Modeling, Growth and Characterization of

III-V and Dilute Nitride Antimonide

Materials and Solar Cells

by

Aymeric Maros

A Dissertation Presented in Partial Fulfillment
of the Requirements for the Degree
Doctor of Philosophy

Approved April 2017 by the
Graduate Supervisory Committee:

Richard King, Chair
Christiana Honsberg
Fernando Ponce
Stephen Goodnick

ARIZONA STATE UNIVERSITY

May 2017

ABSTRACT

III-V multijunction solar cells have demonstrated record efficiencies with the best device currently at 46 % under concentration. Dilute nitride materials such as GaInNAsSb have been identified as a prime choice for the development of high efficiency, monolithic and lattice-matched multijunction solar cells as they can be lattice-matched to both GaAs and Ge substrates. These types of cells have demonstrated efficiencies of 44% for terrestrial concentrators, and with their upright configuration, they are a direct drop-in product for today's space and concentrator solar panels. The work presented in this dissertation has focused on the development of relatively novel dilute nitride antimonide (GaNAsSb) materials and solar cells using plasma-assisted molecular beam epitaxy, along with the modeling and characterization of single- and multijunction solar cells.

Nitrogen-free ternary compounds such as GaInAs and GaAsSb were investigated first in order to understand their structural and optical properties prior to introducing nitrogen. The formation of extended defects and the resulting strain relaxation in these lattice-mismatched materials is investigated through extensive structural characterization. Temperature- and power-dependent photoluminescence revealed an inhomogeneous distribution of Sb in GaAsSb films, leading to carrier localization effects at low temperatures. Tuning of the growth parameters was shown to suppress these Sb-induced localized states.

The introduction of nitrogen was then considered and the growth process was optimized to obtain high quality GaNAsSb films lattice-matched to GaAs. Near 1-eV single-junction GaNAsSb solar cells were produced. The best devices used a p-n heterojunction configuration and demonstrated a current density of 20.8 mA/cm^2, a fill

factor of 64 % and an open-circuit voltage of 0.39 V, corresponding to a bandgap-voltage offset of 0.57 V, comparable with the state-of-the-art for this type of solar cells. Post-growth annealing was found to be essential to improve V_{oc} but was also found to degrade the material quality of the top layers. Alternatives are discussed to improve this process. Unintentional high background doping was identified as the main factor limiting the device performance. The use of Bi-surfactant mediated growth is proposed for the first time for this material system to reduce this background doping and preliminary results are presented.

ACKNOWLEDGMENTS

This section could take up a whole chapter by itself. It is going to be difficult to list every person who helped in any way throughout this adventure as they were so many of you and I apologize in advance if your name was neglected.

That being said, as many others in the III-V community, I've admired the work of my advisor Professor Richard King for years. I was thrilled when he decided to join ASU and was even more thrilled when I was given the opportunity to join his group. His experience and advice have been invaluable and I've appreciated the freedom and trust that he has always given me throughout my PhD. I'm excited to see what will be coming next for his students who are extremely talented and I'm sure they will do great in their research.

Secondly, I don't think there are words that could describe how grateful I am to Professor Christiana Honsberg. Prof. Honsberg was my advisor during the first years of my Ph.D and along with Dr. Chantal Arena, she convinced me to join ASU to start a Ph.D. in collaboration with Soitec. When I see where that has taken me and all the people I got to meet along the way that was probably one of the best decisions I've made. I am extremely thankful for her continuous trust and support. I'm also glad I finally got to see the electric Fiat 500 that she now drives before I finished my program. I also owe a special debt of gratitude to Chantal Arena. I would not be where I am today without her pushing me to join ASU a few years ago. This also extends to the entire team I got the opportunity to work with at Soitec Phoenix Labs, Fred Newman, Ding Ding, Jin Fan, Steven Young, Kapil Vishnubhatla, Frank Reinhardt, Heather Mcfaliven, Ron Bertram, Karen Arters and many others.

I am also very grateful to Professor Nikolai Faleev who taught me everything I know about MBE growth. There is a say in the community that MBE actually stands for Most Broken Equipment. This has proven to be true way too many times. We've spent countless hours trying to fix it, as he would say "this was more or less a typical situation", but I've learned more than I could have expected from that. Thank you for your continuous support.

A special thank you to Professors Stephen Goodnick and Fernando Ponce for serving on my committee. I've really enjoyed the numerous and always rich in information conversations about TEM and other materials and device characterization. Also a special thank you to our lab manager at the Solar Power Laboratory Bill Dauksher for always ensuring that we get to work in the best conditions possible in the lab.

A huge thank you to my MBE-grower colleague and cell processing champion Chaomin Zhang for helping with and teaching me about cell processing. I've also very much appreciated the many useful conversations with my good friend Joshua Williams. I'm always impressed by his level of knowledge on vacuum systems and more generally about MBE growth. I've actually always kept in mind something Josh said to me after Professor Honsberg, something that went along the line of "write your dissertation as you were writing to yourself when you started your Ph.D.". Probably one of the best piece of advice I was ever given and could ever give for any other Ph.D. students.

Thank you to Professor Yong-Hang Zhang for granting me access to his optoelectronics characterization laboratory and thanks to the LeRoy Eyring Center for Solid State Science for supplying and maintaining much of the characterization research equipment used in this thesis. A special thanks to Kenneth Schmieder from the Naval

Research Laboratory for helping with the DLTS analysis. Thank you to the ASU Nanofab and their faculty for their availability and always helpful advice. I would also like to thank the funding agencies that have made this work possible, most especially the joint funding from the National Science Foundation and Department of Energy for the QESST ERC.

From a more personal standpoint, I would like to thank all of my friends for getting me through this journey. I want to give a special big up to the "European gang". The Norwegians, Tine and Jan-Erik and their three kids Audun, Sigurd and Olav. What a family you've got. I'll miss you guys. Pablo the Kansas boy from Spain and Emily, you guys inspire us all. My roommate Simone, who has eaten pasta for lunch every day since I met him. I guess this is not a myth, Italians do like their pasta. Also the Portuguese/Bostonian Dr. Dre, I'm still mad about losing the European cup to you, but we'll get you next time. Finally, the French and Swiss couple Mathieu and Laura. I hope you're leaving the dream back in Switzerland. I also have to give credit to the Bertoni's group in general. You guys have been great, many stories shared during our five dollar burger Tuesday tradition. I also want to remember my soccer team, #Becausefutbol. Not the greatest name I'll give you that but it's been a lot of fun playing with you all every week. It's been a fun ride with you all and I feel very fortunate to count you all as my friends.

Last but not least, my girlfriend Paulina. Thank you for always being by my side, I love you. Finally a huge thank you and much love to my parents, Dominique and Elisabeth, I would not be here without you (literally!), and my brother Amaury. Even when I decided to move to the other side of the world, you have always pushed me to pursue my dreams, thank you so much for always being so supportive.

TABLE OF CONTENTS

Page

CHAPTER Page

LIST OF TABLES

LIST OF FIGURES

Figure Page

Figure Page

Figure Page

Figure Page

Figure Page

CHAPTER 1

MOTIVATION

1.1. The argument for solar energy

Most of our energy consumption today still relies on the burning of fossil fuels (oil, coal and natural gas). Fossil fuel combustion results in greenhouse gas emission, mainly carbon dioxide (CO_2), which absorbs and traps heat causing the Earth's surface temperature to rise. Anthropogenic carbon emission, which is currently increasing at a rate of 1.8% every year [1], has reached unprecedented levels and has caused the average Earth temperature to increase to about 0.8 – 0.9 °C since the beginning of the 20th century [2]. It is predicted that if nothing is changed, temperature will keep rising another 0.5 to 4.5 °C before the end of the 21st century [1]. This rise in temperature, also known as global warming, is one of the consequences of climate change. Other changes in weather, precipitation and wind patterns are expected in the coming years also as a result of climate change [3].

Climate change represents one of the biggest threats to our society and it is crucial to take actions now before it is too late. In 2015, nearly 200 countries signed the Paris climate agreement. This agreement aims to fight climate change by "keeping a global temperature rise this century well below 2 degrees Celsius above pre-industrial levels and to pursue efforts to limit the temperature increase even further to 1.5 degrees Celsius" [4]. Providing clean and sustainable energy is the key to ensure the well-being of our generation but most importantly, the generations who have yet to follow. Renewable energy provides a clean alternative to oil, coal and natural gas. Among renewables, solar is undoubtedly

one of the major candidates to lead us towards a cleaner future. To put it into perspective, the sun provides more energy on earth in an hour and a half than the entire amount that humankind consumes annually [5]. The key for addressing this challenge is to effectively collect this huge amount of energy. Solar cells are photovoltaic (PV) devices that collect sunlight and transform it into electricity, and represent the best option to harvest solar energy. Although only a small percentage of electricity is obtained from PV today (1.2% of the electricity was generated globally from PV in 2015 [6]), this number has seen a remarkably rapid, continuous growth over the last decade. Improving the performance of these solar cells while lowering their cost of production is crucial in order to see an increase in PV deployment in the future. This has been the main motivation behind the work presented in this dissertation.

1.2. Multijunction solar cells

Today's solar market is dominated by flat-plate modules that use crystalline silicon solar cells (> 93% of the market) [7]. Thin-film technologies such as CdTe and CIGS make up most of the remaining market (~ 7%) [7]. Novel technologies such as perovskites have demonstrated very rapid development in the lab, but are still suffering from durability problems which have limited their large-scale production. As of right now, solar cells based on III-V semiconductors have yet to demonstrate lower costs in order to make a significant impact in this market share.

The percentage of incident sunlight transformed into usable electricity in a photovoltaic device is the efficiency of the device. The highest efficiencies demonstrated

for single-junction solar cells based on Si, CdTe, CIGS, perovskites and GaAs are 26.3%[1], 22.1%, 22.6%, 22.1% and 28.8% respectively [8]. The maximum theoretical efficiency for a single-junction solar cell is around 31% at 1.31 eV, as predicted by detailed balance analysis [9]. This indicates that experimentally demonstrated efficiencies are approaching their theoretical limit and that new approaches have to be considered in order to obtain higher efficiencies.

There are two main loss mechanisms limiting solar cell efficiency: the transmission of photons that have an energy lower than the bandgap and the thermalization of photons that have an energy much greater than the bandgap [10]. Multijunction solar cells (MJSC), or tandem solar cells, are designed to reduce these two loss mechanisms, and have been demonstrated to do so. In a MJSC, two or more solar cells, also referred to as junctions, are stacked on top of each other with gradually decreasing bandgap from the top to the bottom of the stack. This allows each junction to absorb a different part of the solar spectrum offering the possibility to better utilize the solar spectrum and hence, reduce efficiency losses due to transmission and thermalization. All the junctions are connected in series which results in an increase of the voltage delivered by the solar cell and an increase in output power. One of the drawbacks of using this configuration is that the overall current in the device is limited by the junction providing the smallest current. The most widely-used MJSC design consists of a GaInP/Ga(In)As/Ge 3-junction (3J) cell design, This type of multijunction cell with monolithic junction growth has demonstrated a record efficiency at 41.6% under 364 suns [11]. The most efficient solar cell to date was demonstrated by

[1] A more recent press release by Kaneka showed an efficiency of 26.6%.

Soitec and the Fraunhofer ISE with an efficiency of 46% under 508 suns and consists of a four-junction (4J), GaInP/GaAs/GaInPAs/GaInAs structure achieved by wafer bonding [12]. However, in spite of their high efficiency, this III-V technology remains too expensive for one-sun solar cells at present, with one major cost driver being the cost of the III-V or Ge substrates [13]. As a result of these high costs, the use of III-V MJSCs have been limited to two specific applications, space and concentrator PV.

III-V solar cells have been used in space to power satellites since the mid-1990s [14]. In addition to their high efficiency they are light in weight, radiation tolerant, and have low temperature coefficients which make them ideal candidates to be used in space. The high costs associated with these MJSCs are acceptable in space since high efficiency allows the use of fewer cells to power the required payloads, reducing spacecraft size, weight, and launch costs.

In order to make this technology suitable for terrestrial applications however, costs unarguably need to be lower. Concentrator photovoltaics (CPV) represents the main terrestrial application for this type of solar cells. In most terrestrial concentrator systems, the high cost of the cells per unit area is offset since only a small area of cells is needed at the focus of the concentration optics (typical CPV cells have an area of about 0.25 cm^2 vs. 32 cm^2 for a standard space cell). Moreover, the Fresnel lenses or reflective optical elements that CPV systems use to focus the sunlight result in light intensities several hundred times that of one-sun on these small area cells, which increases the voltage and current and pushes the efficiency even higher [15], as shown in Figure 1.1. For instance an ideal 4J cell has a maximum efficiency close to 55 % under 1 sun, which goes up to roughly 65 % under 500 suns and closer to 70 % under maximum concentration (~ 46000 suns).

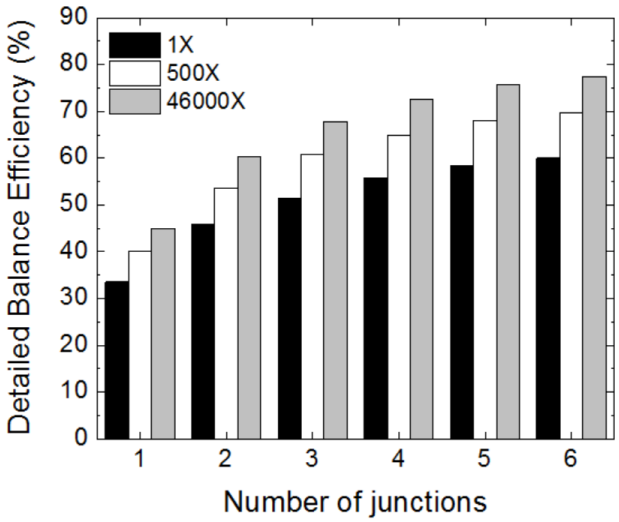

Figure 1.1 Detailed balance efficiency for multijunction solar cells as a function of the number junctions, and under three concentration levels (1-sun, 500-sun and max concentration).

The majority of CPV systems use high concentration ratios (between 300 and 1000 suns). Smaller concentration ratios (below 100 suns) are also used but these are largely designed for Si-based devices [16]. High concentration PV (HCPV) systems are equipped with two-axis tracking systems which allow the module to follow the sun throughout the day. Although this adds significant costs to the system, it greatly increases its energy output. Due to the optics configuration, CPV modules can only make use of the direct sunlight, unlike a conventional flat-plate module that can make use of both the direct and diffuse component. CPV systems are thus of particular interest in sunny regions with high direct normal irradiance (DNI), typically larger than 2000 kWh/m^2 [17]. Figure 1.2 is a world map of the DNI showing that CPV would be an ideal choice for the southwest of the US as well as in parts of South America, Africa and much of Australia. As of 2016, the global cumulative CPV installations was 360 MW at peak power with the largest plants currently being in China (60 and 80 MWp), South Africa (44 MWp) and Colorado, US (30 MWp) [17].

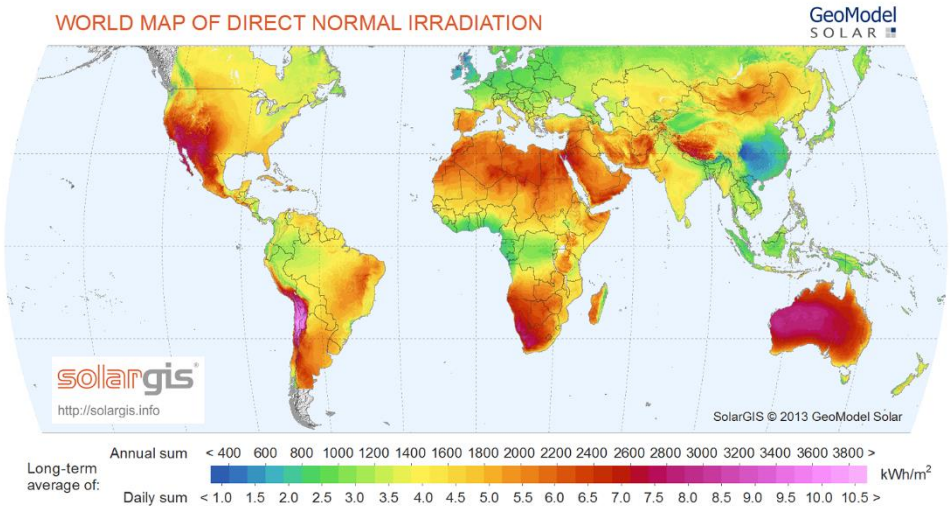

Figure 1.2. World map of DNI showing areas of interest for CPV applications (where DNI > 2000 kWh/m^2) [18].

The most recent CPV report published by the Fraunhofer ISE and the National Renewable Energy Laboratory (NREL) revealed that the current levelized-cost-of-electricity (LCOE) for CPV power plants ranges from $0.11/kWh to $0.16/kWh in locations with a DNI of 2000 kWh/m^2 and from $0.09/kWh to $0.13/kWh in locations with a DNI of 2500 kWh/m^2 (note that the prices were converted from euro to dollar assuming an exchange rate of 0.9) [17]. It is also predicted that CPV has a strong potential for cost reduction and given that CPV installations continue to grow, the LCOE could reach $0.05/kWh to $0.08/kWh by 2030 [17]. Although these predictions are very encouraging, CPV still remains a fairly young technology and its lack of maturity has caused the market to undergo several crises over recent years, with many companies closing or refocusing their core activities [17]. The key to ensure a future for CPV is to work towards costs reduction, both at the cell and the system level. One of the most viable ways of reducing costs is to improve the efficiency. In 2011, the U.S. Department of Energy launched the Sunshot initiative which aims at bringing the cost of solar electricity below $1/W by 2020.

Within this initiative, one of the projects led by NREL is more specifically looking at designing and building multijunction solar cells to exceed 50% efficiency under concentration by 2020. Being able to demonstrate a 50% efficient solar cell has been a long-standing goal but would eventually lead to significant progress for the HCPV market. It should be noted that higher efficiencies would also be beneficial for space PV as it would provide even higher power-to-weight ratio, a factor that is particularly important when considering that the cost of launching a satellite is on the order of $5000/kg – $20000/kg depending on the final orbit.

1.3. The 1-eV magic number

Figure 1.1 showed that increasing the number of junctions provides a clear path towards higher efficiencies. The major challenge in achieving these high efficiencies is to use the appropriate combination of materials. Detailed balance calculations can be used to figure out the optimum bandgap combination that would provide the highest efficiency based on the number of junctions. Figure 1.3 below shows the optimum bandgap combinations for a set of series-connected multijunction designs under 1-sun concentration [18]. Note that these bandgap values are likely to change under concentration.

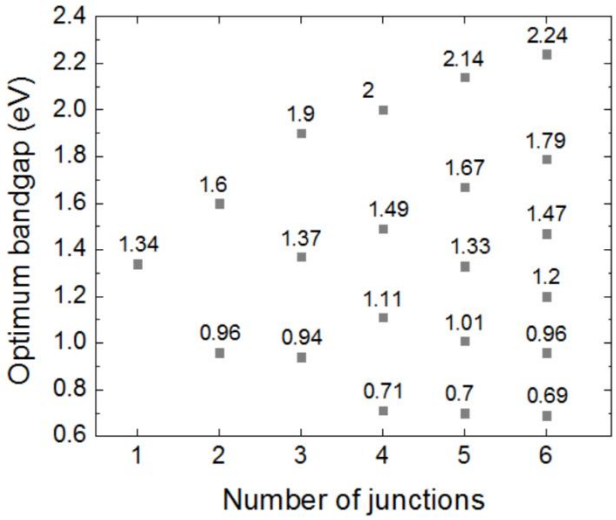

Figure 1.3. Optimum bandgap combinations for detailed balance calculations at 1 sun under the AM1.5G spectrum, for multijunction cells with different numbers of junctions [19].

As stated earlier, the most widely-used MJSC today is a 3J cell based on GaInP/Ga(In)As/Ge (1.85/1.40/0.67 eV) with a record efficiency of 41.6% under 364 suns [11]. However the bandgap combination of this 3J device is not optimum for high efficiency. Due to its low bandgap, the Ge bottom cell produces much more current than the upper two cells, and this excess current is essentially lost. Figure 1.3 shows that an optimum 3J cell should have a bottom cell with a bandgap close to 1 eV. Based on this argument, Solar Junction demonstrated a lattice-matched GaInP/GaAs/GaInNAs(Sb) 3J with a 1-eV dilute nitride bottom cell with an efficiency of 44% under 942 suns [19]. Sharp on the other hand used an inverted metamorphic (IMM) approach to realize a GaInP/GaAs/GaInAs 3J with a 1-eV GaInAs bottom cell with a slightly higher efficiency of 44.4% under 302 suns [20]. Again, higher efficiencies are expected by increasing the number of junctions. In that regard, NREL demonstrated an inverted metamorphic (IMM) 4J structure using GaInP/GaAs/GaInAs/GaInAs (1.85/1.40/1.00/0.74 eV) with an efficiency of 45.7% under 234 suns [21] while Soitec and the Fraunhofer ISE demonstrated

a wafer-bonded 4J cell using GaInP/GaAs//GaInAsP/GaInAs (1.85/1.40/1.12/0.74 eV) with an efficiency of 46% under 508 suns (currently the world record) [12]. Despite the impressive high efficiencies demonstrated by these two structures (IMM and wafer-bonded), both require the use of complex manufacturing processes. In the case of the wafer-bonding example, the top two cells are grown lattice-matched to a GaAs wafer while the two bottom cells are grown lattice-matched to an InP wafer. The cells are then brought together by bonding each wafer to each other and then etching away both wafers. Besides the need for two different expensive substrates, there is an additional cost associated with the bonding process and the epitaxial lift-off or in this case, complete etching of the wafers. This cost could be lowered drastically by reusing the substrates several dozens of times [13, 22], approach that has been used by companies such as Alta Devices and Microlink Devices [23]. However it is not clear how many substrate reusals these companies are able to demonstrate at the moment. Concerning the case of NREL's IMM structure, additional manufacturing costs come as a result of the use of lattice-mismatched materials. Indeed the growth of metamorphic materials implies the need for thick buffer layers to be incorporated in between each lattice-mismatched junctions to relieve the strain induced by the lattice mismatch. This involves longer and more complex growth processes and implies the use of more materials which both adds to the manufacturing costs. Note that epitaxial lift-off of the wafers is also necessary in this approach. Additionally from a space application standpoint, it has been shown that GaInAs demonstrates a lower radiation resistance than GaAs or GaInP [24]. Recent radiation testing of a 4J IMM solar cell revealed that the end-of-life (EOL) performance remained at 82% that of the beginning-of-life (BOL) [25]. Although this has improved over the years, it remains lower than the EOL that can be

achieved by conventional Ge-based lattice-matched 3J solar cells developed by companies such as Spectrolab, SolAero or Azurspace which have demonstrated EOL ranging from 85% to 90%.

Whether the cells are designed to be used in space or in CPV, there is a need for new approaches that combine the improvement of cell efficiency and the reduction of manufacturing costs. In order to reach efficiencies greater than 50%, the use of structures with four junctions and higher is essential. In these 4-, 5- and even 6J designs, most of the challenges lie around the development of junctions with bandgaps close to 1.0 eV and higher than 2.0 eV. With that in mind, we have chosen to work towards advancing the development of the state-of-the-art III-V solar cells by using non-conventional materials. In particular, we focused on the development of dilute nitride materials to realize 1-eV solar cells lattice-matched to GaAs. Lattice-matched growth is preferred since all the cells can be monolithically grown on a single wafer without the need for thick graded buffer layers, simplifying the growth process and opening ways to costs reduction. Moreover, this type of cells have demonstrated efficiencies of 44% for terrestrial concentrators [19], and with their upright configuration they are a direct drop-in product for today's space solar panels, not requiring additional processing beyond conventional three-junction cells.

In this work, we have developed a growth process to realize GaNAsSb solar cells lattice-matched to GaAs using molecular beam epitaxy (MBE). The advantage of this material system is that it can be grown lattice-matched to both GaAs and Ge while its bandgap can be tuned from 0.8 to 1.4 eV, making it an ideal candidate for use in a MJSC. This next section will describe how this thesis is organized and will point out some of the language that will be frequently used throughout this dissertation.

1.4. Dissertation overview

Dilute nitrides, or dilute nitride materials, are GaAs-based materials in which nitrogen has been added in dilute amounts (typically less than 5%). They were first proposed and demonstrated in 1995 [26]. They have more recently gained particular attention as they allowed the demonstration of the first multijunction with an efficiency above 44% [19]. Dilute nitrides include, but are not limited to GaNAs, GaInNAs and GaNAsSb. In some instances, it can also refer to GaP-based materials such as GaNP or GaNPAs. In this work, we will use the term dilute nitride antimonide to refer to the GaNAsSb alloy.

The chemical formula of the materials presented in this work always follow the same nomenclature. That is, III-V materials are presented in order in which they are found in the periodic table. The group-III elements are listed first in order of their atomic weight, followed by the group-V elements, also listed in order of their atomic weight. As an example GaNAsSb is used rather than GaAsSbN. The term multijunction solar cell (MJSC) has been extensively used in the introduction chapter and will also been used throughout the following chapters. We will refer to J1 as the junction that sees the light first, i.e., the top cell. J2 then corresponds the second cell to see the light, then J3, and so forth and so on until the last, i.e., bottom cell. Note that the term "(sub)junction" or "(sub)cell" is used interchangeably as well.

CHAPTER 2 presents some of the background related to semiconductor materials and epitaxial growth, introducing in particular the concept of growth of strained materials and the resulting critical thickness.

CHAPTER 3 covers the experimental details section. It presents a detailed discussion of the technique that has been used to synthesize the materials presented in this work, *i.e.*, molecular beam epitaxy (MBE), as well as all the characterization techniques that have been used to analyze the grown materials and devices.

CHAPTER 4 first introduces some of the fundamental physics behind basic solar cells operation. The optical modeling of multijunction solar cells is then described and the effect of high temperature on the performance of GaAs single-junction solar cells is investigated.

CHAPTER 5 focuses on the structural characterization of nitrogen free materials, namely GaInAs and GaAsSb. The main motivation behind the work presented in this chapter was to understand the formation of defect creation during the growth of lattice-mismatched materials. Most of the work presented in this chapter was published in Ref. [27].

CHAPTER 6 focuses on the optical characterization of nitrogen-free GaAsSb. The goal was to understand the optical properties of these materials prior to the introduction of nitrogen. In particular, it led to a better understanding of the material properties when non-optimum growth conditions were used. Most of the work presented in this chapter was published in Ref. [28].

CHAPTER 7 looks at the development of the dilute nitride antimonide (GaNAsSb) lattice-matched to GaAs. In this chapter, the growth conditions are optimized in order to demonstrate lattice-matched films with the appropriate bandgap close to 1 eV. The optical properties of this material are also investigated and optimization of the thermal annealing conditions is presented. Part of this work was published in Ref [29].

CHAPTER 8 presents the results of 1-eV GaNAsSb single-junction solar cells grown following the growth process developed in the previous chapter. The effect of thermal annealing is discussed. Additionally, standard and novel antireflective coating approaches are investigated. The results presented in this chapter are currently being put together for publication.

CHAPTER 9 is aimed at carefully reviewing the performance of these GaNAsSb solar cells to try to understand where the performance limitations originate from. In particular, the main factors limiting the efficiency of these devices are identified and discussed. The work presented in this chapter is also currently being considered for publication.

Finally CHAPTER 10 presents a conclusion and addresses the future work.

CHAPTER 2

BACKGROUND

2.1. Semiconductor materials

Semiconductor materials relate to a class of materials that have unique electronic and optical properties. These semiconductors can be made of different elements from the periodic table. The most common materials are either from the group-IV, such as silicon or germanium, or can be a mix of group-III and group-V elements such as GaAs or InAs and group-II and group-VI elements such as CdTe or ZnSe. Semiconductor materials are at the heart of solar cell device physics and operation since their properties can be tuned based on which elements are chosen, resulting in different band structures and thus, different electrical and optical properties.

Each material can be identified by its bandgap energy, defined as the minimum energy difference between the conduction band (CB) and the valence band (VB). As shown in Figure 2.1, a material is said to have a direct bandgap if the minimum of the CB and the maximum of the VB occurs at the same crystal momentum. That is the case for most III-V semiconductors such as GaAs or InP for instance. On the other hand, if the minimum of the CB and the maximum of the VB do not coincide, the bandgap is said to be indirect. That is the case of silicon and germanium. Direct bandgap materials are preferred for optoelectronic applications as electrons from the VB can easily be promoted to the CB, given that they are provided with enough energy by the incident photons. The opposite process is also highly probable in which case an electron from the CB can recombine with a hole in the VB, process in which a photon is emitted. On the contrary, in an indirect

material such processes are much less probable as they also require the absorption or emission of a phonon in order to occur.

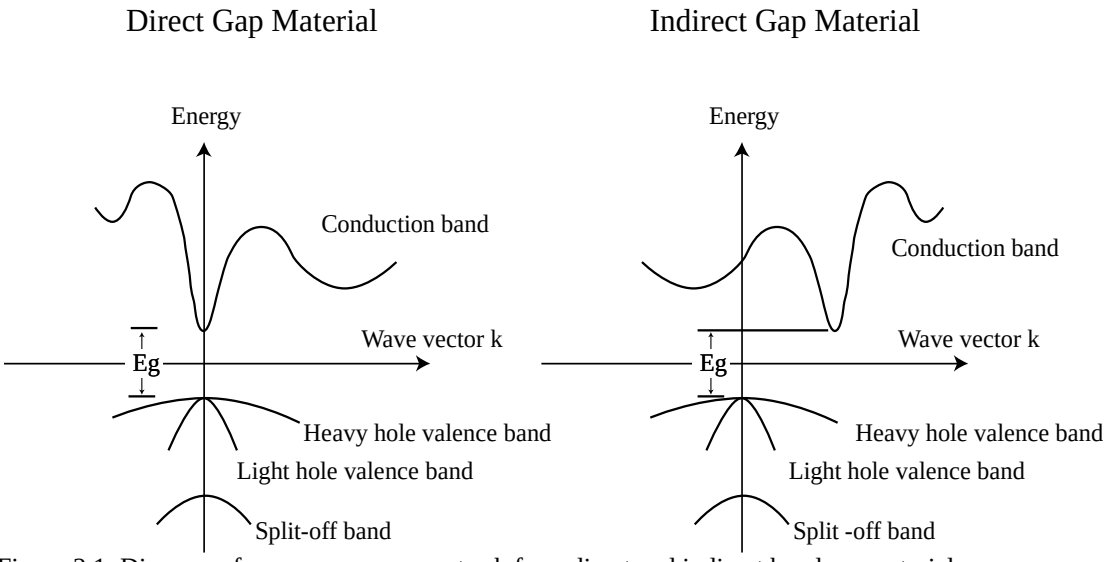

Figure 2.1. Diagram of energy vs. wavevector k for a direct and indirect bandgap material.

Despite its indirect bandgap, silicon has been the predominant material in the electronic industry for decades. Silicon also strongly dominates the solar market with still a 93 % production market share in 2015 [7]. However due to its indirect bandgap, silicon does not absorb light very efficiently. Direct bandgap semiconductors on the contrary have a much higher absorption coefficient, as shown in Figure 2.2 and are usually preferred for optoelectronic applications.

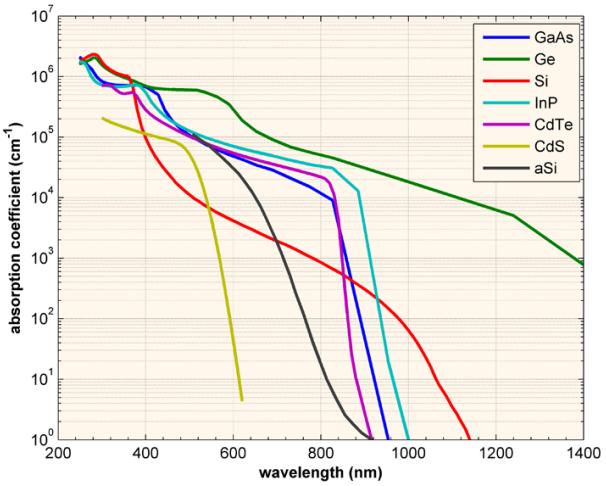

Figure 2.2. Absorption coefficient vs. wavelength for various direct and indirect bandgap materials.

As a material cannot absorb photons that have energies lower than its bandgap, there is a sharp cut-off of the absorption coefficient right at the bandgap of each material. Different materials can be alloyed to tune the bandgap. For instance, alloying GaAs (1.42 eV bandgap) with InAs (0.354 eV bandgap) to form $Ga_{1-x}In_xAs$ results in a bandgap of 1.0 eV for an indium composition x of 30 %. Alloying does, however, change the crystal structure of the material. The crystal structure of a semiconductor material consists of an arrangement of atoms that forms a so-called unit cell. The lattice parameter, or lattice constant, refers to the size of this unit cell. Silicon and germanium have a diamond structure while most III-V materials have a zinc-blende structure. Figure 2.3 presents the bandgap of various semiconductors as a function of their lattice constant.

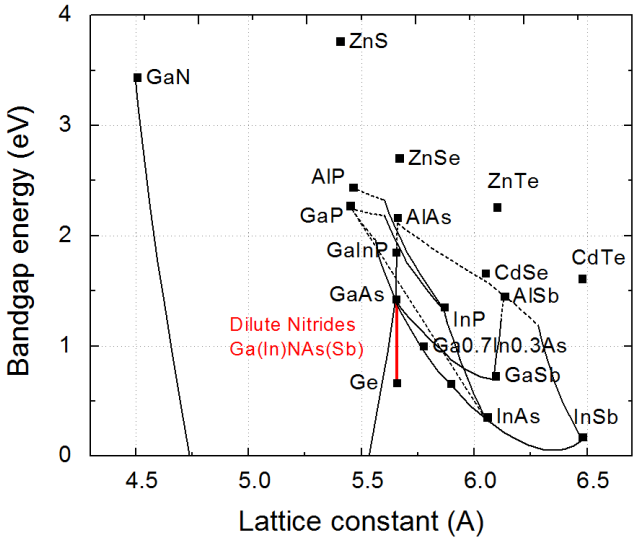

Figure 2.3. Bandgap energy vs. lattice constant for various semiconductor materials.

Most of the work presented in this dissertation has focused on alloying GaAs with InAs or GaSb and GaN to form Ga(In)NAs(Sb). By tuning the composition of each element, the bandgap of this material can be tuned from 0.8 to 1.4 eV while its lattice parameter can be kept the same as that of GaAs or Ge [26], as shown by the red line on Figure 2.3. Because of this unique property, this material system has brought a lot of attention from the solar community. The next section will briefly introduce how these materials are fabricated.

2.2. Epitaxial growth

Semiconductor materials are usually fabricated by depositing thin layers of a material onto the surface of another crystalline material, usually a substrate, so that the deposited film has ideally the same crystal structure as that of the substrate (*i.e.*, same lattice parameter). This process is called epitaxial growth. Several epitaxial growth techniques have been developed over the years. Among them, two are commonly used to grow III-V materials: metal-organic chemical vapor deposition, or metal-organic vapor phase deposition (MOCVD, or MOVPE) and molecular beam epitaxy (MBE). More

recently hydride vapor phase epitaxy (HVPE) has shown growing interest from the III-V community as it offers a very high throughput and potentially lower cost alternative to MOVPE. High quality III-V films have been grown by HVPE at very high growth rates (~ 60 µm/hr) with a very simple process and devices were fabricated demonstrating excellent results and hence great promise for this technique [30]. HVPE still, however, lacks of maturity with regards to MOVPE and also presents limitations when it comes to accurate control of the interface sharpness or doping.

MOVPE has been adopted by most of the III-V concentrator and space cell manufacturers as it provides high quality III-V materials with very good control of the growth parameters and offers a high throughput. However due to the metal-organic precursors used in a MOVPE reactor, a high concentration of hydrogen and carbon is typically present during growth which has been associated with high background doping levels and the formation of defect complexes (such as N-H for instance) in MOVPE-grown dilute nitride materials [29][30]. In particular, it has been shown that the carbon background doping increases with nitrogen content [33]. High background doping is detrimental to dilute nitride solar cells such as GaInNAs and GaNAsSb as it results in short depletion widths which do not allow proper carrier extraction and hence limits the solar cell performance [34]. The use of higher growth temperature and different substrate orientation has been proposed to lower the background doping level in MOVPE-grown materials however the values remain much higher than what can be achieved by MBE [31].

As a result, MBE was proven to be the best suited technique to grow dilute nitride materials. Although providing a much lower throughput than MOVPE, MBE offers an extremely good control of the growth kinetics and is usually preferred for research purposes

as the ultra-high vacuum used during growth forms an extremely clean environment, ideal for the growth of high quality material. The thickness of the grown film can be controlled down to a single atomic layer and through the use of mechanical shutters, abrupt interfaces are easily achievable. Low background doping ($< 10^{15}$ cm^{-3}) have been reported in dilute nitride materials grown by MBE which led to record high current densities [34]. Typical MBE growth temperatures are also much lower than what is used in MOVPE (~ 400 – 600 °C versus ~ 600 – 850 °C respectively) which is again another advantage for the growth of dilute nitrides which are preferably grown on the lower end of that temperature range (~ 420 – 450 °C).

All the dilute nitrides films and solar cells presented in this dissertation were grown by MBE on GaAs (001) wafers. Section 3.1. will provide more information about MBE growth and will describe in details the growth conditions used in this work. The next section will cover some of the basics of epitaxial growth including growing layers under lattice-matched or lattice-mismatched conditions and the effects on the material quality of the resulting films.

2.2.1. Lattice-matched and lattice-mismatched growth

During epitaxial growth, thin layers of a material are deposited onto the surface of another crystalline material (usually a substrate), that imposes its crystallographic ordering to the grown layer. The term homoepitaxy is used when a material is grown on a substrate made of the same material, such as GaAs on GaAs for instance. If the grown material differs from that of the substrate, then the term heteroepitaxy is used. This is the case for GaAsSb or GaInAs grown on GaAs for instance. In the case where the grown film has the same lattice parameter as the substrate underneath, growth happens coherently and the

grown layer keeps the same lattice structure as the substrate. This situation corresponds to a lattice-matched growth. On the contrary, if the lattice parameter of the grown film differs from that of the substrate, the film will be grown under strain. This situation corresponds to a lattice-mismatched growth. The amount of strain in the film depends on the lattice mismat f, *i.e.*, the difference between the lattice parameter of the film and that of the substrate:

$$f = \frac{a_f - a_s}{a_s} \tag{2.1}$$

where a_f and a_s correspond to the lattice constants of the film and of the substrate, respectively.

In the case of a lattice-mismatched growth, the strain will force the grown material to adopt the same crystal structure as the substrate underneath. If the lattice parameter of the film is greater than that of the substrate, the film will be under compressive strain while for the opposite case the film will be subject to tensile strain. The strained layer can be grown coherently up to a specific thickness known as the critical thickness h_c, after which it becomes energetically favorable to relieve this strain through the formation of defects called misfit dislocations [35]. This process of strain relaxation through the formation of misfit dislocation implies that the film regain its own lattice structure. Figure 2.4 summarizes the different growth modes.

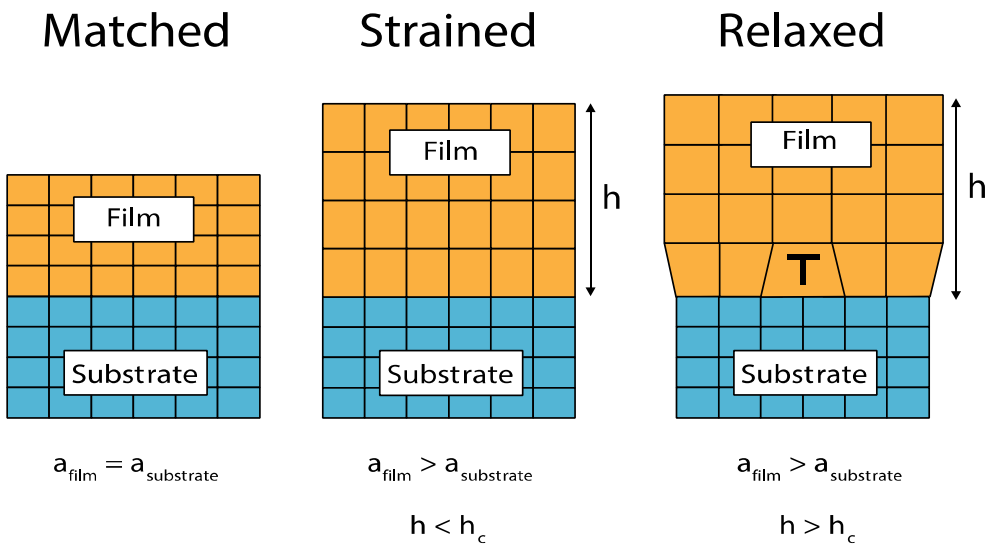

Figure 2.4. Schematic of the different modes of epitaxial growth showing a film grown lattice-matched, a film under strained, and a film that has relaxed. When the film thickness becomes larger than the critical thickness, the film relaxes and forms misfit dislocations.

The growth of lattice-mismatched materials offers a wide range of possibilities as it allows one to tune the optical and physical characteristics of a material based on its applications. In some applications such as long-wavelength detectors and lasers, highly strained quantum wells are preferred while for others such as solar cells, thick lattice-matched layers are preferred. Regardless of the application, structural defects are detrimental to the performance of the final devices and hence their presence must be avoided. It is therefore extremely important to be able to accurately predict this so called "critical thickness" in order to avoid the formation of extended crystalline defects. The next section will introduce the concept and present the theory behind the calculation of the critical thickness.

2.2.2. Critical thickness

Van der Merwe was the first to study in detail this concept of critical layer thickness using thermodynamic equilibrium theory [36]. Later, Matthews and Blakeslee reviewed in depth this concept based on the equilibrium theory in which the misfit strain is

accommodated by the generation of a grid of interfacial misfit dislocations [35]. Although the term critical thickness has been widely used, it should be used with caution as it actually varies based on the growth conditions.

The theory developed by Matthews and Blakeslee (M-B), based on the equilibrium of forces acting on a threading dislocation [35], has unarguably been one of the most used approaches to calculate the critical thickness. However, as noted by Fitzgerald [37], this model was used to calculate the critical thickness of superlattices. Moreover, it was also pointed that M-B assumed isotropic properties for GaAs-based compounds whereas such materials are rather anisotropic. In that sense, Fitzgerald provided a thorough review and comparison of the different critical thickness models developed along with the various parameters used in each of these models [37].

In the equilibrium theory, two forces are considered: the lateral force F_e exerted by the misfit strain on a dislocation and the opposite line-tension force F_l in the dislocation line. Once the two forces balance out, a critical thickness h_c is reached and it becomes energetically favorable to create misfit dislocations to relieve the strain [37]. The lateral force acting on the dislocation line is defined as [37]:

$$F_e = \frac{1}{2} bY\epsilon h \tag{2.2}$$

where b is the Burgers vector, ϵ is the elastic strain, h is the layer thickness and Y is the Young's modulus given by:

$$Y = 2G\frac{(1+\nu)}{(1-\nu)} \quad \text{(isotropic case)} \tag{2.3}$$

$$Y = c_{11}+c_{12}-\frac{c_{12}^2}{c_{11}} \text{ (anisotropic case)} \tag{2.4}$$

here G and ν are the shear modulus and the Poisson ratio, respectively, and c_{ij} are the elastic constant of the layer. The Poisson ratio is defined as $\nu = c_{12}/(c_{11}+c_{12})$. Since the active slip system is <011>{111}, the shear modulus G needs to be calculated using $G = c_{44}-1/3(2c_{44}+c_{12}-c_{11})$ in the anisotropic case [37].

The line-tension force is defined as [37]:

$$F_l=\frac{Db}{2}\left(1-\nu\cos(\alpha)^2\right)\left[\ln\left(\frac{h}{b}\right)+1\right] \tag{2.5}$$

where α is the angle between the dislocation line and the Burgers vector ($\alpha = \pi/3$ in our case) and D is an average shear modulus of the interface given by:

$$D = \frac{G_0 G_S b}{\pi(G_0+G_S)(1-\nu)} \text{ (anisotropic case)} \tag{2.6}$$

$$D = \frac{Gb}{2\pi(1-\nu)} \text{ (isotropic case, } G_0 = G_S) \tag{2.7}$$

where G_o and G_S are the shear moduli of the overlayer and substrate respectively.

The resulting critical layer thickness h_c is obtained by balancing Eq. (2.2) with Eq. (2.5). Considering the anisotropic case, this gives [37]:

$$h_c=\frac{nD}{Y\epsilon}\left(1-\nu\cos(\alpha)^2\right)\left[\ln\left(\frac{h}{b}\right)+1\right] \tag{2.8}$$

Here n corresponds to the number of interface(s) (*i.e.*, 1 for a single bulk overlayer, 2 for a quantum well and 4 for a superlattice) [37]. It is interesting to note that for the isotropic case, assuming $\cos(\lambda) = \frac{1}{2}$ [33, 35], Eq. (2.8) reduces to:

$$h_c = \frac{nb}{8\pi\epsilon\cos(\lambda)}\left(\frac{1-\nu\cos(\alpha)^2}{1+\nu}\right)\left[\ln\left(\frac{h}{b}\right)+1\right] \tag{2.9}$$

which corresponds to the original critical thickness of Matthews and Blakeslee [32].

Table 2.1. List of material parameters used to calculate the critical thickness in this work [38].

Parameter	**GaAs**	**GaSb**	**InAs**	**GaN**
E_g (eV)	1.42	0.726	0.354	3.2
a (Å)	5.6533	6.0959	6.0583	4.508
c_{11} (GPa)	119	88.3	83.4	293
c_{12} (GPa)	53.4	40.2	45.4	159
c_{44} (GPa)	59.6	43.2	39.5	155
G (GPa)	32.8	24.05	19	67
ν	0.312	0.313	0.352	0.352

To realize dilute nitride materials such as GaInNAs and GaNAsSb, small amounts of nitrogen are added to GaInAs or GaAsSb. The addition of In and/or Sb increases the lattice parameter with regards to GaAs while it decreases the bandgap. The addition of nitrogen into GaInAs or GaAsSb decreases the lattice parameter while also decreasing the bandgap. By carefully choosing the In/Sb and N compositions, it is possible to grow thick Ga(In)(N)As(Sb) films lattice-matched to GaAs and Ge, which is desired for the growth of high quality solar cells. This will be reviewed in details in CHAPTER 7.

CHAPTER 3

EXPERIMENTAL DETAILS

3.1. MBE growth

3.1.1. System setup

All the films presented in this work have been grown by solid-source molecular beam epitaxy (MBE), which is an ultra-high vacuum (UHV) technique that allows the growth of semiconductor materials with high crystal quality and with an extremely accurate control of the growth kinetics. Typical UHV conditions are in the order of 10^{-10} Torr to 10^{-11} Torr. The system used to produce all the materials presented in this dissertation was a Veeco Applied Epi Mod Gen III. The UHV in the main chamber is obtained by using a combination of ion pumps and closed-cycle helium cryogenic pumps. From time to time, the cryogenic pumps need to be regenerated due to the saturation of their absorbing materials [39]. In addition, liquid nitrogen (LN_2) is used to fill the cryo shrouds which surround the growth chamber and the effusion cells. Due to its very low boiling temperature (-196 °C), LN_2 acts as an additional impurity trap and increases the pumping of oxygen-containing molecules such as CO, CO_2 and O_2 [40]. In our system, the use of LN_2 in the cryo shrouds reduces the background pressure in the main chamber by at least an order of magnitude. The Gen III system comprises of three other smaller chambers that are used to load/unload the wafers into/from the main chamber as well as pre-heat and degas the wafers prior to epitaxial growth. Figure 3.1 is a schematic of the system used in this work.

During MBE growth, the semiconductor materials are provided in the form of molecular beams which correspond to thermally evaporated elemental sources. Our Gen

III system comprises of twelve source flanges. A total of ten flanges are currently being used for group III (Ga, In, Al) and group V (As, Sb, P and Bi) elements which allows the growth of arsenide-, antimonide- and phosphide-based compounds. Si and Be are used as n-type and p-type doping sources respectively. Additionally, a Veeco UNI-Bulb radio-frequency (RF) nitrogen plasma was installed in order to crack high purity N2 gas and provide reactive nitrogen species for the growth of the dilute nitride materials. The operation procedure for the plasma will be described in a subsection below.

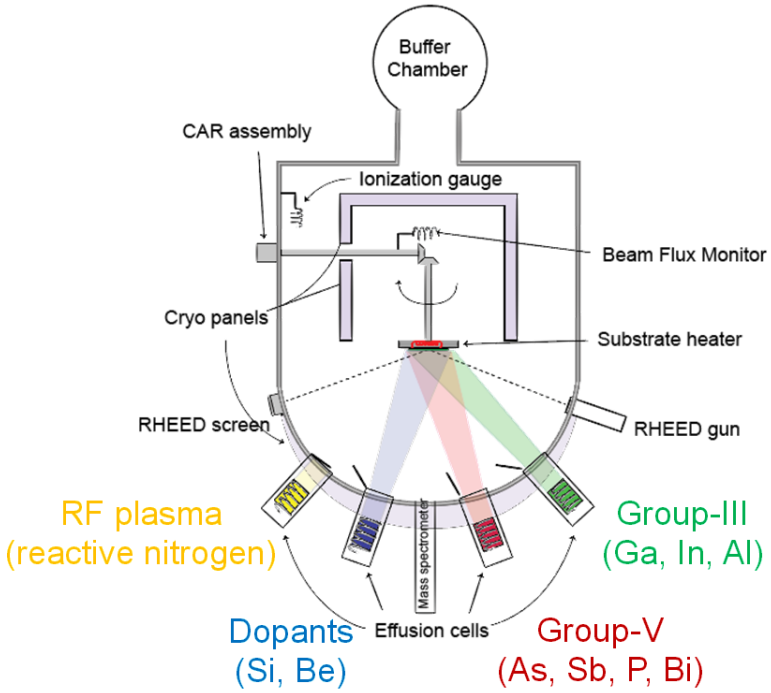

Figure 3.1. Schematic of the MBE system used in this work.

Due to the large amount of materials needed for the As, Sb and P sources, these materials are loaded in cracker valves. During normal operation, the crackers are heated up and the beam flux is controlled by opening of a valve. After passing through the valve, the materials pass through a cracking tube that converts the As_4, Sb_4 and P_4 molecules to As_2, Sb_2 and P_2. This process reduces the consumption of the materials as it is believed that dimmer molecules have a better incorporation and thus less material is required during

growth. Typically the cracker heads were kept at 960°C while the bulk temperature was set to 400, 500 and 280°C for the As, Sb and P cracker cells, respectively. All other materials are loaded in Knudsen effusion cells which are used to evaporate the materials at elevated temperatures. The beam flux is then controlled by changing the temperature of the effusion cell and the opening or closing of a mechanical shutter placed directly in front of the material sources. These molecular beams are directed towards a heated substrate which allows the deposition of high quality epitaxial layers down to a single atomic layer. The substrate is mounted on a continual azimuthal rotation (CAR) unit that allows constant rotation of the substrate during growth to ensure good uniformity across the sample. An ion gauge, hereafter referred to as beam flux monitor (BFM), is mounted on the back of the CAR unit to measure the background pressure in the chamber. The BFM is also used to measure the beam flux, or beam equivalent pressure (BEP) incident on the wafer. In that case, the CAR is rotated 180° so that the BFM directly faces the material sources, as would the substrate during epitaxial growth. The flux of each material is then carefully measured and calibrated prior to each growth process to ensure repeatability over different growth runs.

3.1.2. Operating procedure of the nitrogen plasma source

A great deal of work has been done over the last decade or so on understanding and optimizing plasma conditions to improve the material quality of dilute nitrides. A few references that I have personally found very helpful throughout my work are mainly from Harris's group at Stanford who initiated most of the groundbreaking work that resulted in world record devices [41], [42]. In this section, we will describe the plasma ignition procedure and the limitations that we face due to the current setup of our machine.

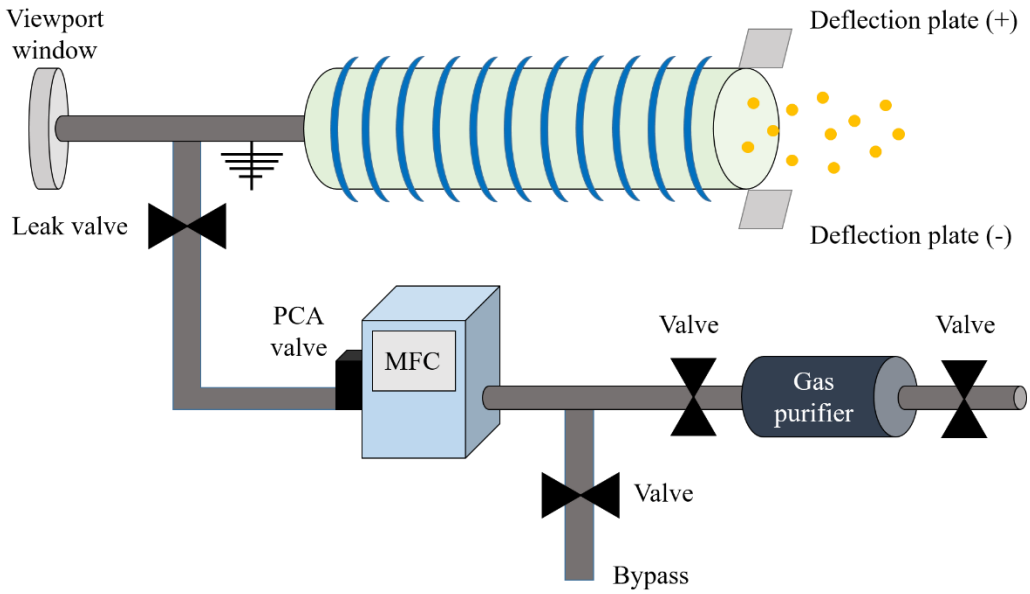

Figure 3.2. Schematic of the nitrogen plasma cell used in this work. Not shown is the RF power unit.

A schematic of our plasma cell is shown in Figure 3.2. A UNI-Bulb radio-frequency (RF) nitrogen plasma was used in this work. The RF power was supplied by an Advanced Energy Industries RFX 600 RF generator operating at 13.56 MHz. High purity nitrogen was supplied through stainless steel tubes from a tank located outside of the building. A gas purifier was installed to reduce contamination of the nitrogen. Isolation valves were also installed before and after the filter to avoid contamination of the filter during purging. A 5 sccm mass flow controller (MFC) from Alicat Scientific Inc. was installed. This MFC allows to control the nitrogen flow down to 0.025 sccm and is equipped with a PCA control valve mounted downstream which operates particularly well in the leak-tight aspect. A gas bypass was installed before the MFC in order to purge the line when needed. In addition to the PCA valve installed on the MFC, another leak valve was installed in between the MFC and the plasma cell in order to ensure that no nitrogen leaks into the chamber.

The typical ignition procedure goes as follows. First, the nitrogen supply line is open through the opening of a manifold (~ 10 – 15 psi input). The nitrogen flow is set to 4

sccm on the MFC. Following this step, the leak valve is open to its full range. At this point, although the nitrogen shutter is closed the background pressure in the chamber rapidly increases up to $4 – 5 \times 10^{-5}$ Torr as nitrogen penetrates in the chamber around the shutter. As the background pressure increases, the RF power unit is turned on and the forward power P_F is rapidly increased to 300 W (the plasma usually ignites when $P_F > 200$ W). If the plasma does not ignite, the RF power can be increased up to 500 W however it should not be kept at these high powers for extended period of times. Upon ignition, the plasma is in "low intensity mode" (it has a pale orange color) and the reflected power P_R increases rapidly (to about 20 – 30 W). At this point the matching knob needs to be tuned to minimize the P_R. From our experience, under normal circumstances, P_R should easily reach down to about 2 – 3 W. The next step consists in lowering the nitrogen flow to the desired value. This is realized step by step in order to avoid extinguishing the plasma. First, the flow is reduced from 4 to 1 sccm. After just a few seconds the plasma switches from a dim to a bright ("high intensity") mode which is clearly visible through the plasma viewport (the plasma should now have a very bright orange/yellowish color). This change in plasma conditions creates a large increase in the reflected power and hence the matching unit should be tuned to reduce P_R as much as possible (by rotating the two knobs A and B). Following this step, the nitrogen flow is then reduced further to the desired target flow (generally 0.2 sccm in most of this work) and is left as is until the pressure in the chamber stabilizes (usually 10 to 15 min). As the background pressure decreases to reach stabilized conditions, the matching unit needs to be constantly tuned to reduce P_R as we found that the reflected power goes up as the pressure in the chamber goes down. With our current setup, with a nitrogen flow of 0.2 sccm and a RF power of 300 W, the typical pressure

during the growth of GaNAsSb is in the range $2 – 3 \times 10^{-6}$ Torr. After growth is completed, the plasma is shut down by setting the MFC to 0 sccm. After the plasma extinguishes, the RF power is rapidly brought to 0 W and finally the leak valve as well as the nitrogen supply are closed.

The large increase in background pressure as a result of the plasma ignition is not desirable as it is associated with plasma. One solution to avoid this would be to install a differentially pumped gate valve which would allow us to ignite the plasma and let it stabilize without introducing "parasitic" nitrogen in the growth chamber. In particular, Freundlich *et al.* showed large improvement in their dilute nitrides material quality through the use of a gate valve [43]. Although such option would most probably improve our material quality as well it requires serious remodeling of our current system and was not achievable within the timeframe of this work. It should be also noted that installing a gate valve would also avoid undesirable nitrogen incorporation in our material. Although the nitrogen shutter is kept closed during plasma ignition and stabilization, SIMS analysis revealed that up to 0.1 % of nitrogen was incorporating in GaAs.

As shown in Figure 3.2, the cell aperture at this end of the plasma source is made of several holes of a specific diameter. Depending on the number of holes and/or their diameter, the plasma can be operated at different flow rates [42]. This aperture can only be changed by opening the MBE chamber. As a result the cell aperture was unknown during the majority of this work. After a recent opening of the chamber, we found that the aperture of our cell contains 499 jets of diameter 0.008" (0.2 mm). All of the work presented in this dissertation was based on this cell aperture however we recently replaced this aperture by a nozzle that has 42 jets of diameter 0.008" (0.2 mm). This will imply a complete

recalibration of the growth parameters in the future in order to characterize the resulting plasma conditions and nitrogen incorporation.

Furthermore, Wistey *et al.* showed that the use of deflection plates biased with moderate voltages led to the removal of the ions from the plasma beam which led to a further improvement of the PL intensity of the GaInNAs(Sb) materials [44]. In our case, the use of deflection plates even at moderate voltages (+/- 40 V) did not lead to any improvement in the PL intensity. Higher voltages were not investigated in this work but could maybe lead to some improvement.

3.1.3. In-situ monitoring

Most MBE systems are also equipped with in-situ monitoring tools. In our case a residual gas analyzer (RGA) is used to monitor the residual species (impurities) present in the growth chamber. The dominant species in the chamber (even after bake-out) is hydrogen (H_2) which originates from cracking of H_2O molecules, and potentially penetrates through the stainless steel walls of the chamber. As it turns out, H is very hard to pump out. The ion pump is especially inefficient at pumping hydrogen (and also phosphorus). All other species have a much lower partial pressure and for the most case, are below the detection limit of the RGA ($< 10^{-13}$ Torr).

Our Gen III system was also equipped with reflection high energy electron diffraction (RHEED) to monitor the oxide removal from the wafers, the surface reconstruction and calibrate growth rates. Typical growth rates for MBE growth are low compared to other vapor phase epitaxy techniques, in the order of 1 Å/sec (0.36 μm/hr) to 3 Å/sec (1.08 μm/hr). The growth rate is typically controlled by the group-III fluxes. It should also be noted that it is important to always maintain an overpressure of the group-

V elements during growth which avoids the grown film to desorb. For instance an As overpressure close to 20 is maintained during the growth of GaAs at high temperature. It was typically lowered to 10 when GaAs was grown at lower temperatures. The As/Ga BEP ratio was also maintained close to 10 – 11 during the growth of our GaNAs(Sb) layers. Similarly, an overpressure of P is needed during the growth of GaInP. We typically used an overpressure close to 20 during the growth of our GaInP materials, however this ratio has not been optimized.

In addition, infrared pyrometry is used to monitor the temperature of the substrate. The deoxidation temperature was used to calibrate our growth temperature. Deoxidation of GaAs wafers typically occurred at 580°C (as per pyrometer temperature). The growth temperature is chosen based on the material that is being grown. Table 3.1 below summarizes typical MBE growth temperatures (substrate temperature) for some of the materials that have been grown in this work.

Table 3.1. Typical MBE growth temperature and V/III BEP ratios used for the various III-V and III-V-N materials grown in this work

	(Al)GaAs	GaInAs	GaAsSb	GaAsP	GaInP	GaNAsSb
$T_{substrate}$ (°C)	580-600	450-500	470-500	500	500	440-460
V/III ratio	20	15	15	20	20	10-11

3.2. Solar cell fabrication

Following the MBE growth, solar cells were fabricated using a standard photolithography process. We will describe here the typical process flow used to fabricate n-on-p (or n-i-p) solar cells. The solar cells were fabricated in the ASU NanoFab facility.

The first step consists in depositing the back metal contact. The front surface of the sample is first coated with photoresist. Electron beam (E-beam) evaporation is then used to deposit Ti/Pt/Au (400/100/2000 Å) on the back side of p-type wafers. The photoresist is

then removed from the front surface and the mesa is created by etching through the p-n junction during the second step. This step ultimately isolates each device from each other. Step three consists in depositing the front contacts. E-beam is used again to deposit n-type contacts Pd/Ge/Pd/Au (500/800/1500/500 Å). In step four the contacts are annealed in a rapid thermal annealing (RTA) furnace in order to form ohmic contacts. Typical RTA conditions were 380 – 420 °C for 20 sec under N_2 ambient. The final step consists in etching the top GaAs cap layer in a mixture of NH4OH:H2O2:H2O (1:1:8) for 30 sec. Standard solar cells were processed into 0.25 cm^2 devices with a grid metal coverage ranging from 10 – 14 %, or 1 cm^2 with a grid metal coverage ranging from 7 – 9 %. The GaAs and GaNAsSb solar cells presented in this work were fabricated following the same process with the exception that the GaNAsSb cells were first annealed right after epitaxial growth in order to improve the material quality. Annealing was usually performed in a RTA furnace at temperature between 750 – 800 °C for 5 – 10 min under nitrogen ambient. Optimization of the RTA conditions for GaNAsSb will be further discussed in CHAPTER 7.

3.3. Characterization techniques

3.3.1. Structural characterization

3.3.1.1. High-resolution X-ray diffraction (HRXRD)

High-resolution X-ray diffraction (HRXRD) is a powerful, fast and non-destructive technique used to characterize the crystal properties of thin epitaxial structures. HRXRD was measured at ASU LeRoy Eyring Center for Solid State Science (LE-CSSS) with a X'Pert MRD (PANalytical) diffractometer. This diffractometer uses a copper anode X-ray tube combined with a multilayer focusing mirror and a 4-bounce Ge (022) assymetric

hybrid monochromator to separate a $CuK_{\alpha 1}$ radiation (λ = 1.54056 Å) with a beam divergence of 0.005° (~18 arcsec). The beam is directed towards the sample that is mounted on a six-axis goniometer designed such that the sample can be moved with angles χ, φ and ω, and along the x-, y- and z-axis, as shown in Figure 3.3. The diffracted beam can be collected either in double-crystal or triple-crystal mode with a special 3-bounce Ge(022) symmetric analyzer crystal. The beam divergence in double-crystal mode can be adjusted by the use of variable slits while the Ge (011) triple-crystal analyzer presents a beam divergence of 0.0033° (~ 12 arcsec).

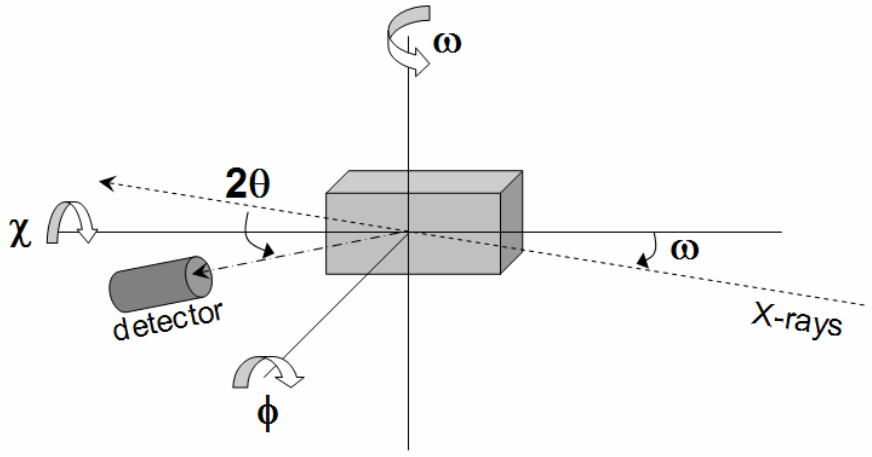

Figure 3.3. Schematic of the HRXRD PANalytical diffractometer used in this work (after [45]).

For almost every sample investigated in this work, XRD was used to measure ω-2θ scans and ω rocking curves. In an ω-2θ scan, the sample rotates around ω while the detector rotates around 2θ. This type of scan is used to measure the lattice spacing. The composition is then calculated based on the diffraction angle of the film according to Bragg's law:

$$\lambda = 2d \sin(\theta) \tag{3.1}$$

where λ is the wavelength of the incident X-rays, d is the lattice spacing and θ is the diffracting angle. In (001) oriented crystals, the (004) Bragg reflection has the highest

intensity therefore ω-2θ scans were collected in the vicinity of the GaAs (004) reflection. Once the lattice spacing is known, the lattice parameter can be obtained from:

$$d = \frac{a}{\sqrt{h^2+k^2+l^2}} \tag{3.2}$$

Where h, k and l are the Miller indices. From there, Vegard's law is used to obtain the alloy composition. Note that this is valid for a ternary alloy such as GaN_xAs_{1-x}, where there is only one variable. For a quaternary material such as $GaN_xAs_{1-x-y}Sb_y$, an additional characterization technique is necessary in order to accurately obtain the composition (we generally used secondary ion mass spectrometry). In the case where the film has a strong vertical coherence, well defined interference fringes (Pendellösung fringes) are also observed and can be used to calculate the thickness of the film.

During an ω rocking curve scan, the position of the sample and detector is chosen to maximize the diffraction peak intensity. The detector is then fixed and the sample is rocked around the maximum of the diffraction peak in the ω direction. The resulting shape and full-width-at-half-maximum (FWHM) can be used to identify the presence of defects as well as their type and density [46].

When a greater sample analysis was required, reciprocal space mapping (RSM) was performed using the triple-axis monochromator. During a RSM measurement, a series of ω-2θ coupled scans are collected at different ω angles. RSM is the most involved of all XRD measurements but provides a complete set of information (composition, thickness, tilt, defects, strain relaxation). Both symmetrical around (004) and asymmetrical around (224) RSM can be collected.

3.3.1.2. X-ray topography (XRT)

X-ray topography is a non-destructive imaging technique that also relies on Bragg diffraction. XRT was used to visualize extended defects such as dislocations in a crystal. XRT can be performed either in reflection (Bragg mode) or transmission (Laue) mode. The reflection mode provides information on the crystal quality near the surface (1 – 10 μm) while the transmission mode provides information about the bulk crystal structure [47]. X-ray topographs were collected at ASU LE-CSSS using a Rigaku XRT-100 system used in reflection mode in order to visually observe misfit dislocations. This system also uses a copper anode X-ray tube to use a $CuK_{\alpha 1}$ radiation ($\lambda = 1.54056$ Å). The power chosen for these analyses was 1.5 kW and the scan speed was set to 2 mm/sec. The diffracted signals were recorded by a live X-ray camera placed 65 mm away from the sample. Images were collected on 50 μm thick emulsion plates with a resolution of 1 μm.

3.3.1.3. Transmission electron microscopy (TEM)

Transmission electron microscopy (TEM) is an extremely powerful technique that can be used to study the structural characteristics of epitaxially grown semiconductors. For TEM investigation presented in this work, wedge cross-section samples were mechanically polished and further thinned by ion milling. The samples were studied in a Philips CM200-FEG TEM with a 200 keV electron beam. Two-beam diffraction contrast images were recorded with a diffracted beam g = 220. In order to visualize crystalline defects on the interface the samples were tilted around the diffraction vector during measurement.

3.3.2. Optical characterization

3.3.2.1. Photoluminescence (PL)

Photoluminescence (PL) measurements were used to probe the optical characteristics of the epitaxial layers. Room-temperature PL was used to obtain information about bandgap and material quality. PL has been particularly useful for optimizing the annealing conditions of the dilute nitride films. Power- and temperature-dependent measurements were used to investigate the presence of localized states within the bandgap of the materials which originated from compositional inhomogeneity. Unless otherwise stated, PL measurements were performed using a 405 nm laser diode with a power ranging from 1 to 120 mW. The laser beam was focused on the samples with a 260 μm spot diameter and chopped for lock-in amplifier purposes. The signal was detected using a spectrometer equipped with a liquid nitrogen-cooled Ge detector. For the temperature-dependent measurements the samples were mounted on the cold finger of a closed-cycle helium cryostat.

3.3.2.2. Photoreflectance (PR)

In some instances, the crystal quality of as-grown material was very poor and as a result the films did not emit any PL at room temperature. In this case, photoreflectance (PR) spectroscopy was performed instead. PR is a non-destructive method used to investigate the band structure, alloy composition and doping concentration of semiconductor materials. It is a very sensitive technique in which the sample is being modulated by a chopped laser beam while the change in reflectance is measured as function of wavelength.

3.3.1. Electrical characterization

3.3.1.1. Capacitance-voltage (C-V)

Capacitance-voltage (C-V) measurements were used to measure the background doping concentration of the grown dilute nitrides films and to estimate the extent of the depletion width. The capacitance C_j of a p-n junction under reverse bias is described by [48]:

$$C_j = \frac{\epsilon_S A}{W_d} \tag{3.3}$$

where ϵ_S is the permittivity of the material (we assumed $\epsilon_S = 12$ for GaNAsSb in this work [49]), A is the sample area and W_d is the depletion width.

The background doping concentration N_B can be estimated by taking the slope $d\left(1/C_j^2\right)/dV$ as shown by Eq. (3.4) below [48]:

$$N_B = \frac{2}{q\epsilon_S A^2 d\left(1/C_j^2\right)/dV} \tag{3.4}$$

3.3.1.2. Deep-level transient spectroscopy (DLTS)

Deep-level transient spectroscopy (DLTS) is yet another powerful tool that allows one to study the electrically active traps (defects) present within the depletion region of a p-n junction. During a DLTS measurement, the diode is kept under reverse bias. A voltage pulse is then applied to fill the traps and the capacitance transient is recorded. Majority traps are observed by applying a reverse bias pulse while minority traps are observed by applying a positive bias pulse. The temperature is then changed and another transient is measured. The system used in this work uses Fourier analysis on the capacitance transients to generate several DLTS spectra for each temperature scan [50]. The corresponding

Fourier coefficients can then be used to extract information such as the activation energy E_A of the trap, the trap density N_T and the capture cross section σ.

Both C-V and DLTS measurements were performed at the U.S. Naval Research Laboratory (NRL) with a Biorad DL 8000 DLTS system. The samples were processed into circular diodes with full metal coverage with varying areas (200 – 1000 μm). Unless otherwise stated, all the DLTS measurements were performed with a reverse bias (UR) of – 2V, a pulse bias (UP) of 0 V, a period width (Tw) of 204.8 ms and a pulsewidth (tp) of 100 μs, 10 ms and 1 s.

CHAPTER 4

MODELING AND CHARACTERIZATION OF III-V SOLAR CELLS

4.1. Solar cell fundamentals

A solar cell is a photovoltaic (PV) device that uses semiconductor materials to convert photons (light), into charge carriers (electricity). The basic operating principle of a solar cell relies on the formation of a junction between two semiconductors of opposite doping, commonly known as a p-n junction. When light is shined onto the solar cell, photons are absorbed and electron-hole (e-h) pairs are generated. These e-h pairs will then be separated by the electric field that built up in the space charge region of the p-n junction. After being separated, the electrons and holes can either be collected at the contacts of the solar cell which results in a photogenerated current, or the electrons/holes can diffuse to the p-side/n-side of the junction where they can move freely until they recombine with one another. Recombination usually happens if a carrier travels a distance greater than its diffusion length L, which depends on the minority carrier lifetime τ and the mobility μ ($L_{n,p}=\sqrt{\tau_{n,p}D_{n,p}}$ where $D_{n,p}=(\frac{kT}{q})\mu_{n,p}$). Every photogenerated carrier that recombines is essentially lost and does not contribute to the current, therefore the longer the diffusion length (and hence the minority carrier lifetime), the better.

There are three main recombination mechanisms that can occur: radiative, Shockley-Read-Hall (SRH) or Auger. Radiative recombination is the dominant mechanism in direct bandgap materials. SRH recombination is a non-radiative process and is associated with the presence of defect states within the bandgap of the material. Auger recombination

is predominant in silicon solar cells however it can also impact the performance of III-V solar cells if these are heavily doped or measured under high level injection.

Recent efforts in the optimization of the material quality and design structure resulted in III-V solar cells that have demonstrated very high quality materials and devices approaching the radiative limit [51]–[53]. Dilute nitride materials however are known for having a low minority carrier diffusion length compared to GaAs [54], [55]. Nevertheless, even with short diffusion lengths good current collection can be achieved with wide depletion widths, for which low background doping is key [56]. This will be discussed in further details in CHAPTER 8 and CHAPTER 9.

4.1.1. I-V characteristics

The performance of a solar cell is measured by its current-voltage (I-V) characteristic. The I-V curve of an ideal solar cell is usually modeled using a one-diode equation model [57]:

$$J(V) = J_L - J_0 \left(\exp\left[\frac{qV}{nkT}\right] - 1 \right) \tag{4.1}$$

where J is the current density through the device (in A/cm^2) as a function of the applied voltage V (in V), J_L is the light or photogenerated current density (in A/cm^2), J_0 is the dark or reverse saturation current (in A/cm^2), q is the electron charge (in C), n is the diode ideality factor, k is the Boltzmann's constant (in J/K) and T is the temperature of the cell (in K).

The ideality factor value is usually between $1 < n < 2$, $n = 1$ being for an ideal solar cell while $n = 2$ being a solar cell dominated by SRH recombination. It is not unusual to find $n > 2$, its origin is still subject to discussion but it is often attributed to high-injection

current or trap-assisted tunneling. A single-diode model is however not always sufficient to model the performance of solar cells in which it is necessary to consider a modified two-diode equation model that takes into consideration parasitic elements such as recombination mechanisms as well as series and shunt resistance:

$$J(V) = J_L - J_{01}\left(\exp\left[\frac{q(V+JR_s)}{n_1 kT}\right]-1\right) - J_{02}\left(\exp\left[\frac{q(V+JR_s)}{n_2 kT}\right]-1\right) - \frac{V+JR_s}{R_{sh}} \qquad (4.2)$$

where R_s and R_{sh} are the series and shunt resistances respectively (in ohm.cm^2). The subscripts 1 and 2 corresponds to the parameters of the first and second diodes respectively, n_1 is typically set to 1 while is n_2 set to 2.

The I-V curve of a solar cell allows for the extraction of several important parameters that define the performance of the device. Figure 4.1 is an example of the characteristics of a GaAs solar cell measured under dark (DIV) and under 1-sun illumination (LIV). Measuring the cell in the dark is useful in order to extract the dark saturation current and the diode ideality factor as well as the series and shunt resistance. The LIV curve allows the extraction of four essential solar cell parameters, the short-circuit current density J_{sc}, the open-circuit voltage V_{oc}, the fill factor FF and the efficiency η. The short-circuit current density J_{sc} corresponds to the photocurrent density J_L at short circuit conditions (when $V = 0$) and is the maximum current that can be driven through the device. There is a situation where the dark current and the photocurrent cancel out and the corresponding applied bias is the open-circuit voltage V_{oc}. At V_{oc}, the device returns to a quasi-equilibrium state and the current no longer flows even under illumination. The open-circuit voltage is a good indicator of the cell quality as it is directly related to the recombination mechanisms. However the V_{oc} is bandgap-dependent therefore in order to

investigate the cell quality it can be quite useful to consider instead the bandgap-voltage offset $W_{oc,}$ defined under open-circuit conditions as [58]:

$$W_{oc} = \frac{E_g}{q} - V_{oc} \tag{4.3}$$

For a good solar cell, it has been shown that a bandgap-voltage offset W_{oc} of 0.4 V or lower is expected (the lower W_{oc} the better) [58]. Dilute nitride materials usually demonstrate W_{oc} higher than 0.5 V due to the presence of N-related defects and other point defects [59].

The efficiency of a solar cell is obtained when the cell outputs its maximum power. The corresponding maximum power point (MPP) happens at a voltage V_m and a current I_m, which are used to calculate the fill factor [57]:

$$FF = \frac{I_m V_m}{I_{sc} V_{oc}} \tag{4.4}$$

The solar cell efficiency is then simply calculated by doing the ratio of the maximum power output by the cell to the incident power:

$$\eta = \frac{P_m}{P_{in}} = \frac{FF\ J_{sc}\ V_{oc}}{P_{in}} \tag{4.5}$$

Figure 4.1b shows how these different parameters are obtained from a typical LIV curve for a GaAs cell.

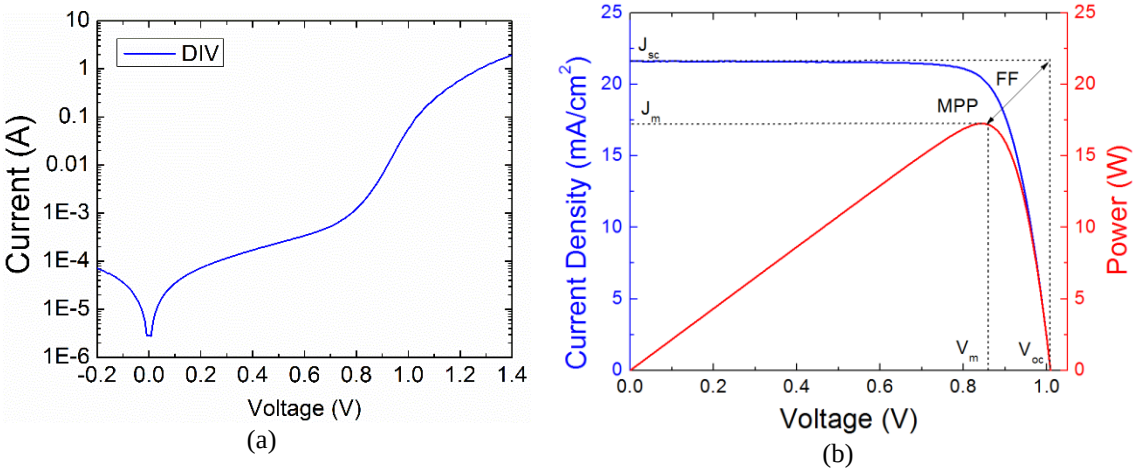

Figure 4.1.a) Dark I-V characteristic of a GaAs solar cell, b) One-sun light I-V characteristics. The corresponding power and the extracted solar cell parameters are shown for reference.

4.1.2. Spectral response

The spectral response is, by definition, the ratio of the current generated by the cell to the power incident on the device at each wavelength (expressed in A/W). However, the term external quantum efficiency (EQE) is often used instead. The EQE is the ratio of the number of photogenerated carriers output by the cell over the number of photons incident on the cell. It is sometimes useful to look at the internal quantum efficiency (IQE), which is the ratio of the number of photogenerated carriers output by the cell over the number of photons absorbed by the cell. The IQE basically takes into consideration the losses associated with the photons reflected back from the surface of the cell. For an ideal solar cell, the EQE (IQE) would be one. The J_{sc} of a solar cell can be obtained by integrating the product of the quantum efficiency with the incident solar spectrum [57]:

$$J_{sc} = q \int EQE(\lambda)\phi_{inc}(\lambda)d\lambda \qquad (4.6)$$

where $\phi_{inc}(\lambda)$ corresponds to the incident solar spectrum. Three solar spectrum standards have been adopted, namely the AM0, AM1.5G and AM1.5D [60]. The AM0 spectrum

corresponds to the solar radiation outside of the terrestrial atmosphere and is therefore used as reference for space applications; it has an integrated spectral irradiance of 1366 W/m². The AM1.5G spectrum takes into consideration atmospheric effects such as absorption and scattering as the light goes through the atmosphere. It has an integrated spectral irradiance of 1000 W/m² and is used as reference for flat-plate terrestrial applications. Finally the AM1.5D is used as reference for terrestrial concentrators as it considers the direct beam from the sun plus the circumsolar component in a disk 2.5 degree around the sun. It has an integrated spectral irradiance of 900 W/m².

An antireflective coating (ARC) layer is usually deposited on the front surface of a solar cell to reduce the front surface reflection. Figure 4.2 shows the improvement of the EQE after depositing a dual ARC layer of SiO_2/SiN onto a GaAs single-junction solar cell.

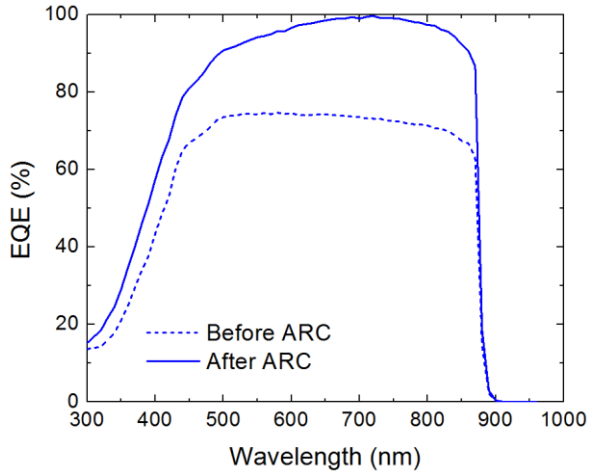

Figure 4.2. External quantum efficiency (EQE) of a GaAs solar cell before and after ARC deposition. The large improvement in EQE results mainly from a reduction in the front surface reflection (note however the rather poor blue response in this device even after ARC deposition).

4.2. Optical modeling of multijunction solar cells

A large portion of this dissertation has focused on modeling the optical properties of multijunction solar cells, in particular modeling of the quantum efficiency in order to optimize the device structure and improve current matching. This work was done in collaboration with Soitec Phoenix Lab in order to improve the structure of their 4J wafer-bonded solar cell.

The current output by a series-connected multijunction solar cells will be limited by the subcell that produces the smallest current. It is therefore extremely important to being able to accurately predict the current generated by each junction in a tandem cell. In this thesis, a transfer-matrix method (TMM) was used to predict the external quantum efficiency of each subcell in a multijunction stack. From there the current generated by each subcell was calculated and the structure was optimized accordingly.

4.2.1. Transfer matrix method (TMM)

The transfer matrix method (TMM) is used to calculate the transmittance, reflectance and internal light absorption in mixed coherent-incoherent multilayer systems. A layer is generally treated as coherent when its thickness is comparable or smaller to the light wavelength and is generally treated as incoherent when its thickness is much larger than the light wavelength. In most cases, solar cells are made of a stack of several layers which each have different optical properties. Because the thickness of these layers are usually in the same order of magnitude than the wavelength of the incident light, the light distribution in the stack needs to be calculated using a TMM. The theory behind the TMM has been described in great details in the literature and therefore, this will not be repeated

here. However, a brief introduction to this approach will be presented. For more information please refer to Refs. [61]–[63].

Because each layer in a solar cell usually has different optical properties (refractive index, n and extinction coefficient, k), when light propagates through the different layers it will be subject to optical interferences as it passes through each interface. These optical interferences will also be affected by the thickness of each layer. If the optical constant and the thickness of the materials are precisely known, one can use the transfer matrix approach to calculate these optical interferences and the light absorption as light penetrates through each layer of the solar cell.

A transfer matrix code was developed in Matlab following the initial work done by Burkard *et al.* from McGeehee's group at Stanford [64].The inputs parameters of the code are the thickness of each layer and their optical constant (n and k). Precise knowledge of these optical constant is crucial in order to obtain accurate modeling results.

4.2.2. Validity of the model

In order to prove the validity of the model, the GaInP/GaAs/GaInPAs/GaInAs 4J cell developed by Soitec, the CEA-Leti and the Fraunhofer ISE was modeled and the corresponding EQE was compared to the measured data. As shown in Figure 4.3a, the model provides a very good representation of the experimental data. Similarly, Figure 4.3b presents the corresponding responsivity obtained from the EQE of the modeled and measured EQE.

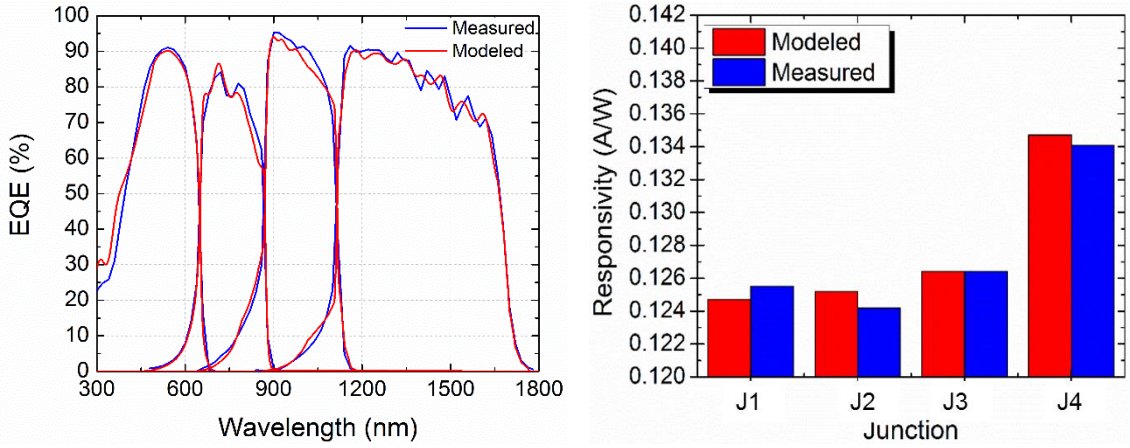

(a) (b)

Figure 4.3. a) Measured vs. modeled EQE of the wafer-bonded 4J cell developed by Soitec and the Fraunhofer ISE, b) Corresponding modeled vs. measured responsivity obtained by integrating the EQE data. Experimental data from [65].

4.2.3. Optimization process

Based on the close agreement between modeled and experimental data, this optical model was used to improve the structure design, with the main goal being to improve the current matching. As shown in the example presented in Figure 4.3, J4 (bottom cell) overproduces current with regards to the other three junctions. Several optimization processes were performed throughout this work to optimize and maximize the current distribution within each subcells. This includes optimizing the thickness of different layers within the stack or using materials with different bandgaps so that a specific layer absorbs/transmits more of the incident light.

Another area of optimization relied on the reduction of front surface reflection. Figure 4.4a also proves the ability of the model to accurately model the reflectance. Minor differences arise from inaccuracies in some of the optical constants used in the model. This model was then also used to optimize the design of the antireflective coating layers. An example of a contour plot showing an optimum MgF_2/Ta_2O_5 thickness combination is shown in Figure 4.4b.

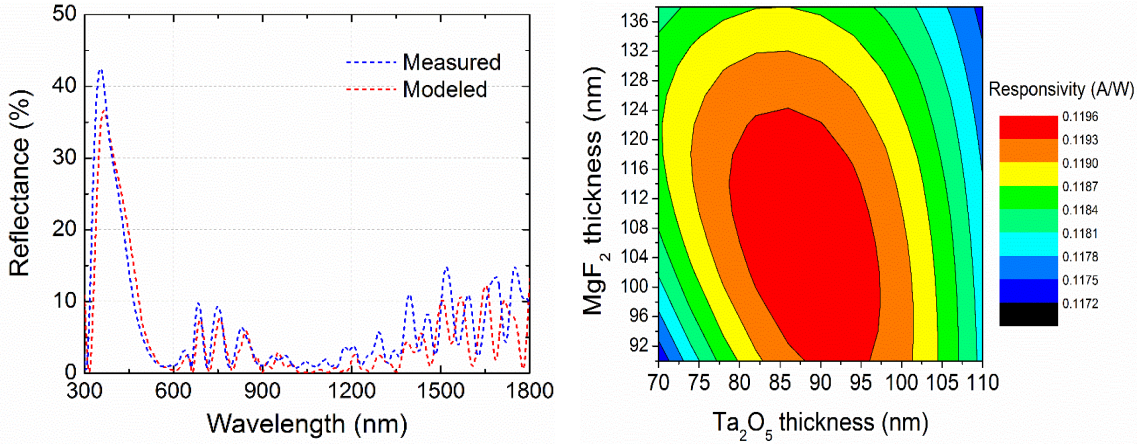

(a) (b)

Figure 4.4. a) Comparison between measured and modeled reflectance, b) Contour plot showing the optimization process of a MgF_2/Ta_2O_5 antireflective coating. The resulting responsivity is shown on the right hand side of the figure.

4.3. Effect of temperature on solar cell performance

4.3.1. Introduction

The performance of solar cells can strongly be affected by the operating or ambient cell temperature. For starters, an intrinsic property of semiconductor materials is that the bandgap shrinks with temperature. This directly results in an increase of the photocurrent generated by the solar cell (*i.e.*, increased J_{sc}). On the other hand, increase in temperature leads to an exponential increase in the dark saturation current which ultimately reduces the open-circuit voltage. The behavior of III-V solar cells operating at elevated temperatures has been studied in details in this work on GaAs single-junction solar cells up to 450°C [66]. These temperatures are far above conventional operating temperatures (concentrator cells operate somewhere around 70 – 80°C), but correspond to the operating temperatures that these devices would be subject to in various space missions (for instance the Mercury mission would involve temperatures around 270˚C [67] while the Solar Probe Plus mission would involve temperatures as high as 1400˚C [68]) and in hybrid concentrated

photovoltaic thermal (c-PVT) systems which are typically designed to operate at temperatures greater than 400°C [69]–[72]. Philipps *et al.* previously reported the measurement and simulation of the EQE and I-V of GaAs solar cells up to 400 K [73][74]. In the present work, we extended the temperature range up to 450°C (~ 723 K) although major performance degradation was observed above 350°C, which is discussed next.

4.3.2. Temperature-dependence of solar cell parameters

As was described in section 4.1. the main parameters that describe the solar cell performance are the short-circuit current density J_{sc}, the open-circuit voltage V_{oc}, the fill factor FF and the solar cell efficiency η. Each parameter will be affected by change in temperature and this is caused by the intrinsic properties of semiconductor materials.

The temperature dependence of the bandgap is usually described using Varshni's formula [75]:

$$E_g(T) = E_g(0) - \frac{\alpha T^2}{T+\beta} \tag{4.7}$$

where α and β are material constants and E_g (0) is the bandgap at 0 K. For GaAs, E_g (0) = 1.519 eV, α = 0.54 meV/K and β = 204 K [75]. The change in bandgap with temperature will directly affect the J_{sc}, i.e., an increase in temperature will lead to a decrease in bandgap and thus increase in J_{sc}. The J_{sc} can either be directly extracted from light IV measurements or can be calculated by integrating the EQE data using Eq. (4.6). Change in J_{sc} will directly affect the V_{oc}:

$$V_{oc}(T) = \frac{kT}{q} \ln\left(\frac{J_{sc}(T)}{J_0(T)}\right) \tag{4.8}$$

Note that the temperature-dependence of the V_{oc} not only depend on the J_{sc} but also (and mainly) on the dark saturation current density J_0, which is defined as:

$$J_0(T)=q\left(\frac{D_n}{L_n N_A}+\frac{D_p}{L_p N_D}\right)n_i^2(T) \quad (4.9)$$

where $N_{A,D}$ is the acceptor or donor doping density, $D_{n,p}$ is the electron or hole diffusivity and $L_{n,p}$ is the electron or hole diffusion length. These values were extracted from a PC1D model. The dominant term driving the dark saturation current is the intrinsic carrier concentration n_i defined as:

$$n_i(T)=\sqrt{N_c(T)N_v(T)}e^{-E_g(T)/2kT} \quad (4.10)$$

Note that the n_i is exponentially dependent on the bandgap which also means that the dark saturation current is also exponentially dependent on the bandgap.

4.3.3. Experimental details

In order to study the effect of high temperature on the solar cell performance, GaAs single-junction cells were investigated at elevated temperatures. The structure of the cells was presented in the original paper [66]. A hot stage from Linkam Scientific Instruments was used to measure the cells at elevated temperatures. Both the EQE and IV measurements were recorded as a function of temperature. The experimental setup did not allow for the simultaneous acquisition of the temperature-dependent EQE and IV, therefore these measurements were performed separately on different cells from the same wafer (only three cells were available at the time of the experiment). Temperature-dependent EQE is reported thereafter on Cell 1 while temperature-dependent IV are reported thereafter on Cell 2 and Cell 3.

The temperature of the stage was increased from room temperature to 450°C in steps of 25 – 50°C with a ramp rate of 10°C/min. Once the desired temperature was reached the sample was kept at the specified temperature for another 3 min.

4.3.4. Experimental results

The temperature dependence of the bandgap was measured by comparing the change in bandgap from EQE measurements on Cell 1 and the value expected from Eq. (4.7). Note that the bandgap values were calculated by looking at the first derivative dEQE/dλ and taking the wavelength at which the derivative peaks as the bandgap.

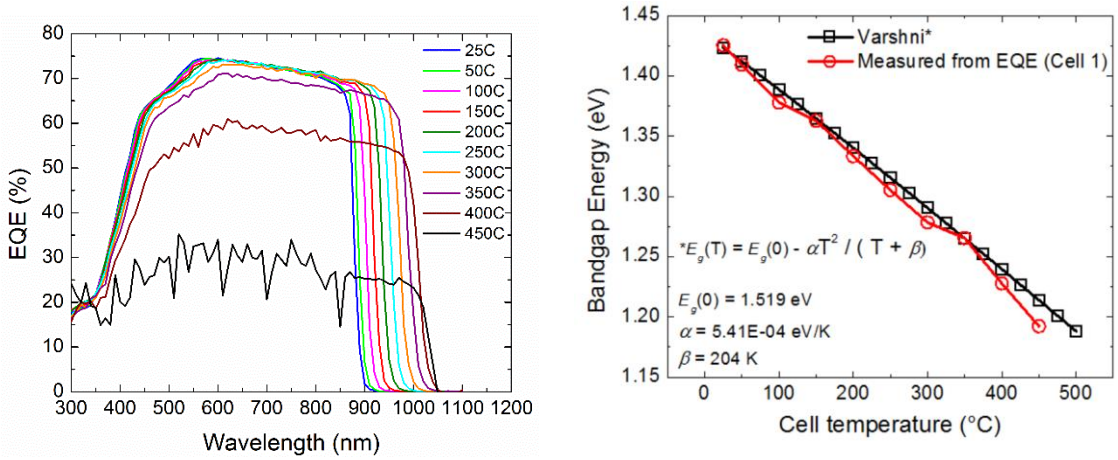

(a) (b)

Figure 4.5. a) Temperature-dependence of the EQE of Cell 1, b) Change in bandgap with temperature compared to Varshni's equation. The bandgap values were extracted from the EQE.

As shown in Figure 4.5a, we observed an inconsistent behavior in the low wavelength range (300 – 350 nm). The EQE slightly increased for T < 200°C and then decreased as the temperature was further increased. Similar to what has been previously reported [73][74], the EQE shifts consistently above 350 nm and the band gap moves towards longer wavelengths as the temperature is increased following the behavior predicted by Varshni's equation (Figure 4.5b). This furthermore confirms that the cell's

temperature is close to that of the stage's thermocouple. The EQE dropped drastically and the signal became very noisy for temperatures above 350 °C suggesting that shunting effects started to kick in [66].

The temperature-dependent dark- and light IV characteristics of Cell 3 are shown in Figure 4.6. As shown in in Figure 4.6b, a gradual decrease in V_{oc} is observed with temperature. This is a result of the exponential increase in the dark saturation currents due to the decrease in bandgap with temperature. The J_{sc} is found to increase up to 275°C after which, due to the gradual decrease in shunt resistance with temperature, the cell becomes completely shunted at around 350°C and results in a strong J_{sc} drop. This is coherent with the shunting observed in the EQE measurements. The DIV measurements will be discussed in the next section.

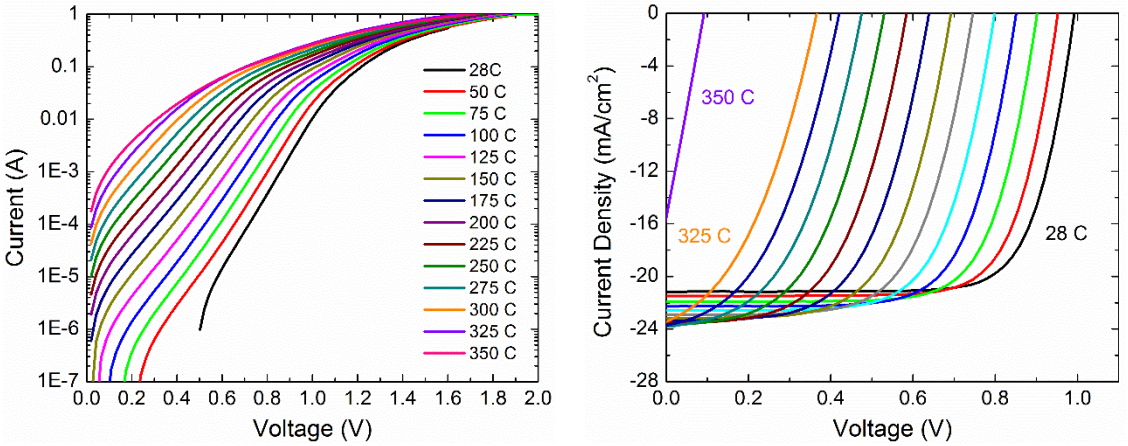

(a) (b)

Figure 4.6. Temperature-dependent measurement of a) the DIV and b) the LIV characteristics of Cell 3.

4.3.5. Modeling

DIV measurements are extremely helpful in assessing the diode properties of a solar cell. In this work, a two-diode model was used to extract various cell parameters from DIV

measurements. Figure 4.7 shows the accuracy of the fit for a room temperature measurement. A Matlab program was used to perform the fitting [76].

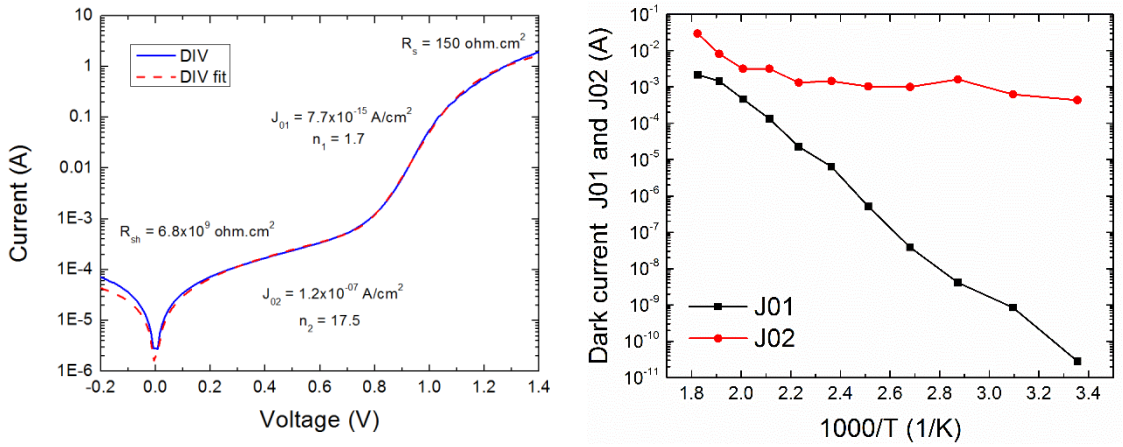

(a) (b)

Figure 4.7. a) Comparison between measured and fitted DIV at different temperatures, b) Extracted dark saturation current from DIV fitting.

In addition, the electrical and optical characteristics of the devices under investigation were simulated using Silvaco ATLAS simulation software. The results of these simulations are presented in Figure 4.8. More details were presented in Ref [66].

As shown in Figure 4.8, the peak EQE drops at 350°C when compared with room temperature which is also well reproduced by simulation. This drop in EQE is most probably caused by the decrease of minority carrier lifetime at high temperature. However there appears to be slight discrepancies between experimental data and simulation results most likely caused by inaccuracies of the optical data or mobility models of the different materials used in the simulation. A good agreement was obtained between measured and simulated IV curve as shown in Figure 4.8. From 28°C to 325°C, J_{sc} increases but V_{oc} decreases due to a smaller bandgap. The decrease in FF is mainly controlled by the

degradation of $V_{oc.}$ Degradation of mobility and lifetime at high temperature will also have detrimental influence on the solar device performance.

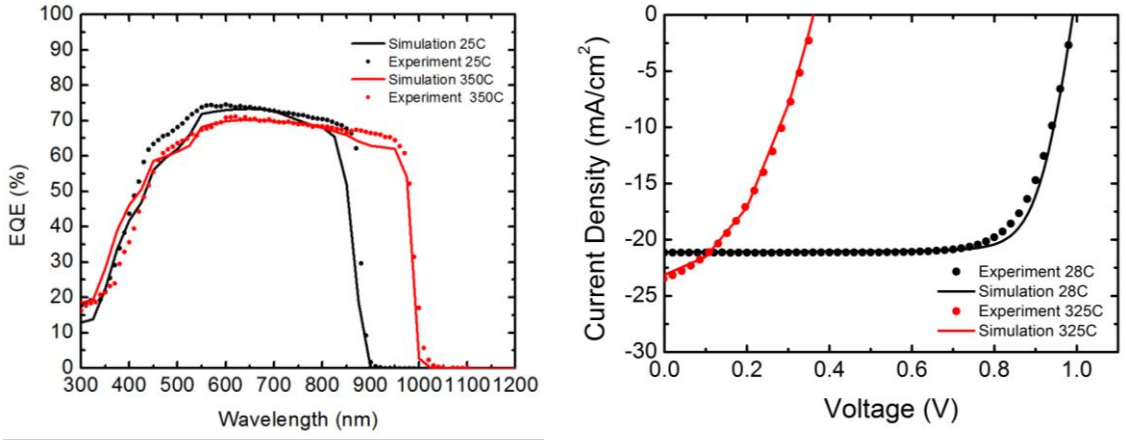

(a) (b)

Figure 4.8. a) Measured and simulated EQE versus wavelength at 25 °C and 350 °C, b) Experimental and simulated IV curves of the investigated GaAs solar under illumination at 28 °C and 325 °C.

4.3.6. Summary

The characteristics of GaAs single-junction solar cells were studied as function of temperature up to 450°C to investigate their potential use in harsh space environment and possibly in hybrid PVT systems where such temperatures are commonly encountered. As a result of the decrease in bandgap with temperature, the J_{sc} increased and the V_{oc} decreased accordingly until shunting effects started to degrade the cells characteristics at temperatures above 350°C after which the cells completely failed. Once cooled back to room temperature, the EQE and thus, the J_{sc}, partially or fully recovered depending on the cells whereas the V_{oc} showed an irreversible loss in all the cells. The shunting is believed to be caused by Au diffusion from the contacts into the GaAs pn junction. A better design of the metal contacts using a diffusion barrier and/or an encapsulant should improve the performance of GaAs solar cells at elevated temperatures.

CHAPTER 5

STRUCTURAL INVESTIGATION OF GaInAs AND GaAsSb

Although the ultimate goal of this work was to produce lattice-matched GaNAsSb materials to produce high efficiency solar cells, it is expected that the introduction of nitrogen into Ga(In)As(Sb) will strongly affect the optical and structural properties of the materials. It was thus extremely important to first develop a good understanding of the properties of N-free materials. This chapter will discuss the growth mechanism of strained GaInAs and GaAsSb on GaAs by investigating the structural properties of these materials prior to introducing nitrogen. Moreover, the use of strained materials such as GaInAs/GaAs and GaAsSb/GaAs has prompted strong interest from the optoelectronics community for the realization of long wavelength photodetectors and laser diodes [77]–[80]. These materials have also attracted a great deal of interest for photovoltaic applications where GaInAs is often used as one or several of the absorber materials in inverted metamorphic multijunction solar cells [81], [82]. GaAsSb has also been used as a barrier material in quantum dot solar cells [83]. Therefore the study of these N-free materials still has clear implications for the development of high performance optoelectronic devices.

5.1. Sample description

Three sets of samples were investigated. Set A consists of GaInAs structures grown with ~ 7 – 8 % In and thicknesses ranging from 50 nm to 2 µm. Similarly, set B consists of GaAsSb films grown with ~ 8 % Sb and thicknesses ranging from 100 nm to 2 µm. Finally, set C consists of 50 nm thick GaAsSb films in which the Sb composition was gradually increased from 2.7 to approximately 16 %. All structures have a 50 nm GaAs

cap layer and were nominally undoped. The V/III BEP ratio was set to about 15 while the growth rate used was typically 0.37 and 0.72 μm/hr for the GaInAs and GaAsSb films respectively. The different thicknesses and compositions were chosen in order to provide samples with different levels of initial elastic strain and are summarized in Table 5.1. As described in CHAPTER 2, strained materials can only be grown pseudomorphically up to their critical thickness, after which it becomes energetically favorable to generate misfit dislocations to relieve the misfit strain [35]. Extended defects introduce non-radiative recombination centers which degrade the optical quality of these materials and thus must be avoided and/or minimized.

Table 5.1. Details of the sample structures for the different GaInAs and GaAsSb films. The thickness, composition and extent of relaxation were determined from XRD measurements.

Sample ID	Epitaxial layer	Thickness (nm)	In/Sb composition (%)	Initial misfit (%)	Relaxation (%)
A1	GaInAs	50	7.3	0.523	0
A2	GaInAs	125	7.35	0.527	0
A3	GaInAs	250	7.35	0.527	46
A4	GaInAs	500	7.3	0.523	64
A5	GaInAs	1000	7.8	0.559	76
A6	GaInAs	2000	8.4	0.602	78
B1	GaAsSb	100	7.7	0.603	0
B2	GaAsSb	250	7.1	0.556	42
B3	GaAsSb	500	7.4	0.579	68
B4	GaAsSb	1000	8.7	0.681	75
B5	GaAsSb	2000	8.3	0.650	81
C1	GaAsSb	50	2.7	0.211	0
C2	GaAsSb	50	4.6	0.360	0
C3	GaAsSb	50	6.5	0.509	0
C4	GaAsSb	50	9.4	0.736	0
C5	GaAsSb	50	12.2	0.955	0
C6	GaAsSb	50	16	1.253	17

5.2. High Resolution X-ray Diffraction analysis

XRD was first used to identify the composition and thickness as well as to specify the presence (or absence) of extended defects in the each sample. The ω-2θ double-crystal

scans measured in the vicinity of the (004) GaAs reflection are shown for all three sets of samples in Figure 5.1. These curves were fitted using the X'Pert Epitaxy software in order to obtain the composition and thickness, which have been summarized in Table 5.1. Structures from sets A and B with film thicknesses of 125 nm or below and structures from set C having a Sb composition of 12.2% or lower demonstrate strong Pendellösung (interference) fringes indicative of good material quality and therefore, low deterioration of the scattered X-ray beam at the interface. As the thickness and/or composition were increased these interference fringes disappeared and the epitaxial layer peak appeared to broaden and gradually shift towards the GaAs substrate peak. These observations revealed partial relaxation of the films due to the creation of 60° type dislocations. Additionally, as the layer thickness increases in the samples of sets A and set B, one can notice the appearance of a peak on the right hand side of the GaAs substrate peak. This additional peak corresponds to the GaAs cap layer which is now subject to tensile stress with regard to the partially relaxed epitaxial layer underneath.

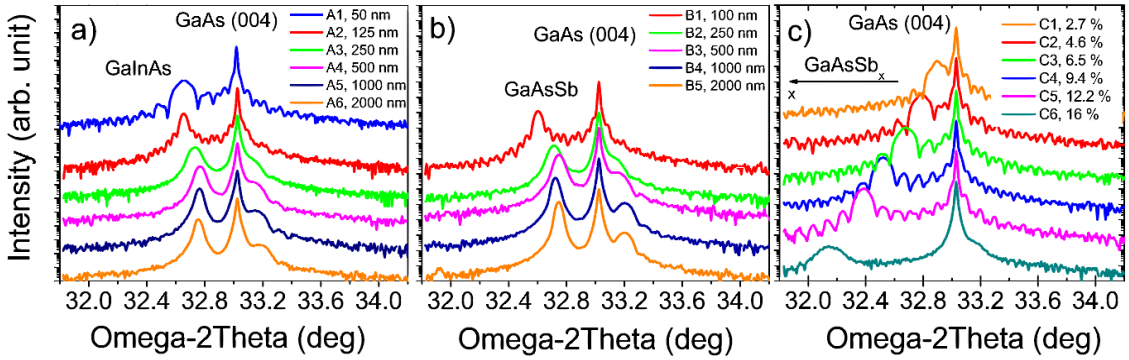

Figure 5.1. HR-XRD ω-2θ scans measured in the vicinity of GaAs (004) reflection for samples of a) set A, b) set B and c) set C [27].

ω rocking curves were collected in triple-crystal mode around the epitaxial layer peak. Similar to the what was found in the ω-2θ scans, Figure 5.2 shows that for structures below 125 nm thick in set A and set B, and compositions below 9.4 % in set C, the ω rocking curves appear as a sharp central coherent peak whose full-width-at-half-maximum (FWHM) was found to be limited by the XRD system resolution. As the thickness and/or composition are slightly increased, diffuse scattering appeared on the tails of the central peak indicating the creation of 60° misfit dislocations [27], [46], [84], [85]. However their density and induced elastic strain must remain below the specific level for deterioration of vertical coherence since the ω-2θ RC of these samples presented in Figure 5.1 showed well defined and extended interference fringes. Further increase of the thickness or composition resulted in a broadening of this diffuse scattering and a suppression of the central coherent peak as a result of strain relaxation and hence increased density of dislocations and volumetric elastic strain [86].

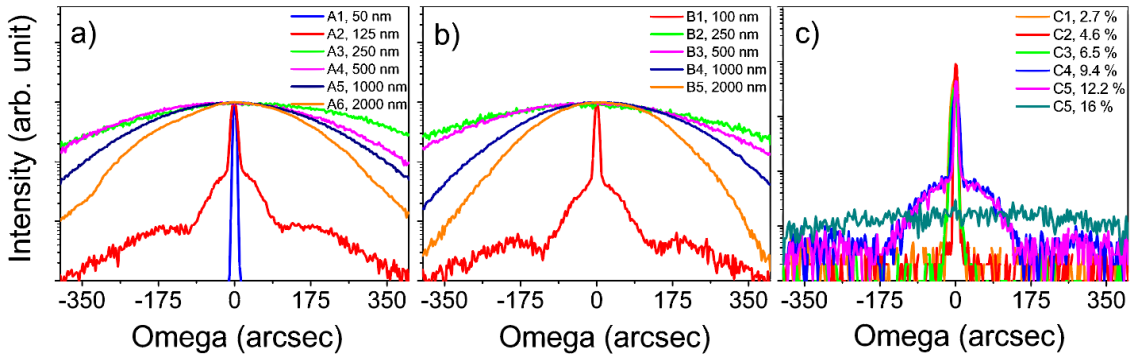

Figure 5.2. HR-XRD ω rocking curves measured around the epitaxial layer of samples from a) set A, b) set B and c) set C. The appearance of diffuse scattering on each side of the central peak indicates onset of stress relaxation and the creation of 60° dislocations [27].

5.3. XRT analysis

In order to confirm that the appearance of diffuse scattering in the XRD ω rocking curves indicates the creation of 60 misfit dislocations [46], [84], [85], X-ray topography images were collected on three GaInAs samples (A1, A2 and A3) which presented very distinct ω rocking curves. Figure 5.3 presents the XRT images of these samples [27].

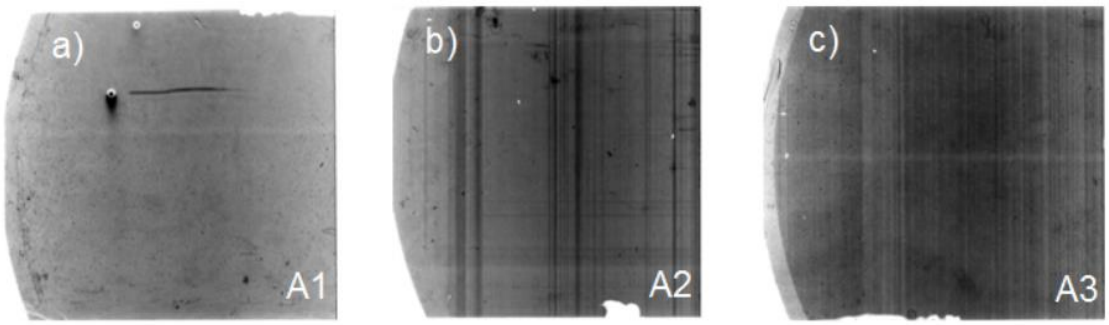

Figure 5.3. XRT images of GaInAs samples with different ω RC characteristics. Sample A1 appears free of dislocations (a) while dislocation lines are clearly visible in samples A2 (b) and A3 (c) [27].

While sample A1 appears to be free of extended defects (note that the line and bubble like features are the results of surface damage), dislocation lines are clearly visible in samples A2 and A3. These results confirm the observations made from the triple-axis ω rocking curves in Figure 5.2 which allowed us to correlate the appearance of diffuse scattering on the rocking curves with the creation of the first 60° dislocation loops [27].

5.4. TEM analysis

Although XRT confirmed the presence of 60° dislocations, it only provides us with a visual observation of the dislocation near the surface. In order to specify where in the structures these dislocations formed, cross-section TEM images were collected. Sample C5 (50 nm $GaAsSb_{0.122}$) was investigated first. Two 60° dislocations, shown by the arrows in Figure 5.4, with a spacing of 490 nm were observed in the cross-section [27]. The presence of dislocations in this structure was expected as the ω rocking curve demonstrated the presence of both a sharp peak and diffuse scattering (see Figure 5.2).

Figure 5.4. Cross-section TEM image of sample C5 (50 nm thick GaAsSb0.122). The arrows point at the 60° misfit dislocations observed at the bottom GaAs/GaAsSb interface. The dislocation spacing is about 490 nm. The dashed lines are guides to the eye to show the top and bottom interfaces [27].

We also chose to investigate a structure that demonstrated an ω rocking curve with a broad diffuse scattering only. The images presented in Figure 5.5 were collected on sample B5 (2000 nm thick $GaAsSb_{0.083}$) which revealed that all the extended defects are located at the top and bottom interfaces, GaAsSb/GaAs and GaAs/GaAsSb respectively, with no threading dislocation segments propagating in the volume of the epitaxial layer [27].

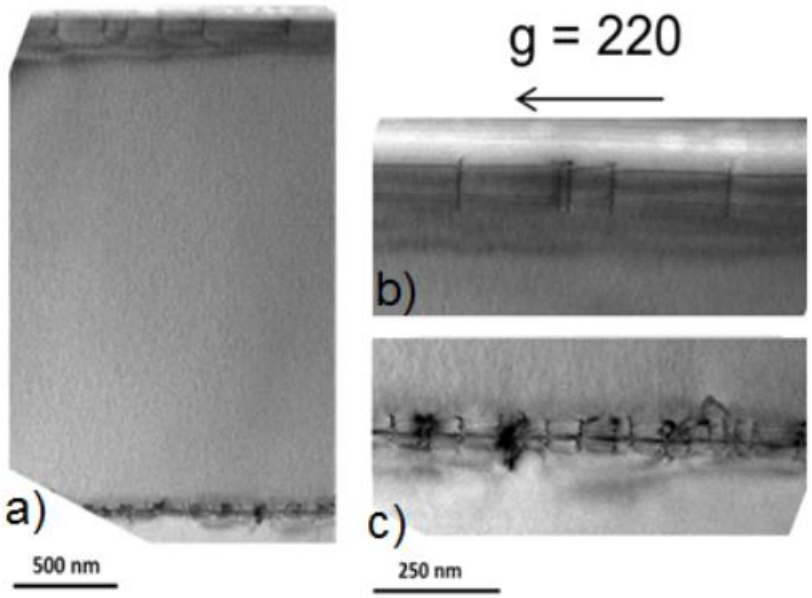

Figure 5.5. a) Cross-section TEM images of sample B5 (2000 nm thick GaAsSb0.083). The top epilayer/cap and bottom buffer/epilayer interfaces are shown in Fig. 5 (b) and (c) respectively. Misfit dislocations are present at both interfaces and no threading dislocation segments are observed in the volume of the epitaxial layers [27].

We should note that the presence of misfit dislocations (most probably 60° type) at the top GaAsSb-GaAs cap interface is not surprising as the ω-2θ scans (Figure 5.2b) showed a shoulder peak on the right hand side of the GaAs (004) substrate peak which indicated that the top GaAs cap layer started to become tensile strained to the underlying GaAsSb layer.

5.5. Strain relaxation

We showed in CHAPTER 2 that according to the equilibrium theory of critical thickness, misfit dislocations form as a result of strain relaxation [35]. In the previous sections we were able to use XRD ω rocking curves in conjunction with XRT as well as TEM to specify which samples were free of dislocations (i.e., those whose ω rocking curves present a sharp peak only), and which samples were not (i.e., all the others).

In order to obtain more information about the crystal structure of the films and especially to determine the amount of strain relaxation, we used asymmetrical (224) reciprocal space mapping. Asymmetrical reflections were used to calculate the in-plane and out-of-plane lattice constant and mismatch which were used to calculate the extent of strain relaxation. The lattice constant was also used to calculate the In or Sb compositions in each sample using Vegard's law. Figure 5.6 shows the (224) RSM for three GaAsSb samples of different thicknesses, B2 (100 nm), B3 (250 nm) and B5 (2000 nm). The horizontal Q_x and vertical Q_y axes represent the directions normal to $(1\bar{1}0)$ and (001) planes, respectively. In particular, Figure 5.6 shows that for sample B2, there is no difference in the in-plane direction, and the GaAs and GaAsSb diffraction spots are well aligned along the Q_x direction. However, both spots are well separated along the Q_y axis. The ΔQ_y indicates that the GaAsSb is subject to an out-of-plane mismatch of 1.14 %. This ultimately indicates that the GaAsSb film remains coherently strained to the GaAs substrate. This was somewhat surprising since misfit dislocations were found to form in this structure (see the diffuse scattering in ω rocking of Figure 5.2), and therefore strain relaxation should have "visually" started. Nevertheless, inspecting the (224) RSM of the thicker structures B3 and B5 revealed that strain relaxation clearly occurred in these structures. In both structures, the GaAs and GaAsSb diffraction spots are again well separated in the Q_y direction, which indicates again that there is still some out-of-plane mismatch in these samples (0.87 % and 0.77 % in B3 and B5 respectively); however the two diffraction spots are no longer aligned along the Q_x direction, indicating that these films are now also subject to an in-plane mismatch (0.19 % and 0.53 % in B3 and B5 respectively). This reveals that strain relaxation has now occurred, however full relaxation

was not achieved even in the thicker structure. Sample B3 relaxed about 34 % while sample B5 relaxed about 81 %. Similar observations were found for the GaInAs structures [27]. A 4 µm-thick sample was also investigated and revealed that only 92 % of relaxation occurred. This reveals that full relaxation by 60° type dislocations is very difficult to reach. As the thickness was increased, the GaAs diffraction spot was also found to elongate and eventually align with the GaAsSb epilayer peak. This again relates to the GaAs cap layer becoming coherently strained to the epilayer underneath, as observed in Figure 5.1.

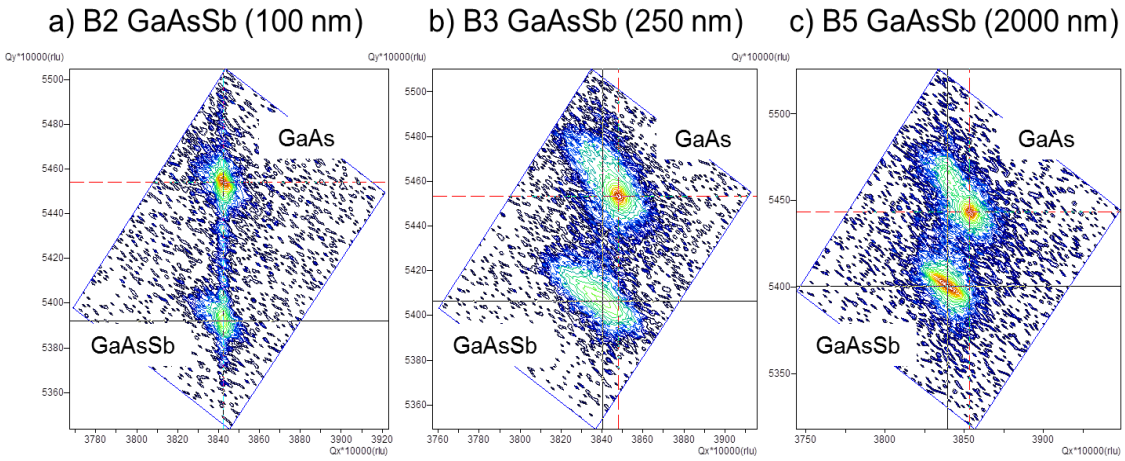

Figure 5.6. Asymmetrical reciprocal space maps measured around the (224) diffraction conditions for GaInAs structures a) B2, b) B3 and C) B5. B2 appears to remain coherently strained while B2 and B5 partially relaxed. The diffraction spot above the GaAs (224) spot in Figs. b) and c) corresponds to tensile stressed top GaAs layer [27].

5.6. Discussion

Ultimately, the formation of misfit dislocations happens at the so-called critical thickness. This term, “critical thickness”, has been widely used and studied over the years although we should use this term with caution as it depends strongly on the growth conditions and it is therefore very difficult to provide a universal critical thickness for a given material. The theory was reviewed in CHAPTER 2 where it was shown that Fitzgerald provided a slightly more accurate definition of the critical thickness for the

materials that we investigated (*i.e.*, III-V materials are in general anisotropic). Figure 5.7 shows the predicted critical thickness for our samples. Also shown are the three sets of samples that we investigated. Filled markers correspond to samples that remained almost or fully strained while open markers correspond to samples that have partially relaxed.

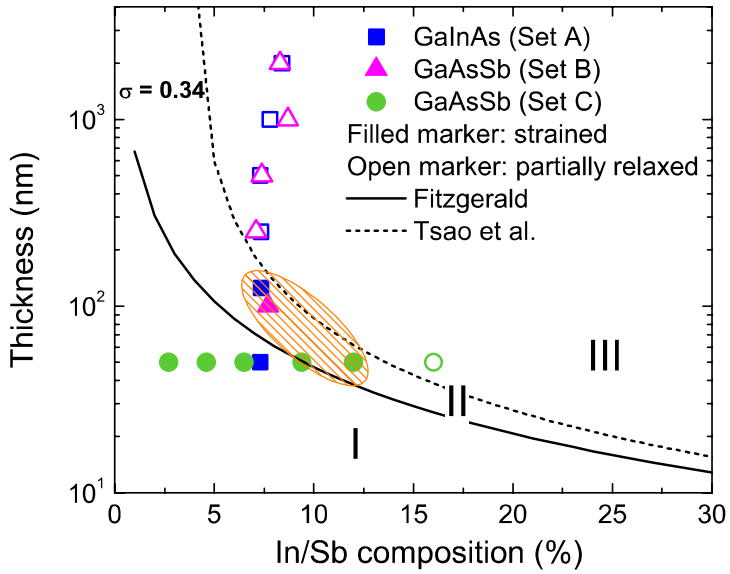

Figure 5.7. Critical thickness plot of the GaInAs and GaAsSb structures investigated in this work [27]. Results from the three sets of samples (A, B and C) are compared to models from the equilibrium theory [35] and Tsao et al. [62].

The samples shown in the orange area indicate samples in which misfit dislocations were found but as revealed by the asymmetrical (224) RSM, strain relaxation did not necessarily occur. There have been many reports showing that although the critical thickness for the onset of misfit dislocations formation could indeed be explained by the equilibrium theory, the resulting strain relaxation only occurred for layer thicknesses well above the equilibrium theory [87]–[89]. This appears to be the case in our materials as well. Several models have then been proposed to explain these inconsistencies.

For instance, Tsao et al. considered the kinetics processes associated with the plastic deformation of a material [90]. Their approach shows the onset of strain relaxation

to be linearly shifted from the equilibrium value and this linear offset was directly related to what they define as an excess stress. Once this excess stress exceeds a critical value, which they relate to the growth temperature, strain relaxation is inevitable. Although this study was done on SiGe, it appears to be very similar to what we observed in our GaInAs and GaAsSb samples. We therefore decided to apply this theory to our materials.

The excess stress σ_{exc} corresponds to the difference between the misfit stress which promotes the elongation of the dislocation along the substrate-film interface and the effective stress related to the dislocation-line tension and is directly related to the growth temperature [90]. The limit for observable strain relaxation is then obtained by solving [90]:

$$F_{exc} = F_e - nF_l = \frac{hb\sigma_{exc}}{2} \tag{5.1}$$

Using Eqs. (2.2) and (2.5) we can express the excess stress term and calculate the resulting critical thickness as follow:

$$\sigma_{exc} = Y\epsilon - \frac{nD}{h}(1-\nu\cos(\alpha)^2)\left[\ln\left(\frac{h}{b}\right)+1\right] \tag{5.2}$$

In the case where $\sigma_{exc} = 0$, Eq. (5.2) simply reduces to the critical thickness predicted by Eq. (2.8). For nonzero excess stress it is equivalent to linearly offsetting the equilibrium curve towards higher misfits. In our case for both GaAs/GaInAs/GaAs and GaAs/GaAsSb/GaAs grown at 500 °C strain relaxation seems to be inevitable once σ_{exc} becomes greater than 0.34. According to Tsao's theory the materials remain stable as long as the layer thickness is kept below the equilibrium limit (*i.e.*, for $\sigma_{exc} \leq 0$), which was identified as stage I in this work. For σ_{exc} greater than zero, the materials are considered to

be in a metastable state (*i.e.*, stage II) until a critical excess stress value is reached. At stage III the critical excess stress becomes sufficient enough to lead to observable plastic deformation. After this point, further deformation of the film is believed to be the result of structural transformation of diffused and accumulated point defects, which leads to the multiplication of dislocations and significant strain relaxation [90]. These different stages are represented in Figure 5.7.

5.7. Summary

XRD was used in conjunction with XRT and TEM in order to investigate how, when and where defects form during the growth of strained materials. It was found that strain accommodation occurs in three stages which can be simply identified by the shape of the XRD ω rocking curves. Strain relaxation was found to happen at thicknesses slightly above the critical thickness. A slight modification of the equilibrium theory was proposed to determine the maximum thickness allowed before observable strain relaxation becomes inevitable. All the samples grown under the critical thickness were found to be free of extended defects and should therefore only be considered in order to realize high quality materials.

CHAPTER 6

OPTICAL INVESTIGATION OF GaAsSb

In this chapter, we will investigate the temperature- and power-dependent photoluminescence (PL) characteristics of GaAsSb/GaAs heterostructures. The samples studied are those referred to as set C for which details were presented in the previous chapter. For simplicity we will refer to these samples in this chapter as S1, S2, S3, S4, and S5, respectively. As described earlier, these structures consisted of a 300 nm GaAs buffer layer, followed by a 50 nm $GaAs_{1-x}Sb_x$ epilayer with Sb composition ranging from 2.7 to 12.2% and capped with a 50 nm GaAs layer. The growth temperature of the GaAsSb layers was set to 500°C while the GaAs buffer and cap layers were grown at 600°C and 585°C respectively. Power- and temperature-dependent PL were used to investigate the optical properties of these structures. Carrier localization effects were found to occur as a result of compositional fluctuations [28]. The details are discussed in the next sections.

6.1. Unusual PL behavior

The temperature-dependent PL spectra are shown for samples S2 (4.6 % Sb) and S5 (12.2 % Sb) in Figure 6.1 for two different excitation intensities (38 and 188 W/cm^2). It was found that for the low Sb-containing samples (below 6.5%), the PL was composed of only one peak over the whole temperature range investigated, for both low (38 W/cm^2) and high (188 W/cm^2) excitation intensity, as shown in Figure 6.1a and Figure 6.1b for the 4.6% Sb sample S2. For higher Sb-containing samples, a second peak located on the high energy side appeared at T ~ 30 K under low excitation intensity and started to dominate as the temperature was further increased (Figure 6.1c). Under high injection, the low-energy

peak does not appear (Figure 6.1d). It can also be noted that increasing the excitation intensity led to a slight blue shift of the PL peak at low temperatures in both samples.

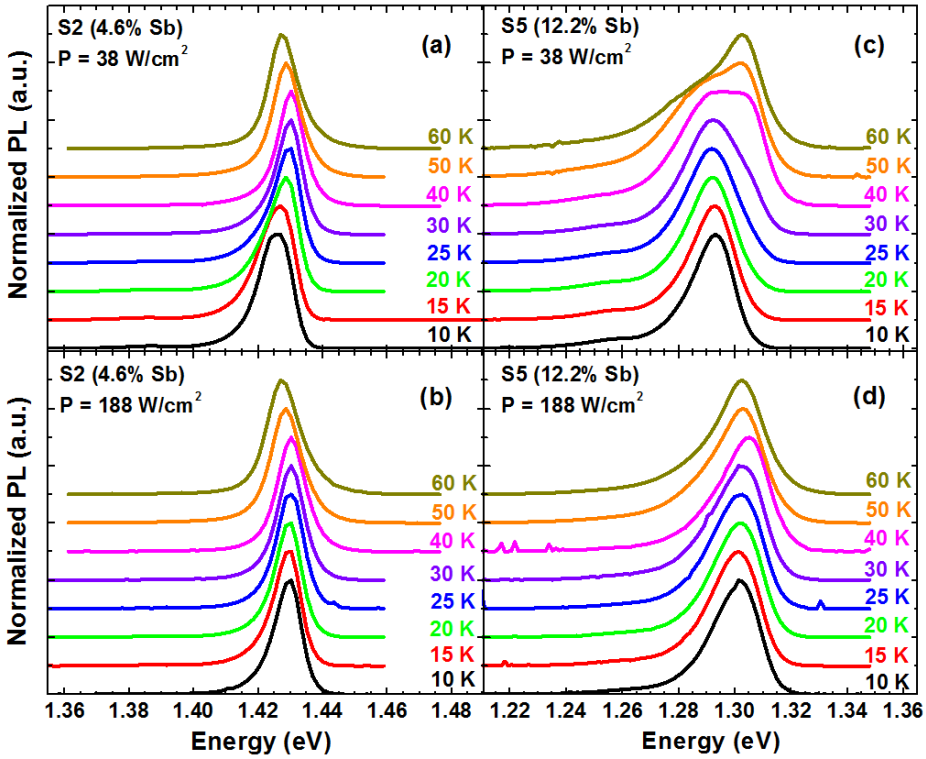

Figure 6.1. PL spectra as a function of temperature measured under different excitation intensities for strained 50 nm thick samples with a) and b) 4.6 % Sb, c) and d) 12.2 % Sb [28].

6.2. Low-temperature S-shape behavior

In order to investigate the origin of this higher energy peak, the PL peak position was plotted for samples with different Sb compositions as a function of temperature and excitation intensity. As shown in Figure 6.2 for samples S2, S4 and S5, the PL peak energy presents an S-shape behavior (red/blue/redshift) that becomes more pronounced at higher Sb compositions and lower excitation intensities. This type of behavior is a well-known characteristic of carrier localization effects generally associated with sub-bandgap potential fluctuations induced by strain or compositional inhomogeneity, crystal defects, interface roughness, and/or fluctuation in quantum well width [91][92]. These different

sources of disorder can locally modify the valence and conduction bands by creating irregular fluctuations of the electrostatic potential. As a result, at low temperature and low excitation intensity, excitons thermalize and relax to local minima where they get trapped, which results in the first minimum (red shift) of the PL peak energy. With further increase in temperature, the carriers gain enough thermal energy to be transferred to higher energy states in the band tail until they finally reach the conduction band edge, thus leading to a maximum (blue shift) in the PL peak energy. Finally when the temperature is high enough the carriers are thermally activated which prevents them from localization. Consequently they can recombine freely which in turns results in the second red shift of the PL peak energy.

In particular, as the Sb composition is increased the S-shape becomes more pronounced and the temperature at which the second redshift begins increases with Sb compositions. This reveals that increasing the Sb content results in deeper confinement potentials. Then, higher temperatures are needed to de-trap the carriers from these deep potential wells [93]. Figure 6.2 also shows that as the excitation intensity increases, the amplitude of the observed blue shift decreases. This phenomenon is attributed to electrostatic band bending and band filling effect of the localized states [94]. As the excitation intensity increases, the lower energy states in the band-tail are gradually filled until reaching saturation in which case all states are occupied and the recombination of free carriers start to dominate. In that case, the recombination of localized states saturate quickly and it becomes impossible to dissociate their contribution to that of the free carriers from the PL spectra, which explains why samples with strong localization demonstrate PL spectra with only one peak under high excitation intensity (Figure 6.1d).

Furthermore, Figure 6.3 shows the temperature dependence of the full width at half maximum (FWHM) for structures S2, S4 and S5 for the different excitation intensities used. The FWHM of all three samples present an inverted S-shape behavior, which is especially more pronounced at lower excitation intensity and which, once again, confirms the presence of a competition process between the recombination of localized excitons (LE) and free excitons (FE). It has been shown that the temperature for which this competition process between localized and free excitons is maximum can be obtained from the FWHM peaks [91]. In our case, the FWHM peaks occur at 15 K, 25 K and 50 K for samples S2, S4 and S5 respectively. This correlates well with the gradual increase in compositional disorder in these three samples. Additionally we can note a gradual increase of the FWHM as the Sb composition is increased.

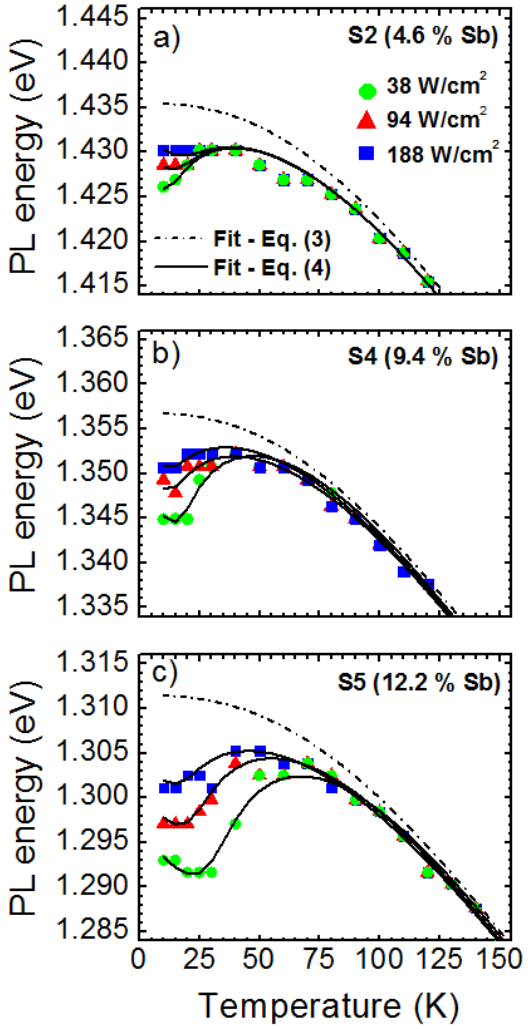

Figure 6.2. PL peak energy as function of temperature and excitation intensity of the $GaAs_{1-x}Sb_x/GaAs$ structures S2, S4 and S5. Each symbol correspond to different excitation intensities (●: 38 W/cm^2; ▲: 94 W/cm^2; ■: 188 W/cm^2). The dashed dotted lines correspond to the fittings based on Eq. (6.1) without considering the thermal redistribution term while the solid lines correspond to the fittings based on Eq. (6.4)(6.4) including the thermal redistribution term. The fitting parameters can be found elsewhere [28].

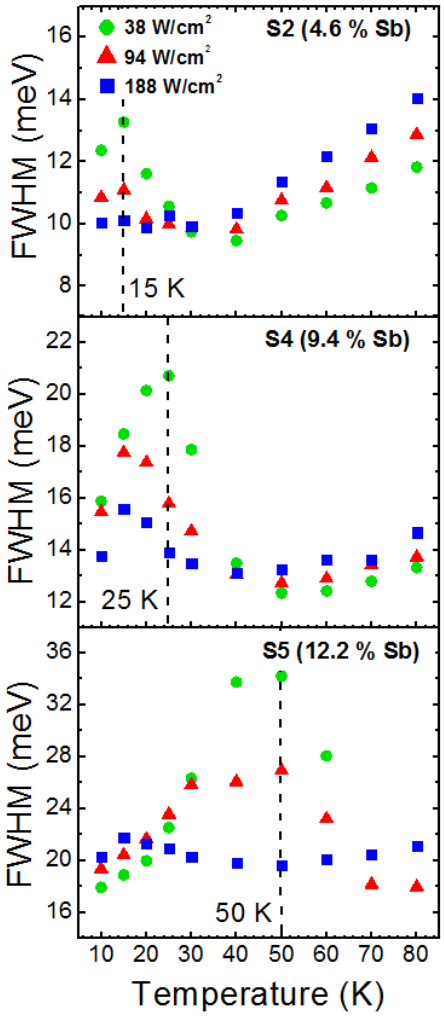

Figure 6.3. FWHM as function of temperature and excitation intensity for the GaAs1-xSbx/GaAs structures S2, S4 and S5. Each symbol correspond to different excitation intensities (●: 38 W/cm2; ▲: 94 W/cm2; ■: 188 W/cm2) [28].

6.3. Fitting of carrier localization effects

In an ideal system with no localization effects the reduction of the band gap is also temperature-dependent and is generally described using either Varshni formula [75] or the Bose-Einstein model proposed by Viña et al. [95]. Pässler provided an in-depth comparison of both models and showed that these models differ quite strongly at low temperatures [96]. Accordingly Pässler proposed a model that includes an additional empirical parameter that was not accounted for in either models which showed to provide more accurate fitting of

experimental data at low temperatures. Using Pässler's expression, the temperature-dependent PL peak energy is then described as [95]:

$$E(T) = E_g(0) - \frac{\alpha\beta}{2}\left(\sqrt[p]{1+\left(\frac{2T}{\beta}\right)^p} - 1\right) \tag{6.1}$$

where $E_g(0)$ is the bandgap energy in eV at 0 K, α is the limit value for the forbidden gap entropy at high-temperature, β is the temperature of the effective phonon with energy $\hbar\omega$ ($\beta \equiv \hbar\omega/k_B$) and p is an empirical parameter related to the shape of the electron-phonon spectral functions.

As our samples evidenced signs of carrier localization effects, it is not surprising that Eq. (6.1) does not provide a good fit of the temperature-dependent PL of our samples, as shown by the dashed lines in Figure 6.2. Li et al. developed a model that takes into consideration the process of thermal redistribution of carriers between localized states occurring in materials presenting signs of localization effects, i.e. materials whose luminescence demonstrate a strong S-shape behavior [97], [98]. In their model, the thermal redistribution of carriers within the localized states is described as:

$$E(T) = E_0 - x(T)k_BT \tag{6.2}$$

Here, x(T) is a dimensionless temperature dependent coefficient that can be obtained by numerically solving [97]:

$$xe^x = \left[\left(\frac{\sigma}{k_BT}\right)^2 - x\right]\left(\frac{\tau_r}{\tau_{tr}}\right)e^{E_0-E_a/k_BT} \tag{6.3}$$

and where E_0 is the center of the energy distribution of the localized states, E_a is the energy position of a delocalized state to which the localized carriers thermally escape while σ is

the standard deviation of the distribution. $1/\tau_{tr}$ is the escape rate, $1/\tau_r$ is the radiative recombination rate of the localized carriers and k_B is Boltzmann constant.

By combining Eqs. (6.1) and (6.2), we obtain the complete expression that describes the non-ideal temperature-dependent PL energy of a material [91]:

$$E(T) = E_g(0) - \frac{\alpha\beta}{2}\left(\sqrt[p]{1+\left(\frac{2T}{\beta}\right)^p} - 1\right) - x(T)k_BT \qquad (6.4)$$

The results of the fittings using Eqs. (6.1) and (6.4) are plotted in Figure 6.2 for each sample and for different excitation powers. It is clear that the S-shape characteristic of the PL is well reproduced using Eq. (6.4). The fitting parameters used in the calculations have been published elsewhere [28].

The degree of localization can be expressed in terms of the localization energy E_{loc}, defined as the energy difference between the first redshift and the maximum position of the blueshift. Figure 6.4 shows the evolution of E_{loc} as a function of the Sb composition and for different excitation powers in samples S1 to S5. The localization energy provides a clear visualization of the effect of the Sb composition and excitation power on the degree of carrier localization. The results suggest that these localization effects are the result of compositional fluctuations whose effect gets larger as the Sb composition increases [28].

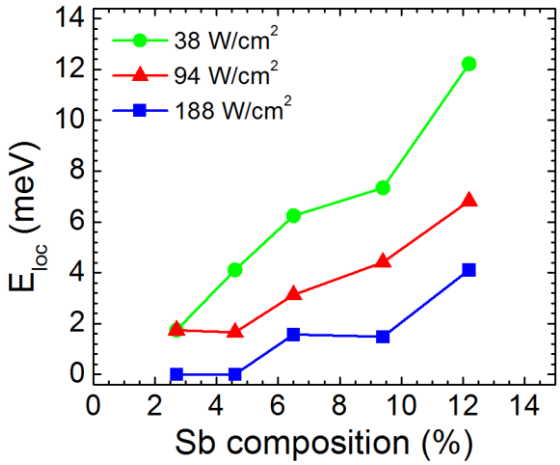

Figure 6.4. Evolution of the localization energy Eloc as a function of the Sb composition and excitation power in samples S1 to S5 [28].

6.4. Effect of growth temperature

The growth temperature of GaAsSb was chosen to be 500 °C in this work, similar to what was found optimum for the growth of high quality GaInAs QWs in our previous work [99][100]. However Sadofyev et al. reported an optimum growth temperature of 470 °C for $GaAsSb_{0.36}$ [94]. Besides the lower growth temperature, they also focused on higher Sb content (~ 36 %) which can also affect the growth conditions. In that regard, two additional samples S6 and S7 were grown at 460 °C and 420 °C respectively. In order to correlate the effect of growth temperature on these localization effects, the Sb composition was kept close to 12 % so that the results could be compared to that of sample S5 (12.2 % Sb).

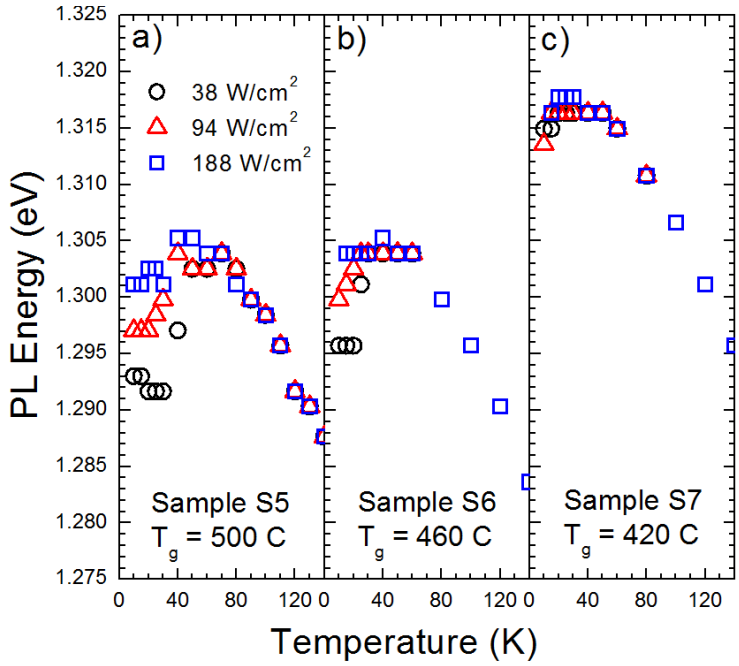

Figure 6.5. PL peak energy as function of temperature and excitation intensity of the GaAs1-xSbx/GaAs structures a) S5, b) S6 and c) S7 grown at 500, 460 and 420 °C respectively. Each symbol correspond to different excitation intensities (○: 38 W/cm2; Δ: 94 W/cm2; □: 188 W/cm^2). Lowering the growth temperature suppressed the S-shape behavior of the PL but decreased the PL intensity [28].

Figure 6.5 presents the PL peak energy of these three samples as function of temperature and excitation power. As described earlier, sample S5, shown again in Figure 6.5a, presents a strong S-shape behavior which becomes less pronounced at higher excitation power. Lowering the growth temperature to 460 °C resulted in a smaller S-shape behavior indicating a reduction in compositional fluctuations, as shown in Figure 6.5b for sample S6. This S-shape behavior almost fully disappeared when the temperature was further lowered to 420 °C, as shown in Figure 6.5c for sample S7. Indeed in this sample, the use of different excitation intensities did not change the PL peak energy which indicates that growth at this lower temperature suppressed the compositional fluctuations and hence minimized the carrier localization. Similar findings were reported in mixed As-Sb alloys (namely, InAlAsSb grown on InP) further indicating that lower growth temperatures seem to be favorable to diminish alloy fluctuations [101]. It should be noted however that

lowering the growth temperature resulted in a decrease of PL intensity. Samples S6 and S7 did not emit any luminescence for temperatures higher than 150 K. This decrease in PL intensity is believed to be the result of a higher density of defects associated with lower growth temperatures. We should also note that although all three samples S5, S6 and S7 have similar Sb compositions, the PL peak of sample S7 presents a slight blueshift of ~ 13 meV with regards to the PL of samples S5 and S6. The origin of this shift is not clear but it is suspected that this blueshift is a direct result of the homogenization of the Sb composition across the sample, similar to the findings that will be presented in this next section.

6.5. Effect of thermal annealing

The previous section revealed that lowering the growth temperature seems to reduce compositional inhomogeneities. In this section, we decided to investigate the effects of a thermal anneal treatment on the atomic distribution of Sb in our materials. Sample S5 was chosen for this study as it demonstrated the strongest S-shape behavior out of all the samples that were analyzed. The sample was sandwiched between two GaAs wafers and annealed at 800 °C for 5, 10 and 30 min under N_2 atmosphere. The resulting XRD spectra are shown below.

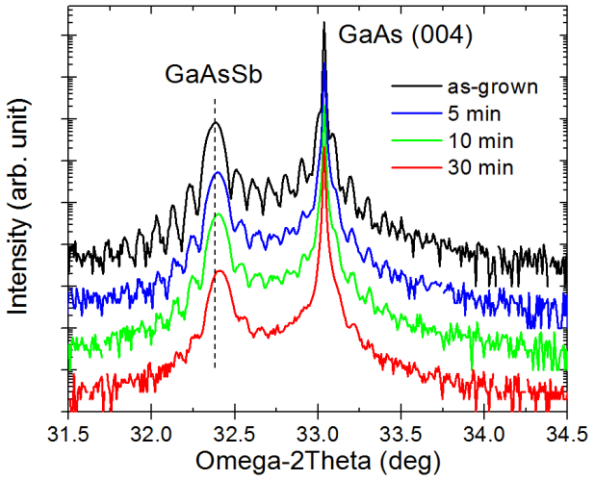

Figure 6.6. HRXRD ω-2θ scans of sample S5 as function of annealing time. The annealing temperature was 800°C.

As evidenced by Figure 6.6, we observed a gradual diminution of the Pendellösung fringes which totally disappeared after the 30 min anneal, indicating loss of coherency and hence crystal deterioration. A diminution in Sb composition was also observed from 12.2 % in the as-grown sample to 11.65 % after 30 min anneal. The fitted Sb composition for each annealing condition is summarized in Table 6.1.

Table 6.1. Change in Sb composition in GaAsSb after RTA at 800°C for different times.

RTA time (min)	Sb composition (%)
As-grown	12.20
5	11.90
10	11.85
30	11.65

Figure 6.7a shows that annealing also suppressed the S-shape behavior of the PL at low temperature, which also suggests that annealing leads to an homogenization of the Sb distribution. However, annealing was also found to induce a strong blueshift of the PL. Figure 6.7b shows a blueshift of 20.81 meV at 10 K. The amplitude of the blueshift is much higher than what would be expected from the change in Sb composition only. Indeed depending on what model is used to calculate the bandgap of GaAsSb, we would expect

an increase in bandgap of 6 – 8 meV maximum for a decrease of Sb composition from 12.2 to 11.65 % [105], [106], this indicates that the blueshift must originate from an additional mechanism which has not been identified yet but could simply be a result of an homogenization of the Sb composition.

As shown in Figure 6.7b, the PL intensity was also strongly impacted by annealing, *i.e.*, the longer the anneal the lower the PL intensity. On the other hand the FWHM was found to decrease by roughly 10 meV after annealing. It was initially believed that the decrease in PL intensity was a result of desorption of the GaAs cap layer, however TEM analysis did not confirm this hypothesis. Further investigation of these annealed samples will be necessary to understand the exact origin of the blueshift as well as the reduction in PL intensity.

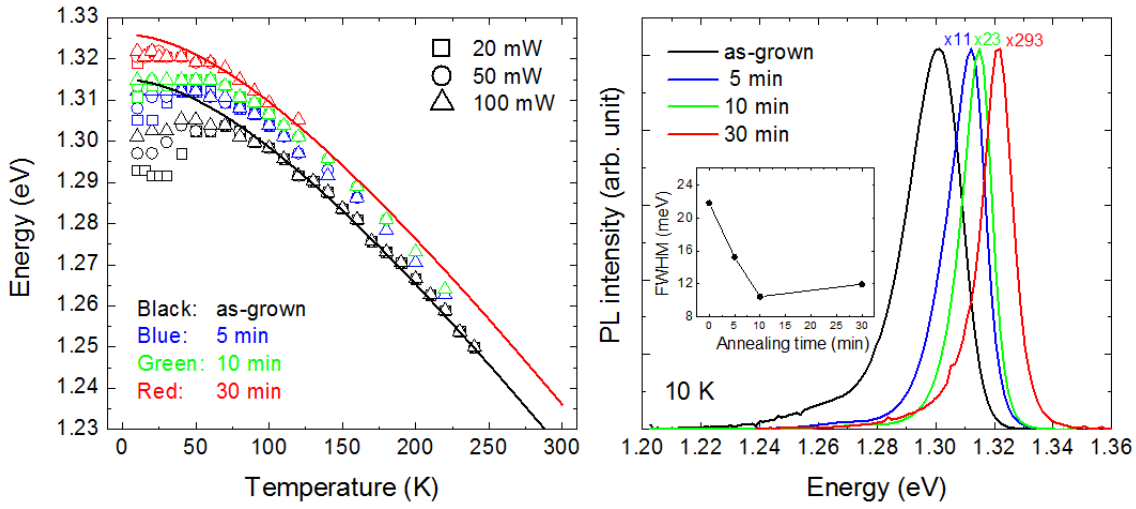

(a) (b)

Figure 6.7. a) PL peak energy of sample S5 (12.2 % Sb) as a function of temperature and excitation power. The anneal temperature was 800°C. The lines are the fitted values using Eq. (6.1), b) PL spectra at 10K for different annealing time. The inset shows the change in FWHM as a function of annealing time.

6.6. Summary

The optical properties and GaAsSb were investigated prior to introducing nitrogen. It was found that non-optimum growth conditions led to compositional fluctuations which

induced carrier localization effects at low temperature. These localized carriers induced an S-shape behavior of the PL peak energy at low temperatures. Lowering the growth temperature and post-growth rapid thermal annealing were both found to homogenize the Sb distribution and hence suppressed the S-shape behavior of the low temperature PL. However, a reduction in PL intensity was also observed in both cases.

CHAPTER 7

GROWTH OPTIMIZATION AND CHARACTERIZATION OF GaNAs(Sb)

The growth of GaNAsSb was first proposed in 1999 by Ungaro *et al.* for long wavelength applications [107]. Since then, only a few groups have studied this material system. In 2004, Yuen *et al.* looked at using GaNAsSb to replace GaNAs as the barrier layers in their GaInNAsSb quantum wells [108], [109]. For the growth parameters and desired end use in those studies, it was found that GaNAsSb quantum wells demonstrated poorer optical quality than GaInNAs(Sb) and thus their further work focused on GaNAs/GaInNAs(Sb) quantum wells only. Around the same time, Wicaksono *et al.* also investigated the growth of GaNAsSb for infrared detectors and long-wavelength lasers [110], [111]. Initial investigations of lattice-matched GaNAsSb for multijunction solar cell applications took place in 2009 – 2011 [112], [113]. Most of the work on GaNAsSb to date has focused on MBE grown materials, however Kim *et al.* have also investigated the growth of this material by MOVPE [31]. Between 2009 and 2015, GaNAsSb solar cells have been demonstrated both on GaAs and Si substrates [59], [112]–[114]. Their performance will be briefly reviewed and compared to what has been developed in the present study, described below.

This chapter will discuss the introduction of nitrogen into GaAsSb, the steps that were developed for growth of high quality, lattice-matched GaNAsSb films with bandgap close to 1 eV and characterization of the materials and device properties of the resulting GaNAsSb films.

7.1. Sample description

The GaNAs(Sb) samples investigated in this chapter were grown on semi-insulating (001) GaAs substrates. For consistency, all samples had 0.1 μm GaNAs(Sb) layers sandwiched between a 300 – 450 nm GaAs buffer layer and a 50 nm GaAs cap layer. The chart presented in Figure 7.1 shows the growth procedure step by step that was used in all the subsequent growths. The growths started with a 300 – 450 nm nm GaAs buffer layer grown at elevated temperature (600°C) to suppress any remaining surface imperfections. As the dilute nitrides need to be grown at much lower temperatures, the substrate temperature was ramped down at a rate of 30°C/min during the growth of this buffer layer. Once the substrate temperature reached the desired temperature, the nitrogen plasma was ignited with the N shutter kept close to minimize N incorporation in GaAs. To avoid any growth interruption, GaAs growth was maintained for a few minutes while the plasma was stabilizing. Once the plasma stabilized, the nitrogen shutter was opened and the 0.1 μm GaNAs layer was grown. When growing GaNAsSb, the Sb shutter was open a few seconds before the N shutter to establish residency of Sb on the surface. Following the growth of the dilute nitride layer, the N and Sb shutters were closed and the plasma was turned off. Simultaneously a 10 nm GaAs cap was grown at low temperature. Following this thin cap layer, the Ga shutter was closed and the temperature was ramped back up to 580°C (using a ramp rate of 20°C/min) to finish the growth of the remaining GaAs cap layer (an additional 40 nm). The following sections will describe the optimization of the plasma conditions, growth temperature, growth rate and finally thermal annealing that led to the growth of high quality lattice-matched materials.

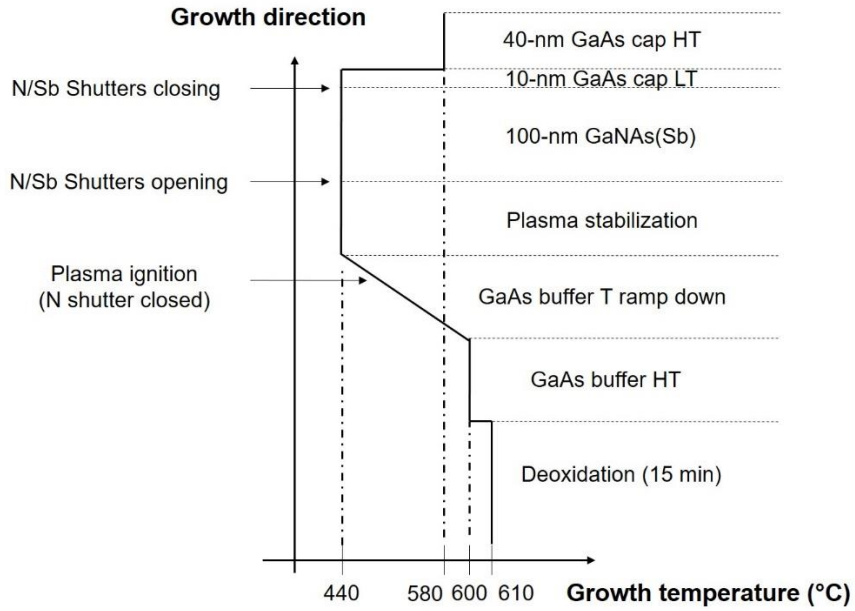

Figure 7.1. Schematic of typical growth procedure during optimization of GaNAs(Sb) growth.

7.2. 2D growth of GaNAs(Sb)

The growth of dilute nitrides relies on the incorporation of N atoms into Ga(In)As(Sb) materials. During the first few growths (early work focused on GaNAs only), we experienced a problem that has been widely reported by other dilute nitride growers: upon opening of the nitrogen shutter, the RHEED switched from a perfect and bright (2x4) pattern typical for the growth of GaAs to a (1x1) spotty pattern, as shown in Figure 7.2 [42], [115]. This drastic change in RHEED pattern indicated a change in the growth dynamic from a smooth 2D growth to a rough 3D growth. For the growth of high quality materials, smooth surfaces with a homogenous atomic distribution are required. After tuning of the nitrogen flux we found that we could maintain 2D growth as long as the pressure in the MBE chamber was kept below 5×10^{-6} Torr (corresponding to a N flux of roughly 0.25 sccm).

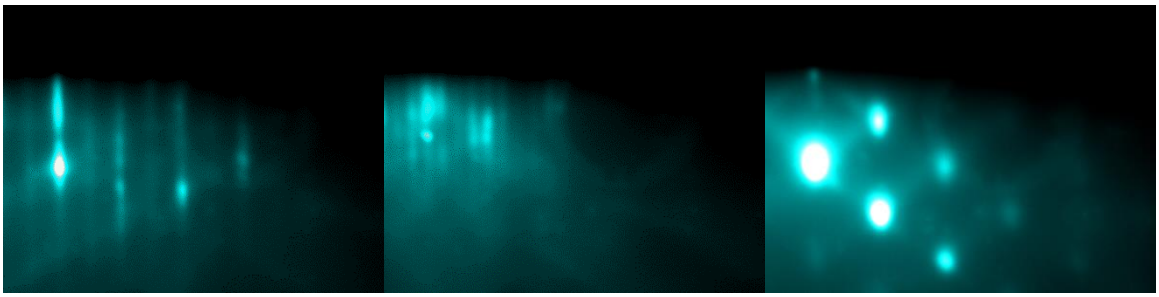

(a) (b) (c)

Figure 7.2. Typical RHEED pattern for high quality GaAs showing a) the streaky x2 and b) the streaky x4 pattern (b) while introduction of nitrogen initially led to a spotty (1x1) pattern as shown in c) [29].

7.3. Effect of varying growth parameters

After ensuring that 2D growth was maintained, the parameter space for growth of GaNAs and GaNAsSb was studied. This growth parameter study was performed step by step, starting with Sb-free materials in order to understand the nitrogen incorporation in GaAs.

7.3.1. Effect of nitrogen flow

In order to investigate the effect of the nitrogen flow on the nitrogen incorporation, a few samples were grown with different nitrogen flows that resulted in background pressure ranging from 1.8×10^{-6} to 3.6×10^{-6} Torr (extrapolating these values to N flows would correspond to flows of approximately 0.04 to 0.2 sccm). These flows were intentionally kept so that the background pressure in the chamber would stay below the 5×10^{-6} Torr limit to ensure smooth growth. The growth temperature was 440°C, the growth rate was 1 µm/hr while the As/Ga BEP ratio was 10. The XRD scans of the corresponding samples are shown in Figure 7.3a. The nitrogen composition was extracted both from XRD and SIMS. The composition from SIMS measurements depends on how well the N composition is known in the standard sample (a GaInNAs(Sb) standard sample was used in this case) while the composition from XRD was calculated using Vegard's law, which

altogether might lead to significant discrepancies between the two methods. As shown in Figure 7.3b, however, the compositions obtained from the two techniques agreed reasonably well. Using the SIMS data as a reference, it was found that the minimum N composition that can be achieved is 1.8 %. Using smaller N flows was found to lead to an extinguishing of the plasma which ultimately indicates that the smallest N composition that can be achieved in our material is 1.8 %. This is mainly due to the aperture plate currently installed on the plasma source (499 holes of 0.08" diameter) which delivers too much nitrogen.

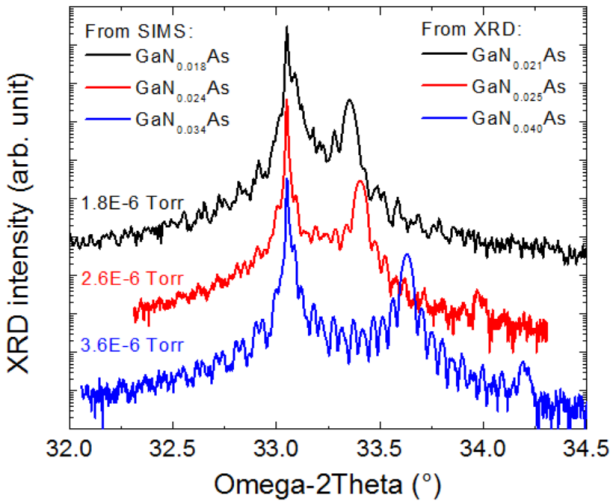

(a)

Background pressure (Torr)	N % from SIMS	N % from XRD
1.8E-6	1.8	2.11
2.6E-6	2.37	2.47
3.6E-6	3.42	2.99

(b)

Figure 7.3. a) Effect of changing the nitrogen flow on the nitrogen incorporation. The data shown on the left represent the corresponding background pressure in the chamber. b) N content obtained from both SIMS and XRD analysis.

7.3.2. Effect of growth rate and forward power

The N incorporation is known to be inversely proportional to the group-III growth rate [116]. This was verified by growing samples at different growth rates of 0.7 µm/hr and 1.0 µm/hr. In addition, the RF power was also varied to investigate its effect on the nitrogen incorporation. As shown in Figure 7.4, the N content increased as the RF power increased and the growth rate decreased. The minimum N composition that could be obtained was

1.60 % using a growth rate of 1.0 µm/hr and a RF power of 265 W. Using smaller RF powers led to plasma extinguishment. As a result, an RF power of 300 W was used in all subsequent growths with a growth rate set to 1.0 µm/hr.

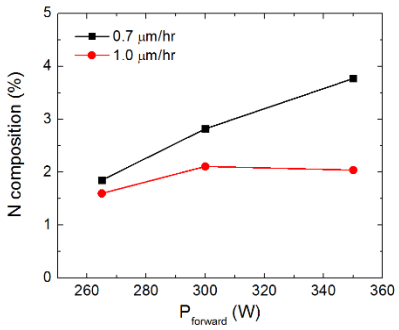

Figure 7.4. Variation in N composition as a function of the Ga growth rate and the forward power

7.3.3. Effect of growth temperature

Several GaNAs samples were grown at different growth temperatures between 420 and 500°C. The N background pressure was 1.8×10^{-6} Torr, the RF power was 300 W, the growth rate was 1.0 µm/hr and the As/Ga BEP ratio was 10. As shown in Figure 7.5a, the N composition was found not to change within the range of temperatures used in this work. Similar observations were reported in GaNAs and GaNAsSb films [108], [110], [117]. This has been explained by the fact that N adatoms have a near-unity sticking coefficient within this temperature range.

Similarly, a few GaNAsSb samples were grown at different growth temperatures under the same conditions. As shown in Figure 7.5b, the PL intensity decreased gradually as the growth temperature increased. Although the N composition does not seem to be influenced by the growth temperature, we found that Sb incorporation increased significantly as the growth temperature is lowered [29]. This might indicate that the decrease in PL intensity is related to increase in Sb composition. Nevertheless, a growth

temperature of 440°C was chosen as the optimum growth temperature as it resulted in the highest PL intensity.

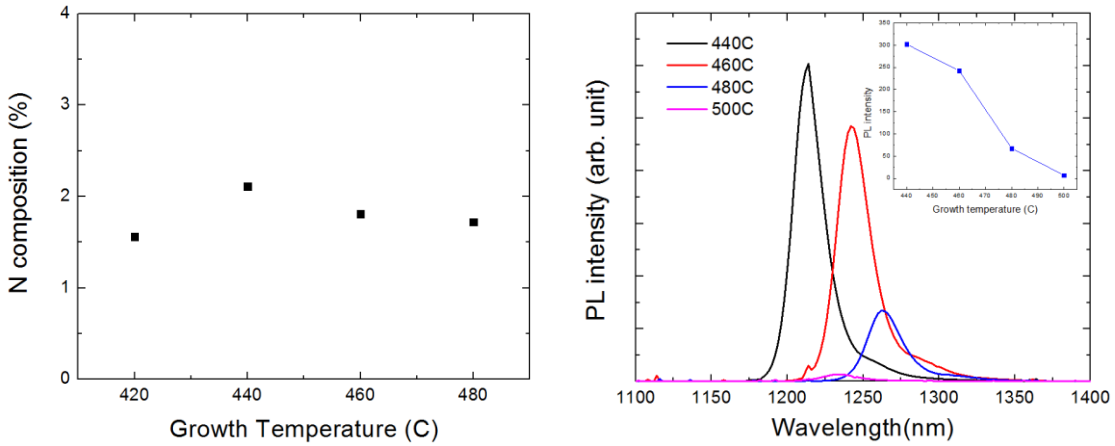

(a) (b)

Figure 7.5. a) Change in N composition for samples grown at different growth temperatures (obtained from XRD). b) Effect of growth temperature on the PL intensity of GaNAsSb films. The inset shows the corresponding decrease in PL intensity with increase in growth temperature.

7.4. Lattice-matched GaNAsSb

For the growth of high quality materials, lattice-matching is essential. As described in the previous chapters, one of the unique advantages of the dilute nitride materials system is that it can be grown lattice-matched to GaAs and Ge by carefully controlling the chemical compositions. The lattice parameter of GaInNAs and GaNAsSb were calculated using Vegard's law:

$$a_{Ga_{1-x}In_xN_yAs_{1-y}}=(1-x)(1-y)a_{GaAs}+y(1-x)a_{GaN}+x(1-y)a_{InAs}+xya_{InN} \quad (7.1)$$

$$a_{GaN_yAs_{1-x-y}Sb_x}=(1-x-y)a_{GaAs}+xa_{GaSb}+ya_{GaN} \quad (7.2)$$

By substituting x and y in both equations, it is found that GaNAsSb and GaInNAs can be lattice-matched to GaAs as long as the ratios of Sb/N and In/N are kept close to 2.6 and 2.8 respectively.

In order to identify the growth conditions that resulted in the appropriate Sb and N compositions, 100-nm thick GaNAsSb films were grown with varying the Sb flux while all the other growth parameters were kept constant. The growth temperature was 440°C while the growth rate was 1 µm/hr and the As/Ga ratio was kept close to 10. Note that the plasma conditions were also kept constant in all the consequent growths with a nitrogen flux of 0.1 sccm and a forward power of 300 W. All the samples were capped with a 50-nm GaAs layer.

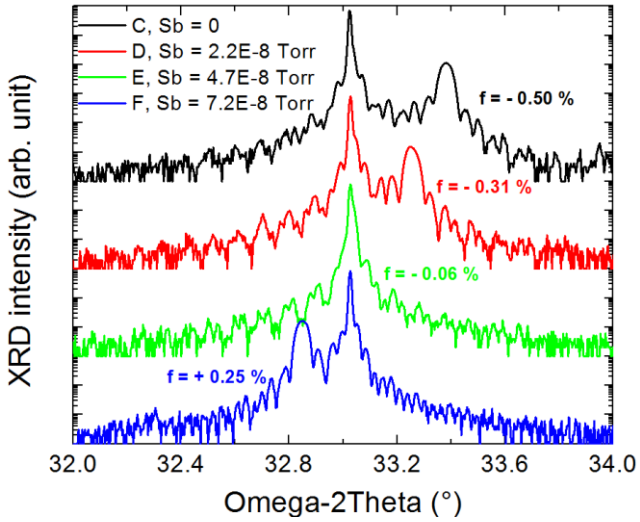

(a)

Sb flux (Torr)	N %	Sb %	Mismatch (%)
0	2.4	0	- 0.50
2.2E-8	2.4	3.4	- 0.31
4.7E-8	2.4	7.1	- 0.06
7.2E-8	2.8	10.8	+ 0.25

(b)

Figure 7.6. a) XRD ω-2θ scans of GaNAs(Sb) samples grown with different Sb fluxes, b) N and Sb compositions obtained from SIMS and corresponding lattice mismatch obtained from XRD [118].

Figure 7.6a shows that the GaNAs film grown without Sb was tensile strained with a N composition of 2.4 %. Introducing an increasing amount of Sb resulted in a shift of the GaNAsSb epilayer towards the compressive side of the GaAs (004) peak. The corresponding lattice mismatch obtained from XRD is presented in Figure 7.6b. The Sb and N compositions were extracted from SIMS measurements as there were too many variables to accurately fit the XRD curves. As shown in Figure 7.6, the sample grown with a Sb flux of 4.7E-8 Torr appeared to be lattice-matched to GaAs with a N and Sb

compositions of 2.4 and 7.1 % respectively. This corresponds to Sb/N ~ 2.96 which is much higher than the predicted ratio of 2.6. As discussed by Wicaksono et al., SIMS accounts for both substitutional and interstitial Sb and N atoms while what is measured by XRD only accounts for substitutional atoms [110]. This might explain the large difference between the predicted and the measured Sb/N ratio.

Nevertheless, these films were rather thin (100-nm thick). In order to confirm that the growth of thick layers remained coherent during the growth of a thicker layer, a 1-µm thick $GaN_{0.024}AsSb_{0.071}$ film was grown under the same growth conditions and compared to a similar 1-µm thick $GaAsSb_{0.09}$ sample grown without nitrogen. The (224) RSM of the $GaAsSb_{0.09}$ sample shown in Figure 7.7a revealed that there was a large difference in both the in-plane ΔQ_x and out-of-plane ΔQ_y mismatch and hence, this induced a GaAsSb film that was about 80 % relaxed. The GaNAsSb film on the other did not present any discernable difference either in the in-plane or out-of-plane mismatch indicating that the film was grown coherently on GaAs and that perfect lattice-matching was maintained, as shown in Figure 7.7b.

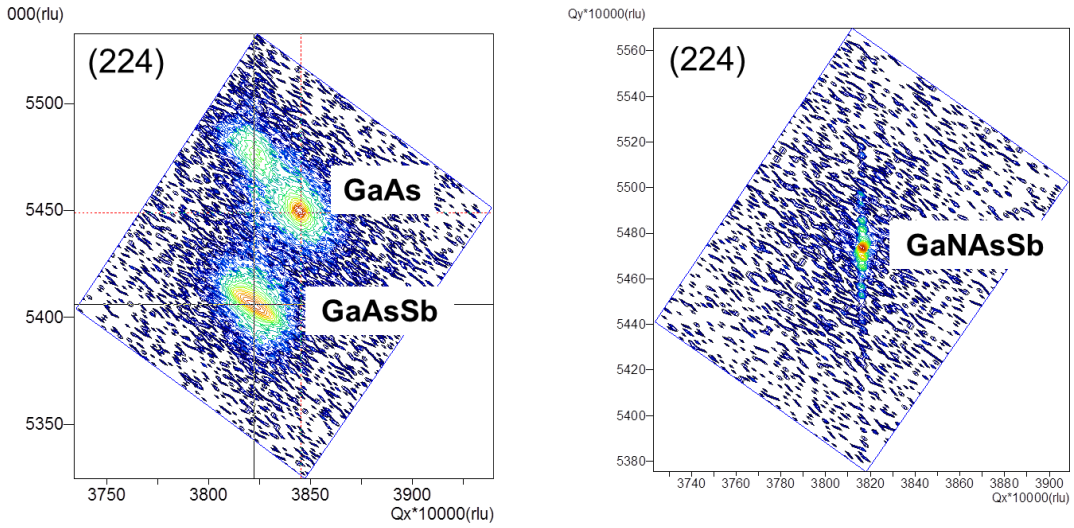

(a) (b)

Figure 7.7. Asymmetrical (224) reciprocal space maps of a 1-µm $GaAsSb_{0.09}$ and a 1-µm $GaN_{0.024}AsSb_{0.071}$ film. The GaAsSb film was 80% relaxed while the GaNAsSb film was lattice-matched to GaAs.

7.5. Group-V incorporation

The incorporation process of group V elements has been studied by several groups however it appears that not all found common ground. For instance, Harmand *et al.*, Yuen *et al.* and Wicaksono *et al.* all found that N incorporation was enhanced in the presence of Sb [108], [111], [119]. On the contrary, Ma *et al.* did not observe any change in N composition in GaNAs or GaNAsSb for the same growth conditions [117]. Furthermore, Yuen *et al.* found that increasing the As overpressure and the growth temperature did not affect the N incorporation but both led to a decrease in reduction of the Sb incorporation [108]. Both Wicaksono *et al.* and Ma *et al.* found that Sb and N compete for the group V sites and that incorporation of N suppresses the Sb incorporation [111], [117].

In order to get a better understanding of the incorporation mechanism of Sb and N in our materials, two sets of samples were investigated in this work. In the first set, the N flux was fixed at 2.6×10^{-6} Torr while the Sb flux was increased from 0 to 7.2×10^{-8} Torr.

In the second set, the Sb flux was fixed at 4.7 × 10^{-8} Torr while the N flux was increased from 1.8 to 3.6 × 10^{-6} Torr. All the samples were grown at 440°C with a growth rate of 1 µm/hr and with an As/Ga ratio of 11.

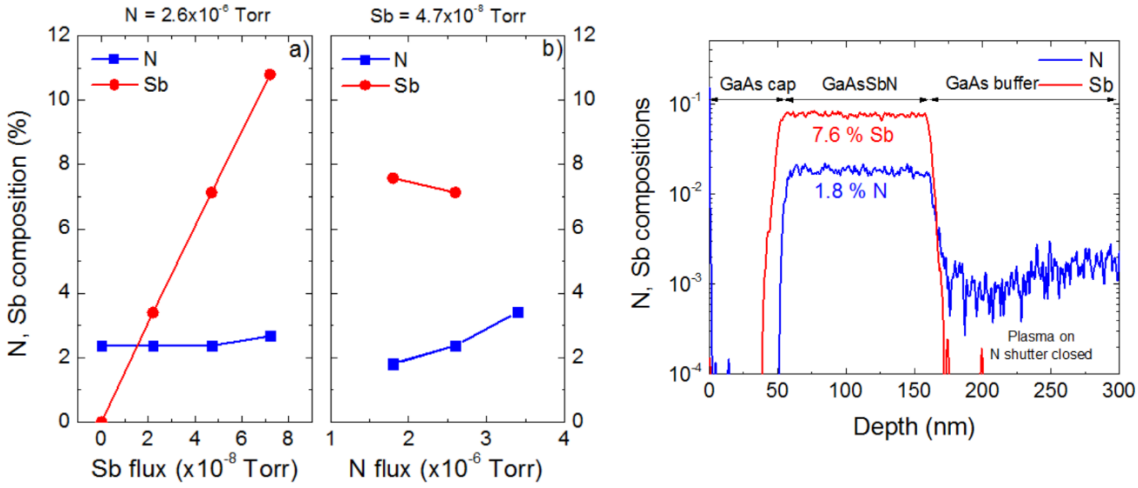

(a) (b)

Figure 7.8. a) N and Sb incorporation as a function of Sb and N fluxes, b) SIMS depth profile of a 100-nm GaNAsSb film. [29], [118]

SIMS analysis was used to extract the N and Sb composition in these samples. As shown in Figure 7.8a, increase in the Sb flux led to a linear increase of the Sb composition while the N composition was found almost unchanged. These findings are in very good agreement with work from Ma *et al.* [117] but disagree with all other reports that showed that N incorporation increased in the presence of Sb [108], [111], [119]. Figure 7.8b shows that increasing the N flux led to an increase in N composition but decrease in Sb incorporation, also in agreement with Ma *et al.* [117]. This definitely indicates some type of competition between N and Sb to occupy the group V sublattice sites. Although N atoms are much smaller than Sb atoms, the sticking coefficient of N is higher than that of Sb and hence increasing the amount of N atoms will tend to favor N incorporation while suppressing that of Sb.

Finally a SIMS depth profile is shown in Figure 7.8c for a 100-nm thick $GaN_{0.018}AsSb_{0.076}$ sample. Two distinct features were observed from this depth profile: i) although the N shutter is kept close during the plasma stabilization (as explained in Section 0), up to 0.1% N was found to incorporate in the GaAs buffer layer and ii) the N and Sb profiles do not end at the same depth even though both the Sb and N shutters were closed at the same time. This was found in all the other samples measured by SIMS and was also reported by other groups [108]. Sb has been shown to act as a surfactant and hence it is believed that Sb floats on the growth surface even after the Sb shutter is closed, leading to Sb incorporation until all the Sb atoms have been incorporated or desorbed from the front growth.

7.6. Effect of substrate rotation speed

During epitaxial growth, the substrate is usually rotated to ensure good uniformity across the wafer. During the initial steps of this project, the rotation speed used throughout the growth of these dilute nitride layers was set to 2 revolution per minute (RPM). The reason for this very slow rotation speed was that, as stated in section 0, monitoring the RHEED reconstruction pattern was very important in ensuring that 2D growth was maintained. Although this slow rotation speed allowed us to carefully monitor the surface reconstruction, it also had an unexpected effect that became clearly noticeable when the growth of thicker films was initiated.

Indeed, as shown for instance in Figure 7.9a, two films were grown under the same growth conditions with the only difference being that the thickness of the GaNAsSb layers was increased from 0.1 to 1.0 µm. The Sb and N fluxes were chosen so that the resulting films would be lattice-matched to the GaAs substrate. The substrate rotation speed used

during the growth of these two films was set to 2 RPM. Whereas the XRD analysis of the thin (0.1 µm) sample did not reveal any abnormal characteristics, the XRD profile of the thick (1.0 µm) structure revealed an unintentional superordering in the GaNAsSb layer with a period of ~ 4.5 nm of Sb-rich and ~ 4.5 nm of Sb-poor layers, as calculated by fitting the XRD profile.

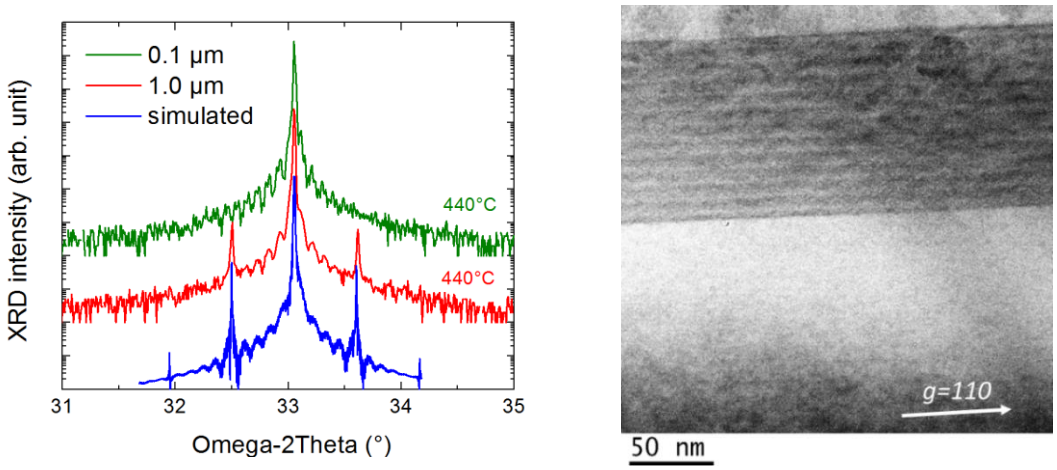

(a) (b)

Figure 7.9. a) HRXRD ω-2θ scans of two GaNAsSb films grown with different thicknesses. The bottom line corresponds to the fitted profile of the 1-µm thick sample; b) TEM image of the 0.1 µm-thick sample shown in a) revealing the presence of an unintentional superlattice.

Since these two samples were grown one after the other using the same growth conditions, it was rather surprising that both did not present this superlattice ordering behavior. In order to confirm the XRD results, TEM images were collected on the 0.1-µm thick sample. As shown by the 2-beam diffraction contrast image in Figure 7.9b, also not seen in the XRD measurement, TEM confirmed the presence of an unintentional superlattice ordering with a total thickness of ~ 107 nm, with 12 repeated periods of bright and dark layer respectively, plus one extra dark layer. Each period of this SL was ~ 8.5 nm thick and contains one bright and one dark layer. Note that, although not visible on the

XRD of the thin film, the period thickness of the superlattice peaks measured by TEM is in good agreement with the XRD fit of the thicker structure.

The reason for the formation of this unintentionally superordered structure was found to be the result of a combination of slow substrate rotation speed and high growth rate. Indeed, the samples were grown with a growth rate of 1 ML/s (1 μm/hr) while the substrate was rotated at 2 RPM. This corresponds to:

$$1\ [\text{ML/s}] \times 60\ [\text{sec}] = 60\ \text{ML/min}$$

$$60\ [\text{ML/min}] / 2\ [\text{r.p.m.}] = 30\ \text{ML / rotation}$$

Considering that a monolayer (ML) is 0.28 nm thick, this indicates that the thickness of each layer grown per rotation is:

$$0.28\ [\text{nm}] \times 30\ [\text{ML}] = 8.4\ \text{nm}$$

This value is in very good agreement with the measured superlattice period thickness from XRD and TEM.

In order to ensure that we could suppress this unintentional superlattice behavior and grow thick, bulk materials, additional samples were grown with higher rotation speed. As shown in Figure 7.10, increasing the rotation speed to 20 RPM was enough to avoid the formation of these superlattices. Note that the sample growth at 20 RPM presented a slight tensile strain which resulted from a slight change in Sb and/or N fluxes used during growth.

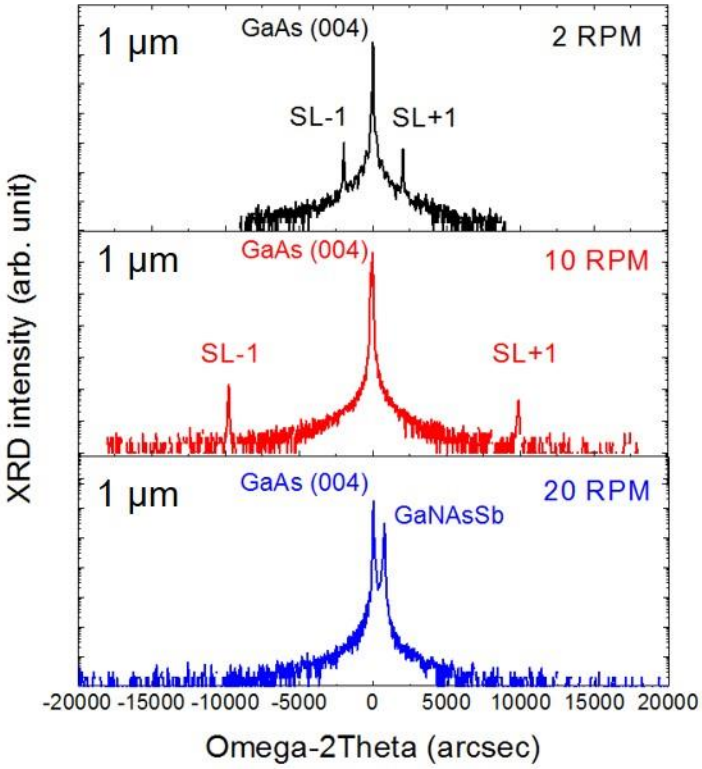

Figure 7.10. Effect of increasing the substrate rotation speed on the formation of unintentional superlattice. All three samples were 1-µm thick GaNAsSb samples grown with nominally the same Sb and N fluxes.

Following these findings, the substrate rotation speed was maintained at 20 RPM during the growth of our dilute nitride material to ensure the growth of bulk materials.

7.7. Effect of thermal annealing

One of the undesirable properties of the dilute nitrides is that they are known to be very defective which often results in short minority carrier diffusion length (*i.e.*, low mobility and low minority carrier lifetime) [55]. Additionally, unintentionally high background doping concentrations have been reported in these materials [55]. High background doping is associated with a narrow depletion width which in turn results in a low carrier collection collection [34], [120]. Defects originate mainly from the low temperature used during growth and the use of the N plasma which introduces N-related recombination centers [113]. The incorporation of N has also been shown to increase the

background doping [33]. Thermal annealing has proven to be very effective at improving the recombination properties of these dilute nitride materials by reducing the amount of defects in the material. Large increases in PL intensity have been observed in both GaInNAs(Sb) and GaNAsSb materials after thermal treatment due to a reduction in the density of recombination centers [121], [122]. A blueshift of the PL is also usually observed in both GaInNAs and GaNAsSb [122], [123]. In GaInNAs, this blueshift originates from a rearrangement of the local bonding environment. The N-nearest neighbor environment is believed to switch from Ga-rich to In-rich upon annealing to reduce the local strain [123]. In GaNAsSb there is no In atoms, therefore Ga-In atomic rearrangement cannot explain this blueshift. Lin et al. reported that the origin of the blueshift in their GaNAsSb was a dissociation of N-N pairs into single N_{As} substitutional atoms [124].

Our as-grown materials only demonstrated PL at low temperature therefore it was also necessary for us to investigate the effect of thermal annealing on the optical characteristics of our materials. The annealing study was performed using rapid thermal annealing (RTA). To identify the optimum annealing conditions, we usually annealed 100-nm thick GaNAsSb samples with various N and Sb compositions at different temperatures and different times in N_2 ambient. In all the annealing experiments, the samples were sandwiched in between two GaAs wafers in order to protect the surface and avoid any As out diffusion at elevated temperature.

Figure 7.11 presents the results of a typical RTA experiment. In this case, a $GaN_{0.018}AsSb_{0.076}$ sample was first annealed for 1 min at different temperatures. Once the optimum temperature was found, based on the maximum PL intensity and minimum full-width-at-half (FWHM), the sample was then annealed at that temperature for different

times. The PL intensity was found to be maximum after a 5 min anneal at 750°C. The post-RTA PL intensity increased drastically with an improvement factor of 26× whereas the FWHM was found to decrease dramatically from 55 to 19 meV, indicating a strong reduction in defect density. The optimum annealing conditions are most likely dependent on both the Sb and N compositions. Based on our experience the optimum annealing conditions for our material remain between 750 – 800°C for 5 – 10 min.

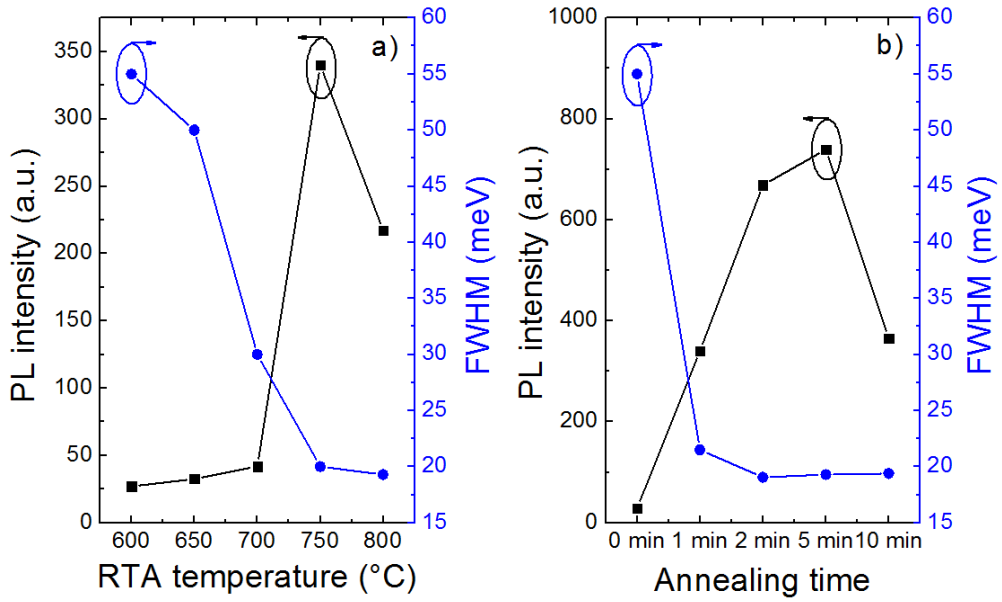

Figure 7.11. Effect of rapid thermal annealing on the PL intensity of a 100-nm thick GaN0.018AsSb0.076 sample.

RTA was performed at 750°C for 5 min under N_2 ambient on the four samples presented in Figure 7.6 and the resulting PL was measured and compared to the as-grwon samples. The corresponding low-temperature PL shown in Figure 7.12 demonstrated a large increase in PL intensity owed to a reduction in defect density (note that the PL intensity is represented in a log scale) however all the samples also demonstrated a significant blueshift of ~ 60 meV. As described earlier in this section, the origin of the blueshift in GaNAsSb is believed to be the result of a short range compositional

homogenization as well as a dissociation of N-N pairs into isolated substitutional N_{As} [124]. From our annealing experiment on GaAsSb presented in CHAPTER 6, it was also shown that Sb out-diffuses upon annealing. It is very likely that this also happens in the GaNAsSb system and might very well contribute to the observed blueshift.

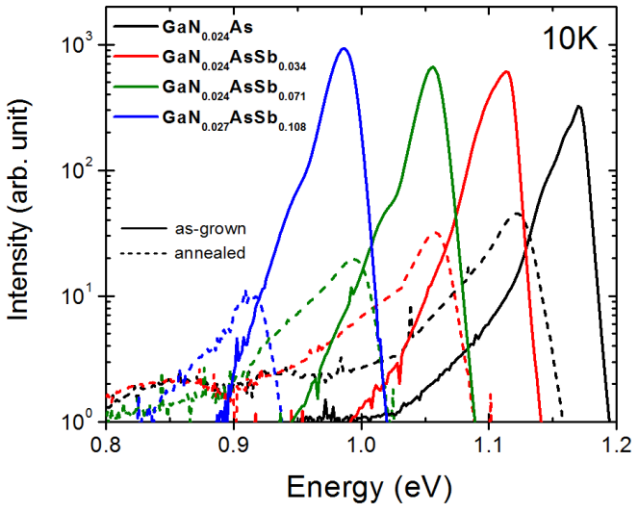

Figure 7.12. Low-temperature PL (10 K) spectra of four GaNAsSb grown with different Sb fluxes before and after RTA at 750°C for 5 min under N2 ambient.

7.8. Bandgap of GaNAsSb

In this work, we assume that the room temperature PL energy corresponds to the bandgap. As shown in the previous section, most of our as-grown materials demonstrated very poor PL efficiency therefore it was necessary to investigate their optical emission at low temperature. Once annealed, however, most of our samples demonstrated room temperature PL. Figure 7.13 presents a series of temperature-dependent PL measurements of several GaNAsSb samples. Although these samples were annealed, this did not appear to be sufficient in order to fully homogenize the atomic composition, as a clear S-shape behavior is observed in all samples. This suggests the presence of carrier localization, similar to what has been reported earlier in CHAPTER 6 for GaAsSb and also suggests that annealing conditions might need to be optimized further.

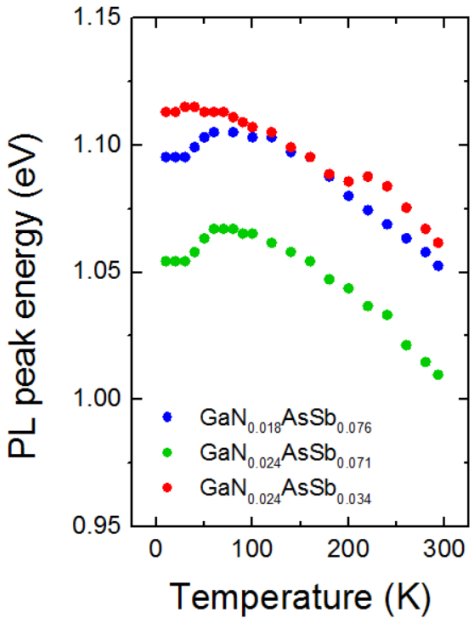

Figure 7.13. Temperature-temperature PL of different GaNAsSb samples annealed at 750°C for 5 min.

Photoreflectance (PR) spectroscopy was used to measure the optical transitions of our as-grown samples at room temperature. Since PR only modulate the change in reflectance of the materials, it is possible to obtain quite strong PR signals even in highly defective materials. Figure 7.14 presents typical room temperature PR spectra for Ga(N)As(Sb) with various amounts of Sb and N.

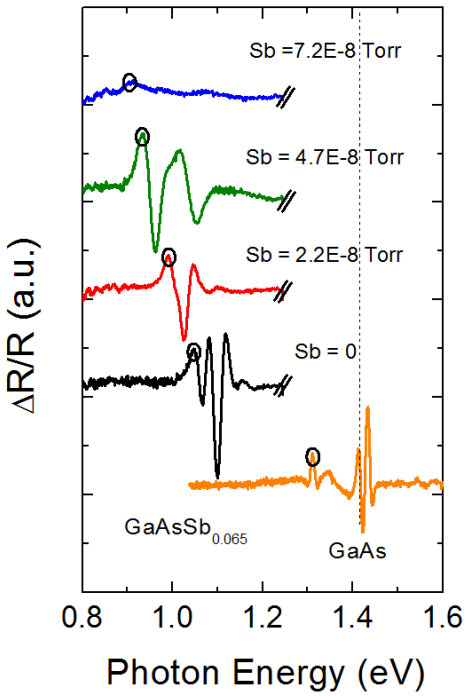

Figure 7.14. Room-temperature PR spectra of different as-grown Ga(N)As(Sb) samples.

III-V alloys demonstrate an unusually large bandgap reduction when small fractions of N are introduced. This behavior has been explained by the band anticrossing (BAC) model [125]. In the case of GaNAsSb, the addition of Sb leads to a restructuring of the valence band described by the valence band anticrossing model (VBAC). On the other hand, the addition of N leads to a restructuring of the conduction band described by the conduction band anticrossing model (CBAC). To calculate the bandgap reduction of GaNAsSb as a function of both Sb and N, a combination of both models, i.e., a double band anticrossing model (DBAC), is therefore necessary [126].

According to the band anticrossing model, the bandgap can be calculated using the following equation:

$$E_{\pm}(k) = \frac{1}{2}\left\{[E_M(k)+E_N] \pm \sqrt{(E_M(k)+E_N)^2+4V^2.x}\right\} \qquad (7.3)$$

where E_M is the bandgap of the host material, E_N is the energy of the localized states derived from the substitutional N atom and V is an adjustable matrix parameter that describes the coupling between the localized states and the band states of the host [125].

Using this expression, we can plot the measured PR and PL data for different N and Sb compositions and compare the results to the BAC model. Although the number of measured samples is not representative of the number of samples investigated in this work, Figure 7.15 shows that a good agreement between the predicted and the measured bandgap was found. Note especially that the PL data points are blueshifted with regards to the PR data points and provide a better agreement with the BAC calculations.

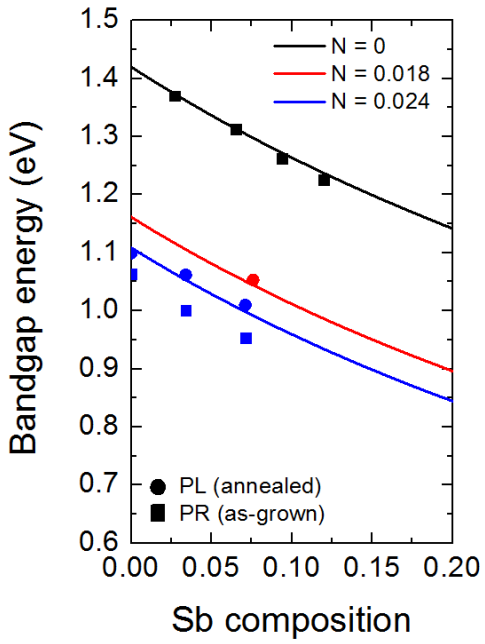

Figure 7.15. Comparison between measured (data points) and calculated bandgap (lines) using the band anticrossing model of Eq. (7.3). The square data points were measured by PR on as-grown samples while circle data points were measured by PL after thermal annealing.

7.9. Summary

In this chapter, the growth optimization of GaNAsSb was reviewed. In particular, the optimum growth parameters were found to synthesize high quality, lattice-matched GaNAsSb films. In particular, we demonstrated the growth of 1-eV material lattice-matched to GaAs. The N and Sb compositions that were found to result in lattice-matched growth were 2.4 % and 7.1 % respectively, corresponding to a Sb/N ratio of 2.95. The Sb and N incorporation mechanism were found to compete with each other for the group-V lattice sites. The use of slow substrate rotation speed in conjunction with high group-III growth rate was found to result in a superlattice ordering. Increasing the substrate rotation speed to 20 RPM was found to avoid this phenomenon. Rapid thermal annealing conditions were optimized and showed to improve drastically the optical characteristics of our materials. Further optical investigation revealed that we were able to produce materials with bandgaps near 1-eV, ideal for the growth of high performance solar cells.

CHAPTER 8

GaNAsSb SOLAR CELLS

8.1. Structure design

Two parameters have restrained the design of our structures: the high p-type background doping of our materials (as will be discussed in a later section) and the difficulty in doping it n-type. In particular we have yet to demonstrate the ability to compensate the high p-type doping to get n-type materials. This has limited us to using our GaNAsSb material as the p-type layer in our designs so far. Moreover, we have not been able to measure the minority carrier lifetime in these materials. Hence, we have investigated both n-p and n-i-p designs in order to study the variation in the cell performance. Taking into consideration these limiting parameters, two cell configurations have been investigated:

Structure A (G16-066) was an n-i-p structure that consisted of a 0.3-μm GaAs:Be buffer layer (5×10^{18} cm^{-3}), a 1.0-μm GaAs:Be base (5×10^{16} cm^{-3}), a 1.0-μm unintentionally doped (UID) GaNAsSb layer, a 0.2-μm GaAs:Si emitter (2×10^{18} cm^{-3}) and a 0.03-μm $Al_{0.8}Ga_{0.2}As$ window layer (1×10^{18} cm^{-3}).

Structure B (G16-074) was an n-i-p multi-quantum well (MQW) design identical to that of Structure A except that 25 periods of unintentionally doped (20-nm GaAs)/(20 nm GaNAsSb) MQW were inserted within the i-region instead of the 1.0-μm bulk GaNAsSb:UID.

Structure C (G16-068) was an n-p heterostructure that consisted of a 0.45-μm GaAs:Be buffer layer (5×10^{18} cm^{-3}), a 1.0-μm Be doped GaNAsSb base (1×10^{17} cm^{-3}), a

0.2-µm GaAs:Si emitter (2×10^{18} cm^{-3}) and a 0.03-µm $Al_{0.8}Ga_{0.2}As$ window layer (1×10^{18} cm^{-3}).

Details of the three structures are shown in Figure 8.1. AlGaAs was used both as the window layer and the BSF mainly because of limitations with the MBE tool at the time. As will be discussed later, GaInP would have probably been a better choice, but the motor operating the valve controller on the phosphorus cracker failed thus preventing us from accurate control of the P flux. Nevertheless, growth of lattice-matched $Ga_{0.50}In_{0.50}P$/GaAs heterostructures was demonstrated and will be implemented into actual devices. This represents an area of future work.

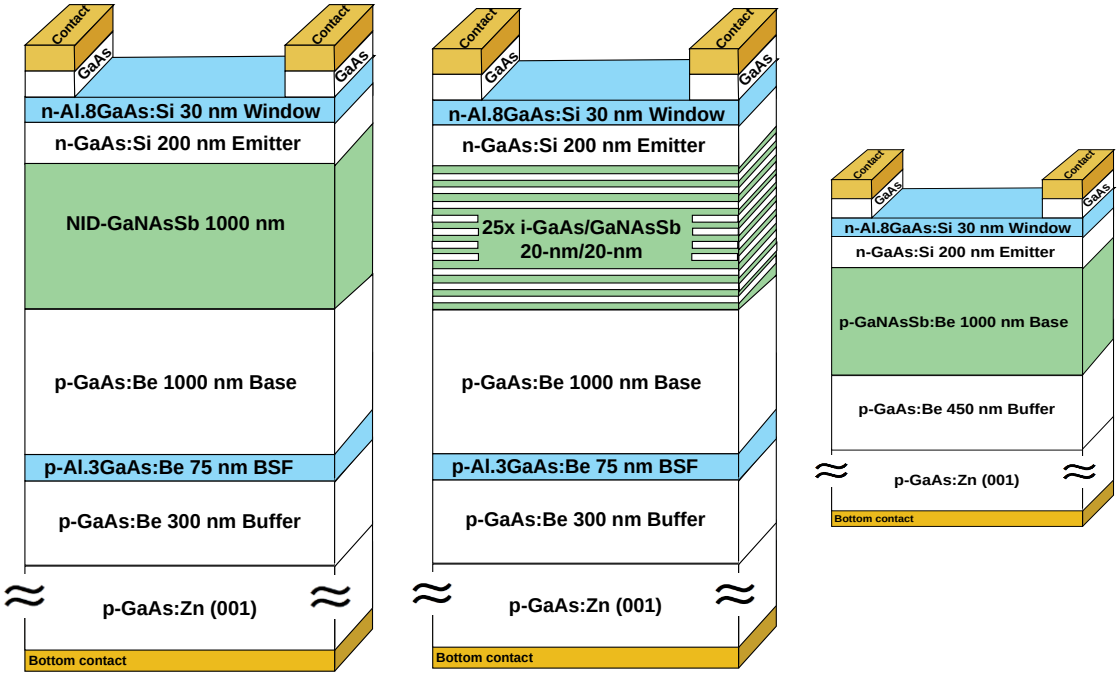

Figure 8.1. Structure design of the three solar cell configurations investigated in this work.

All the GaNAsSb layers were grown under conditions previously described in CHAPTER 7 and unless otherwise specified, all the devices underwent post-growth RTA at 800°C for 10 min under N_2 ambient prior to being processed into working devices. High-resolution XRD was used to verify that all structures were grown lattice-matched.

8.2. Cell results

8.2.1. Bulk devices (Structures A and C)

The so-called "bulk" structures A and C were investigated first. Note that the structures were measured without antireflective coating layers. As shown in Figure 8.2a, both structures demonstrated almost identical EQE with a bandgap close to 0.96 eV. The EQE reached a maximum of 43 %. In order to figure out the amount of power lost due to front surface reflection, the reflectance was measured. From there, a maximum IQE of 58 % was determined (shown in Figure 8.2a). The reflectance is expected to decrease upon deposition of an ARC. This will be discussed in Section 8.5.

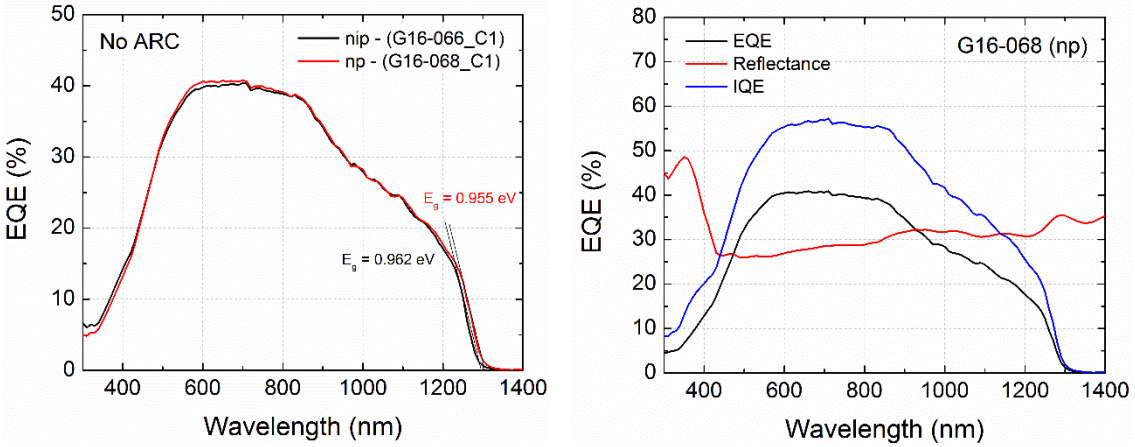

Figure 8.2. a) EQE of Structures A (n-i-p) and C (n-p), b) Reflectance and corresponding IQE for structure C (G16-068).

The IV characteristics of these cells were measured both under dark conditions and under 1-sun illumination, and revealed that both structures present the same characteristics. Structure A (n-i-p) demonstrated a J_{sc} of 15.67 mA/cm^2, similar than structure C (n- p) which had a J_{sc} of 15.49 mA/cm^2. The V_{oc} of both cells was 0.39 V, which corresponds to

a bandgap-voltage offset (W_{oc}) of 0.57 V. Finally the fill factor (FF) was 66 % in both structures. These parameters are summarized in Table 8.1.

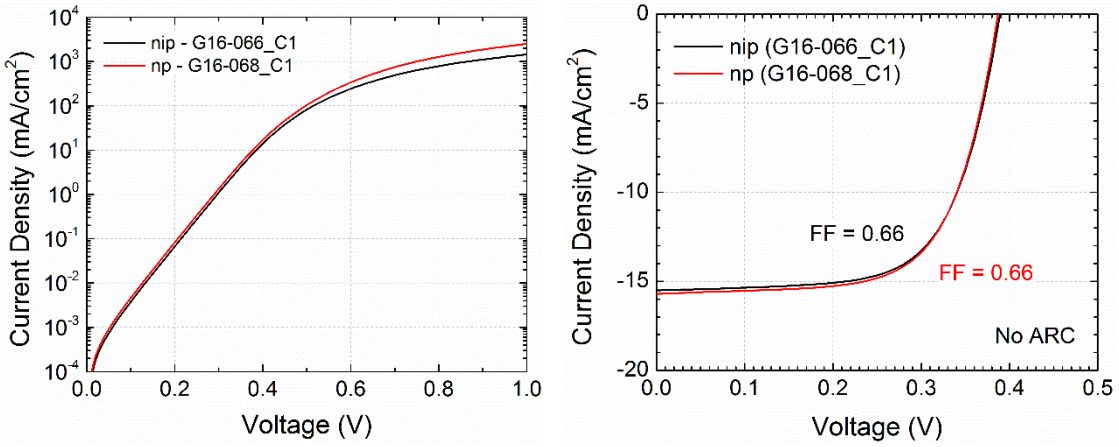

(a) (b)

Figure 8.3. IV characteristics of Structures A (n-i-p) and B (n-p) a) under dark conditions and b) under 1-sun illumination.

Table 8.1. Solar cell parameters obtained from 1-sun IV measurements for structures A, B and C. No ARC was applied.

	E_g (eV)	J_{sc} (mA/cm^2)	V_{oc} (V)	W_{oc} (V)	FF	η (%)
Structure A (n-i-p)	0.96	15.67	0.39	0.57	0.66	4.04
Structure B (MQW)	-	10.27	0.40	-	0.58	2.38
Structure C (n-p)	0.96	15.49	0.39	0.57	0.66	3.99

For multijunction solar cells applications, what matters is the current density that the cells would generate below a GaAs solar cell. For a 4J device, each subcell should generate between 12 -14 mA/cm^2. Integrating the EQE between 0.96 and 1.42 eV leads to a J_{sc} of 4.1 mA/cm^2, about a third of the needed value to be integrated in a multijunction device. This will be addressed in the next chapter.

8.2.2. Multi-quantum well devices (Structure B)

The addition of multi-quantum wells (MQWs) within the i-region of a n-i-p solar cell has been proposed as a way of improving the performance of GaAs solar cells [127]. The use of lattice-mismatched materials such as GaInAs limits the thickness and number

of QWs that can be incorporated in between the GaAs barrier layers and in most cases, a strain balancing layer is necessary to enhance the cell performance [128]. The use of GaNAsSb/GaAs QWs provides the advantage that this material is lattice-matched to GaAs while its bandgap is much smaller than that of GaAs.

The MQW solar cells (G16-074, structure B) were measured and compared to their n-i-p homologue bulk devices (structure A). It should be noted that samples from structure B were annealed at 800°C for 5 min, slightly less than the 10 min used in structures A and C. As presented in Figure 8.4a, although performing slightly better in the blue region the MQW devices demonstrated an overall much lower EQE than the bulk structures. This led to a much lower J_{sc} of 10.27 mA/cm^2. A V_{oc} of 0.4 V was measured and the FF decreased from 67 to 58 %. These values are also summarized in Table 8.1. Since the EQE did not allow accurate extraction of the bandgap, no W_{oc} value is reported.

Table 8.1. Solar cell parameters obtained from 1-sun IV measurements for structures A, B and C. No ARC was applied.

	E_g (eV)	J_{sc} (mA/cm^2)	V_{oc} (V)	W_{oc} (V)	FF	η (%)
Structure A (n-i-p)	0.96	15.67	0.39	0.57	0.66	4.04
Structure B (MQW)	-	10.27	0.40	-	0.58	2.38
Structure C (n-p)	0.96	15.49	0.39	0.57	0.66	3.99

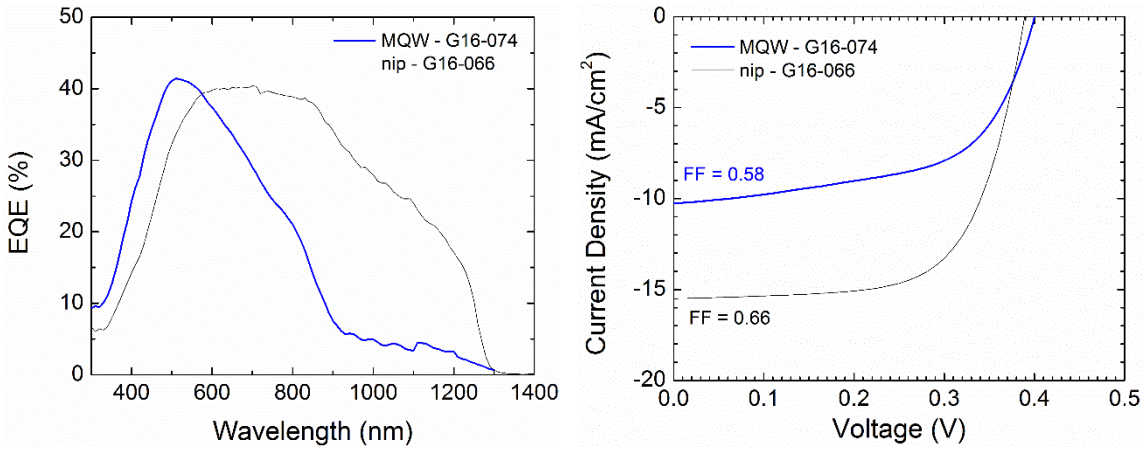

(a) (b)

Figure 8.4. Comparison of the a) EQE and b) 1-sun IV of the MQW solar cell (structure B) and the n-i-p structure (structure A).

It has been previously established from SIMS analysis in Section 7.5. that Sb floats on the surface and continue to incorporate in GaAs even when the Sb is closed until the supply of Sb is completely exhausted. If Sb keeps incorporating in the material while it was not supposed to, it implies that the QW interfaces are not well defined. This will have a direct impact on carrier confinement and hence, carrier collection, which is believed to be the main reason leading to the poor EQE in these solar cells. In order to quantify how much this could affect the QW interfaces, a SIMS depth profile was performed on a 20-nm single-quantum well (SQW) GaNAsSb/GaAs sample. As shown in Figure 8.5, the SQW thickness was measured to be 20 nm while Sb was found to incorporate for another 10 nm. Assuming similar incorporation occurred in our MQW solar cells, this would result in MQW of 20-nm GaNAsSb/10-nm GaAsSb/10-nm GaAs, far from the 20-nm GaNAsSb/20-nm GaAs originally designed.

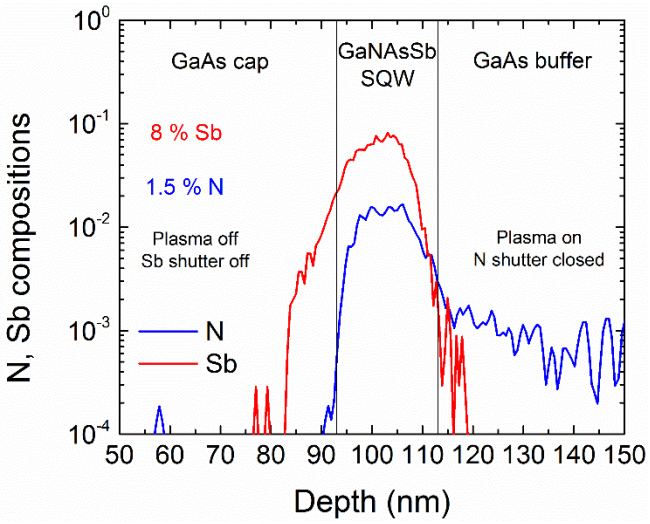

Figure 8.5. SIMS profile of a 100-nm SQW GaNAsSb. The Sb compositions is found to extend 10 nm after the Sb shutter was closed.

A solution to this problem would be to close the Sb shutter a few seconds before the N shutter. This has not been investigated in this dissertation thus most of the following work has focused on bulk structures. This could represent an area of future work.

8.3. Effect of thermal annealing

The effect of thermal annealing on the optical properties of our GaNAsSb material was discussed in the previous chapter. In order to study its effect on the device performance, sample G17-008 was grown with the same configuration as sample G16-068 (*e.g.*, structure C, n-p heterojunction). The wafer was cleaved into 4 pieces and each piece was subject to a different post-growth thermal treatment. Sample 1 (S1) was annealed at 750°C for 10 min, sample 2 (S2) at 800°C for 5 min, sample 3 (S3) at 800°C for 10 min and sample 4 (S4) at 800°C for 20 min. Both the EQE and IV were measured on each sample and the results are presented in Figure 8.6.

The first noticeable effect of the thermal treatment is the gradual increase in EQE in the 700 – 1400 nm spectrum band (Figure 8.6a). This is a direct consequence of the

reduction of the defect density which led to a large improvement in material quality. On the other hand, the EQE in the short wavelength region (400 – 700 nm) appears to gradually decrease as the thermal budget increases. This suggests that the post-growth thermal treatment degrade the material quality of the top layers and/or lead to dopant diffusion in the emitter. The bandgap was not affected by the different annealing conditions and remained at 0.97 eV. Nevertheless, the overall current density doesn't change significantly in these samples, as shown in the IV characteristics (Figure 8.6b). The solar cell parameters extracted from the IV measurements are summarized in Table 8.2.

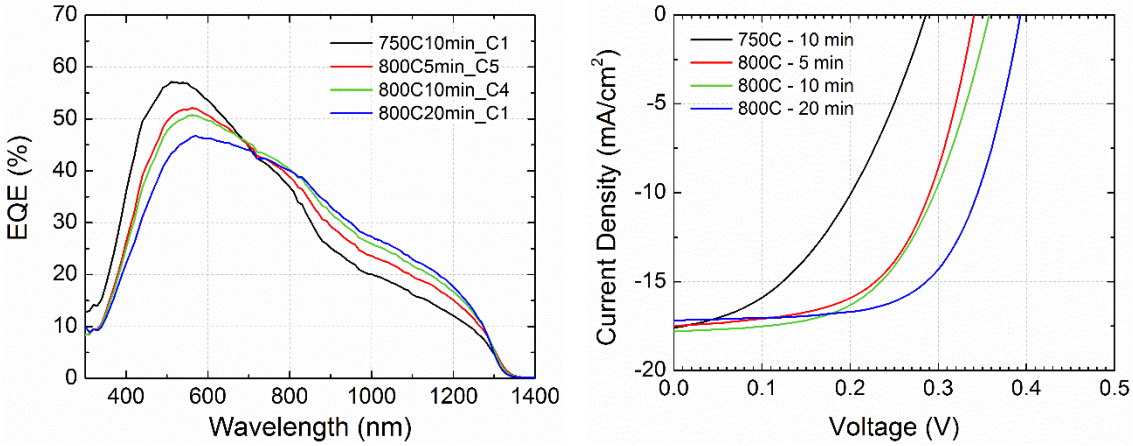

(a) (b)

Figure 8.6. a) Change in EQE with different annealing conditions, b) Evolution of V_{oc} and W_{oc} with different post-growth anneal treatment.

As explained previously, one of the main indicator of cell quality is the V_{oc}. Figure 8.7 shows that increasing the annealing temperature and annealing time resulted in a drastic increase in V_{oc} from 0.29 to 0.40 V, corresponding to a decrease of W_{oc} from 0.68 to 0.57 V. It appears that the best cell performance was obtained for a 20 min anneal at 800°C.

Table 8.2. Solar cells parameters extracted from IV measurements for sample G17-008 annealed under different conditions.

	Anneal conditions	E_g (eV)	J_{sc} (mA/cm^2)	V_{oc} (V)	W_{oc} (V)	FF	η (%)
S1	750°C – 10 min	0.97	17.6	0.29	0.68	0.56	2.86
S2	800°C – 5 min	0.97	17.5	0.34	0.63	0.59	3.51
S3	800°C – 10 min	0.97	17.8	0.36	0.61	0.55	3.52
S4	800°C – 20 min	0.97	17.2	0.40	0.57	0.64	4.40

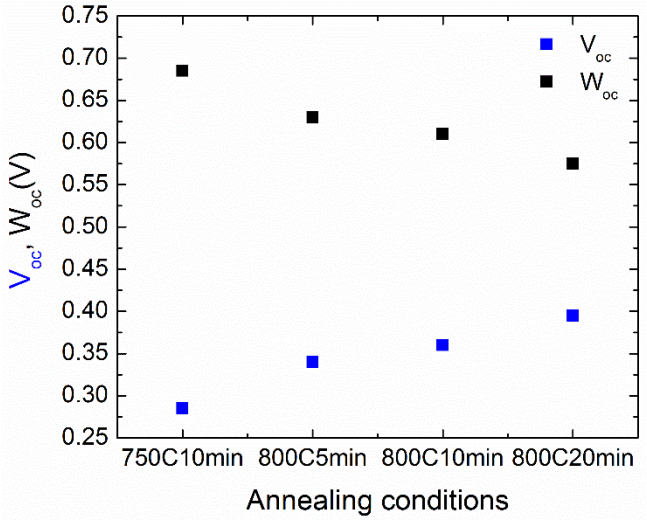

Figure 8.7. Evolution of V_{oc} and W_{oc} for different thermal treatment.

It is suspected that our cell performance might improve further with an even longer anneal however it is not recommended that the RTA furnace operates for an extended period of time at these temperatures. Therefore a maximum anneal of 20 min was used in this work. This ultimately suggests that higher V_{oc} than what is reported in this work might be achievable by simply increasing annealing temperature/time. For comparison, Polojärvi *et al.* reported a similar increase in V_{oc} with annealing. In their study, the samples were annealed at 750°C for 15 min [49].

8.4. Antireflective coating layer optimization

For III-V solar cells, about 30 % of the power is lost due to front surface reflection. Antireflective coatings (ARC) are used to ensure that light couples efficiently into the cell without being reflected back out. In this work we have opted for a standard SiO_2/SiN double layer ARC and compared the results to a simpler and more novel approach based on a flexible textured polydimethylsiloxane (PDMS) film. The optical model presented in CHAPTER 4 was used to determine the optimum ARC layer thickness for the SiO_2/SiN.

The results, shown in Figure 8.8, revealed an optimum thickness close to 40 nm/40 nm. These layers were deposited by plasma-enhanced chemical vapor deposition (PECVD). The PDMS film was developed by Holman's group at ASU. More information regarding the preparation process of this PDMS film can be found elsewhere [129], [130].

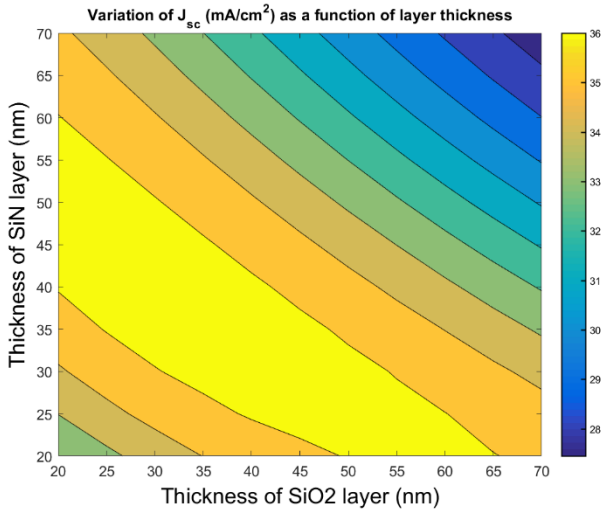

Figure 8.8. Optimum SiO_2/SiN ARC layer thickness obtained from simulation.

The EQE and IV characteristics of the n-p structure (G16-068_C1) are shown in Figure 8.9 for the different ARC investigated. For this cell, the integrated J_{sc} demonstrated a 6 % improvement upon deposition of the PDMS film and a 28 % improvement upon deposition of the SiO_2/SiN dual ARC.

The boost in J_{sc} was found to be quite dependent on the cells, indicating some cell non-uniformities. We measured a maximum J_{sc} improvement of 23 and 37 % upon deposition of the PDMS film and dual ARC, respectively, on a 1 x 1 cm cell from the same wafer. However the overall performance was lower due to shunt resistance issues on this device.

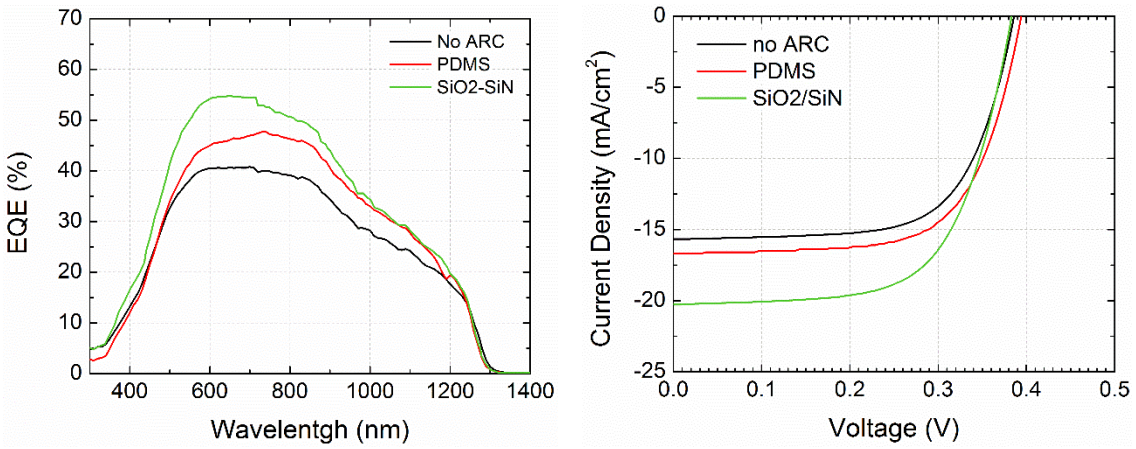

(a) (b)

Figure 8.9. a) EQE and b) IV of G16-068 (n-p) as a function of different ARC.

As can be seen in Figure 8.9b, the PDMS led to a 10 mV increase in V_{oc} while the V_{oc} remained unchanged for the SiO_2/SiN ARC. In some instance the ARC deposition even led to a decrease in V_{oc} (and FF). It is believed that the plasma used in the PECVD to deposit the ARC damages the front surface of the solar cell and hence is responsible for this loss in V_{oc}/FF. Since the PDMS film doesn't require any processing and can be taken off very easily, it does not lead to any cell damage. Nevertheless, this resulted in a 1 % (absolute) increase in efficiency for the cell coated with SiO_2/SiN (Table 8.3). The results from the PDMS are very promising considering that it is a very simple and cheap method compared to more complex ARC approaches. The use of this PDMS should be investigated further in the future.

Table 8.3. Evolution of cell performance for different ARC configuration.

	E_g (eV)	J_{sc} (mA/cm^2)	V_{oc} (V)	W_{oc} (V)	FF	η (%)
No ARC	0.96	15.7	0.39	0.57	0.66	4.1
PDMS	0.96	16.7	0.40	0.56	0.66	4.4
SiO2/SiN	0.96	20.1	0.39	0.57	0.64	5.2

Because the PDMS film can be easily taken off, the change in reflectance was measured on a large area cell (1x1 cm) at each step of the process, *i.e.*, before ARC

deposition, with the textured PDMS film and with the dual SiO_2/SiN ARC to study the change in reflectance. Again, as shown in Figure 8.10 the results from PDMS are very encouraging since the reflectance is reduced by ~ 20 %. Additionally, the single PDMS film was found to perform better than the dual-layer ARC in the IR region (1000 – 1400 nm) indicating that the optimum SiO_2/SiN ARC thickness should be revised to reduce the reflectance in that region. Other ARC materials such as SiO_2/TiO_2 or MgF_2/Ta_2O_5 are currently being investigated and are hoping to perform better in the IR region.

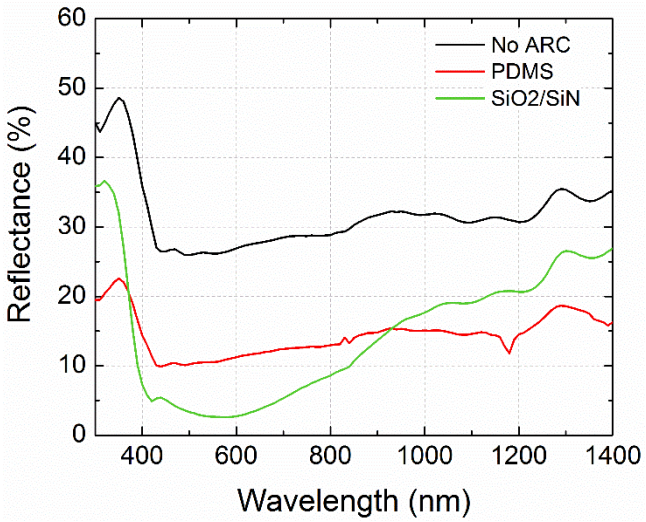

Figure 8.10. Measured reflectance of a 1x1 cm GaNAsSb solar cell before ARC deposition, with a textured PDMS film and with a standard dual SiO2/SiN ARC.

8.5. Bandgap-voltage offset

The open-circuit voltage of a solar cell is a good indicator of the cell quality as it is directly correlated to the recombination mechanisms. However it is also dependent on the bandgap, making the comparison of solar cells with different bandgap difficult. Comparing the bandgap-voltage offset W_{oc} using Equation (4.3) provides a more accurate way of comparing cell quality. A general rule of thumb is that the smaller the W_{oc} the better the cell. The current record GaAs single-junction solar cell has a W_{oc} below 0.30 V [131]. We

have achieved near 1-eV GaNAsSb solar cells with W_{oc} of 0.56 V. As demonstrated by Figure 8.11, this value is comparable to the current state-of-the-art for this type of material, although it shows that there is definitely still room for improvement. The best W_{oc} ever reported for a dilute nitride solar cell is just below 0.50 V [132].

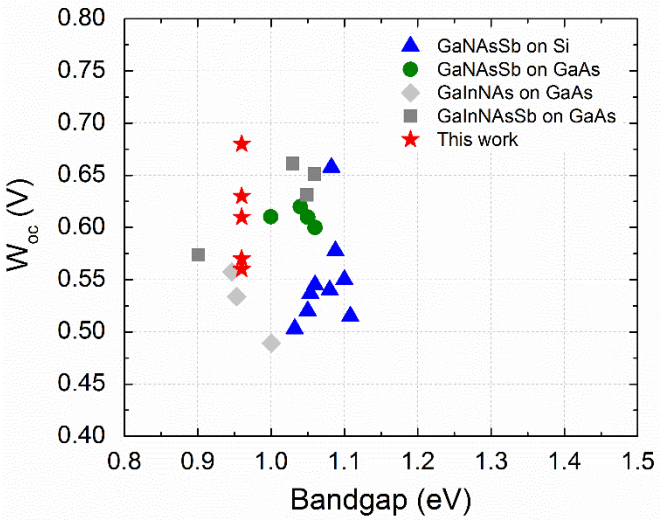

Figure 8.11. Comparison of different W_{oc} values obtained by other groups and in this work [59], [113], [132]–[137].

8.6. Summary

GaNAsSb solar cells were successfully grown and processed. Both bulk and MQW structures were investigated. Due to non-optimum interfaces associated with Sb floating on the growth surface, the MQW cells under-performed compared to the bulk structures. The effect of post-growth thermal annealing on the cell performance was investigated. The optimum annealing conditions were found to be 800°C for 20 min but the results suggested that higher temperatures or longer anneals might improve performance further. However the high thermal budget led to a degradation of the top material quality, leading to a decrease of the EQE in the short wavelength region. Two antireflective coating approaches were investigated, a standard SiO_2/SiN and a single textured PDMS film. It is the first time

that PDMS is used as ARC for this type of cells. It was found to greatly enhance the J_{sc}, although a dual-layer ARC is still better. After ARC deposition, the best device had a J_{sc} of 20.8 mA/cm^2, a FF of 64 % and a V_{oc} of 0.39 V. This corresponds to a W_{oc} of 0.57 V and an efficiency of 5.20 %, comparable to the state-of-the-art for this type of cells.

CHAPTER 9

UNDERSTANDING PERFORMANCE LIMITATIONS OF GaNAsSb SOLAR CELLS

9.1. GaAs reference cells

So far, only GaNAsSb solar cells have been investigated. Some of the questions we wanted to answer were: how would a GaAs solar cell grown under the same conditions as the dilute nitride ones perform and could that bring useful information to improve the performance of these GaNAsSb solar cells? With that in mind, four GaAs reference structures were designed using the same structures as that of the dilute nitride solar cells.

Structures D and E (G16-069 and G16-071) were based on an n-i-p structure that consisted of a 0.3-µm GaAs:Be buffer layer (1×10^{18} cm^{-3}), a 1.0-µm GaAs:Be base (5×10^{16} cm^{-3}), a 1.0-µm unintentionally doped (UID) GaAs layer, a 0.2-µm GaAs:Si emitter (2×10^{18} cm^{-3}) and a 0.03-µm $Al_{0.8}Ga_{0.2}As$ window layer (1×10^{18} cm^{-3}). The UID:GaAs layer was grown at 440°C in structure D to replicate the growth conditions of the dilute nitrides, while in structure E this layer was grown at 580°C, which is the standard growth temperature for GaAs.

Structures F and G (G16-070 and G16-072) were based on an n-p structure that consisted of a 0.45-µm GaAs:Be buffer layer (5×10^{18} cm^{-3}), a 1.0-µm GaAs:Be base (1×10^{17} cm^{-3}), a 0.2-µm GaAs:Si emitter (2×10^{18} cm^{-3}) and a 0.03-µm $Al_{0.8}Ga_{0.2}As$ window layer (1×10^{18} cm^{-3}). Similarly, the UID:GaAs layer was grown at 440°C in structure F and 580°C in structure G.

The structures of the GaAs cells are shown in Figure 9.1 for reference. Note that structures F and G did not have a BSF to reproduce the same design as structure C.

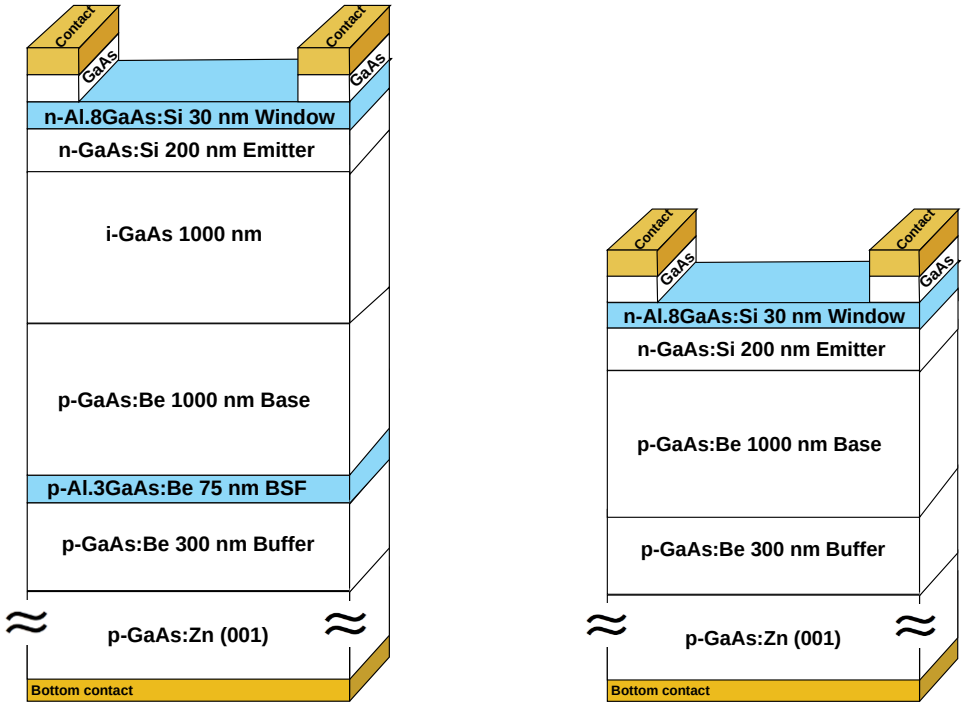

Figure 9.1. Structure design of the GaAs reference solar cells: structures D and E (left) and F and G (right)

Both EQE and IV characteristics were measured on these four devices. The results are shown in Figure 9.2 and summarized in Table 9.1.

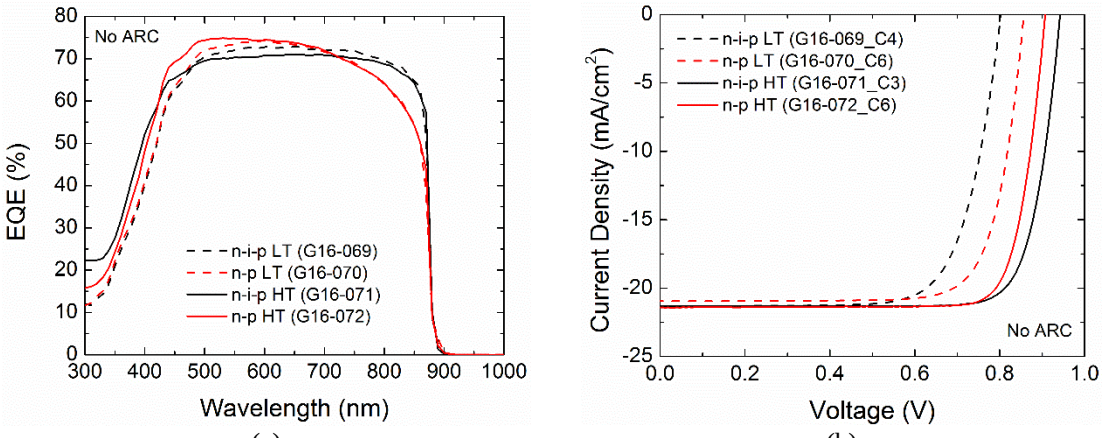

(a) (b)

Figure 9.2. a) EQE of the GaAs reference cells, b) 1-sun LIV characteristics of the GaAs reference cells.

The EQE was found not be strongly impacted by the growth temperature. The main difference appear to be that n-i-p structures present a slightly better EQE in the IR region

showing the importance of having a BSF layer to maintain low back-surface recombination velocities. The I-V characteristics however demonstrated quite different behavior. As expected, both the n-p and n-i-p structures grown at low temperature (LT) demonstrated a much lower V_{oc} than their homologue grown at normal growth temperature. Table 9.1 shows that even though there is no N or Sb, the GaAs cells grown at LT demonstrated similar W_{oc} values than the GaNAsSb solar cells (Figure 8.11). This suggests that this increase in W_{oc} is mainly due to the introduction of point defects, which are in this case not N nor Sb-related. Increasing the growth temperature should in theory result in a reduction in the density of point defects and hence, should improve the cell performance. Recent work from Leong *et al.* however suggested that, in addition to reducing the Sb incorporation, higher growth temperatures led to nitrogen phase separation in their GaNAsSb solar cells which resulted in an overall reduction in cell performance. This study indicated that GaNAsSb solar cells performed better when grown at temperatures below 500°C.

Table 9.1. Solar cell parameters obtained from 1-sun IV measurements for the GaAs reference structures D, E, F and G grown at low temperature (LT) and high temperature (HT). No ARC was applied.

	T_g (°C)	J_{sc} (mA/cm^2)	V_{oc} (V)	W_{oc} (V)	FF	η (%)
Structure D (LT n-i-p)	440	21.37	0.80	0.62	0.73	12.5
Structure E (HT n-i-p)	580	21.34	0.95	0.46	0.79	16.0
Structure F (LT n-p)	440	20.95	0.82	0.57	0.77	13.2
Structure G (HT n-p)	580	21.39	0.91	0.51	0.82	16.0

9.2. Parasitic resistance

The results presented in Table 9.1 indicated the FF of the reference GaAs solar cells was overall much higher than that of the GaNAsSb solar cells (82 % maximum for GaAs vs. 67 % maximum for GaNAsSb). Despite the fact that the J_{sc} and the V_{oc} of the dilute nitride solar cells are lower than that of GaAs, which will ultimately affect the FF, parasitic

resistance may also affect the FF. This was investigated by measuring Suns-Voc characteristics, which provide an "ideal" IV measurement without the effect of series resistance. Suns-Voc measurements provide an implied-V_{oc} (iV_{oc}) and an implied-FF (iFF), which are the maximum values you can expect to get out of your device if there was no series resistance.

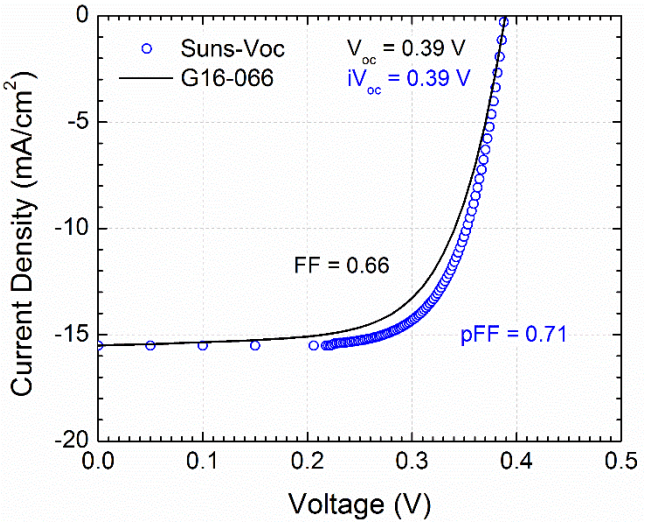

Figure 9.3. Suns-Voc measured on structure A showing the effect of series resistance on the FF.

Figure 9.3 shows that an iV_{oc} of 0.39 V was measured, comparable to the measured V_{oc} under 1-sun, with an iFF of 71 %, slightly higher than the 66 % measured under 1-sun conditions. This indicates that series resistance reduces the FF by about 5 % (absolute). Another concern (not discussed here) is that the dark saturation current of the dilute nitride solar cells was found to be about two orders of magnitude higher than that of the GaAs solar cells. This could also have a direct correlation with the low FF we measured. Improvement in material quality is necessary to reduce J_0.

9.3. In-situ anneal

Post-growth thermal treatment was shown in the previous chapter to significantly increase the V_{oc} of our GaNAsSb solar cells. However it also appeared that the thermal

treatment led to a decrease of the EQE in the blue response region (Figure 8.6a). This blue response degradation was also observed in the GaAs reference cells that underwent post-growth annealing, as shown in Figure 9.4. Interestingly, the EQE in the blue response of the GaAs cell that was annealed at 800°C for 5 min matches exactly that of the GaNAsSb solar cells (sample S2) that was subject to the same annealing conditions (dashed black curve and blue curve in Figure 9.4). This ultimately indicates that the thermal treatment alters the material quality of some of the layers in the structure (likely the AlGaAs window layer or GaAs emitter).

In order to prevent this material degradation, the post-growth RTA step was replaced step by an-situ anneal in the MBE chamber, directly after the growth of the dilute nitride layer. The process consisted in growing an n-p GaNAsSb structure similar to that presented in Figure 8.1. Following the growth of the 1-µm thick GaNAsSb base layer, a 10-nm GaAs:Si was grown to act as a protective layer. The growth was then interrupted and the substrate temperature was rapidly increased to 750°C and kept at that temperature for approximately 5 min. During this step, a continuous flow of As was maintained. RHEED was monitored throughout the entire process. As the temperature was increased above 720°C, the RHEED pattern started to change drastically and large spots began to appear before the RHEED pattern disappeared. The As flow was increased but that did not improve the RHEED pattern. Nevertheless, when the temperature was brought back down to 580°C and the rest of the GaAs emitter layer was grown, the (2×4) RHEED pattern recovered. The EQE of the resulting structure was compared to that of sample S1 which was anneal at 750°C for 10 min.

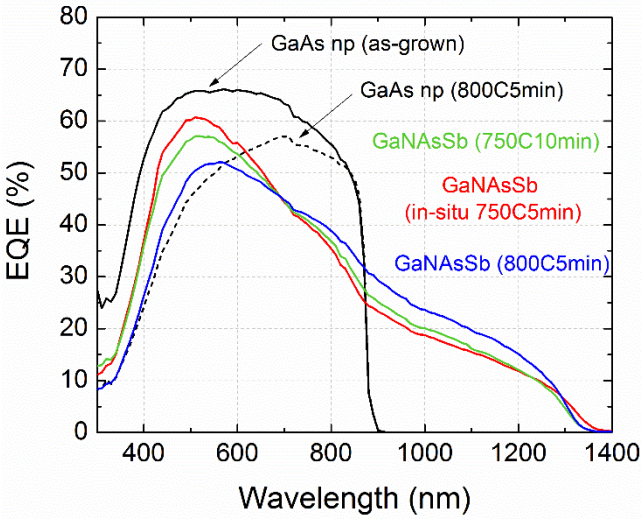

Figure 9.4. Effect of post-growth anneal and in-situ anneal on the blue response of the EQE for GaAs and GaNAsSb solar cells.

Figure 9.4 revealed that the EQE of the in-situ annealed sample (red curve) did not perform better than the sample that was annealed by RTA at 750°C for 10 min (green curve). Additionally, the LIV characteristics were also measured on both structures and similar results were observed, as shown in Figure 9.5.

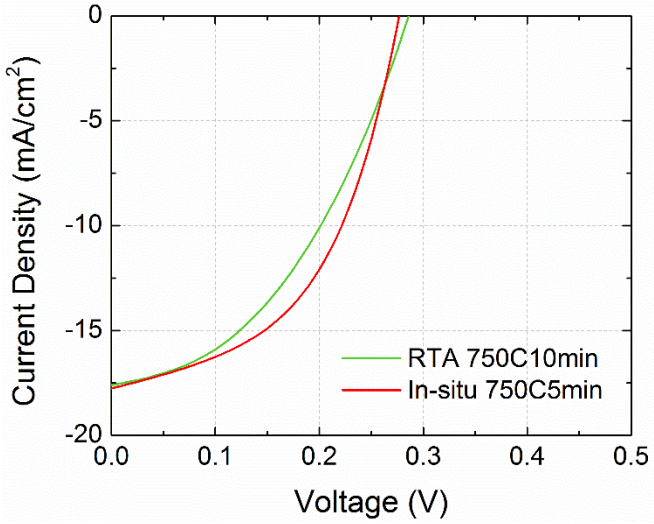

Figure 9.5. LIV characteristics of two similar n-p structures annealed by post-growth RTA and in-situ.

Unfortunately these results do not provide more insights onto what is really causing the decrease of the blue response EQE after annealing. Further analysis will be required.

9.4. Defect Density

As discussed in Section 9.1. the W_{oc} of the GaAs reference cells grown at LT was found to be similar to that of the GaNAsSb solar cells (close to 0.6 V). Ultimately, this indicates that high recombination mechanisms occur in these devices which limit their V_{oc}. In order to identify the electrically active defects and their density, DLTS analysis was performed on both a n-p GaAs reference cell grown at LT (Structure G16-070) and its homologue GaNAsSb solar cell (G16-068) in order to investigate any possible correlation between the defects present in these two cells.

The DLTS spectra shown in Figure 9.6a were obtained for the LT GaAs structure using a reverse bias (UR) of −0.6 V, a pulse bias (UP) of 0 V, a period width (Tw) of 204.8 ms, and various pulsewidths (tp) varying from 100 µs to 1 s (tp of 10 ms was used for trap signature extraction). Two peaks located at approximately 290 K and 360 K in Figure 9.6a are found. The first positive Gaussian peak at 290 K corresponds to the emission from a majority hole trap (Trap A1). The second peak at 360 K demonstrates a negative Gaussian shape indicating the emission from a minority electron trap (Trap B1) which is apparent even at UP = 0 V. Trap A1 has the following properties: E_A = 0.60 eV, $\sigma \approx 2.5 \times 10^{-14}$ cm^2, and $N_T \approx 1.54 \times 10^{14}$ cm^{-3} while trap B1 has the following properties: E_A = 0.86 eV, $\sigma \approx 3.2 \times 10^{-13}$ cm^2, and $N_T \approx 2.5 \times 10^{13}$ cm^{-3}. Trap A1 does not present any strong fit with known MBE as-grown defects in p-GaAs [138] however trap B1 presents a potential fit to the EL2 defect [139] (although it should be noted that its activation energy is slightly higher than what is typically reported for EL2 [50], [140]). This midgap defect is commonly found in GaAs grown at low temperature and is usually associated with As_{Ga} antisite defects [50].

Although still under discussion, it is possible that trap A1 corresponds to the emission of a hole from the same EL2 defect.

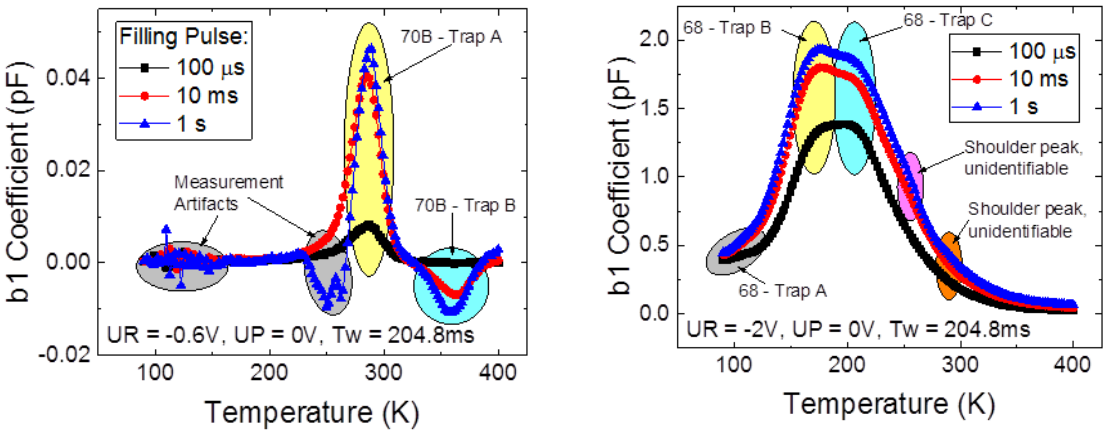

(a) (b)

Figure 9.6. a) DLTS spectra of a GaAs cell grown under the same growth conditions as the GaNAsSb cells (i.e., low growth temperature), b) DLTS spectra of a 1-eV GaNAsSb solar cell.

The DLTS spectra shown in Figure 9.6b were obtained for the GaNAsSb structure using a reverse bias (UR) of −2 V, a pulse bias (UP) of 0 V, a period width (Tw) of 204.8 ms, and also with various pulsewidths (tp) varying from 100 µs to 1 s. Three positive Gaussian peaks are apparent from the b1 coefficient spectra at approximate temperatures of 100 K, 170 K and 210 K as shown in Figure 9.6b, which correspond to the emission of three majority holes (thereafter A2, B2 and C2). Large signal swamps out smaller defect that show up as shoulders to the main peaks. These traps have the following characteristics: E_A = 0.18, 0.38 and 0.44 eV, $\sigma \approx 7.8 \times 10^{-16}$, 7.8×10^{-14} and 1.4×10^{-13} cm^2, and $N_T \approx 1.4\times10^{15}$, 6.3×10^{15} and 6.2×10^{15} cm^{-3} for traps A2, B2 and C2 respectively. These values are summarized along with those for the GaAs structure in Table 8.1. It should be noted that the N_T values were corrected for the λ-effect and the capture cross section is extracted at infinite temperature [50]. Figure 9.6b shows that the Gaussian peaks are significantly broad indicating that these might correspond to extended defects or dislocations [141]. As

explained by Polojärvi *et al.*, the nature of these traps can be investigated by varying the filling pulse [142]. As shown in Figure 9.6b, the shape of the DLTS signal evolves with increasing filling pulse and even at tp = 10 ms to 1 s, full saturation of the defects is not reached. This behavior appears to be indeed characteristics for extended defects [143]. However the presence of extended defects in this structure would be surprising as XRD revealed that this structure was well lattice-matched to GaAs (with less than 0.05 % mismatch). Another possibility, although not evidenced by the current experimental results shown in Figure 9.6b (as discussed above), is that these traps correspond to point defects. Preliminary analysis indicates that trap A2 might be a nitrogen-related shallow defect (such as N-N or N-As). Trap B2 is at ~ $0.39E_g$ which is very close to the Sb_{Ga} defects ($0.40E_g$) reported by Wicaksono e*t al.* [144]. Similarly the activation energy of trap C2 appears to be close to $0.43E_g$, which would indicate that these traps might correspond to the same EL2 defects (possibly As_{Ga} defects) observed in the LT GaAs reference cell. A general comment to be made is that the analysis of DLTS spectra and the identification of the defects nature can be quite complicated. The analysis presented here provides a hypothesis onto the possible type of defects in our material but further analysis would be required to determine their exact origin.

Table 9.2. Trap signature of the GaAs and GaNAsSb solar cell structures extracted from DLTS.

GaAs	**N_T (cm^{-3})**	**E_A (eV)**	**σ (cm^2)**
Trap A1	1.5×10^{14}	0.60	2.5×10^{-14}
Trap B1	2.5×10^{13}	0.86	3.2×10^{-13}
GaNAsSb	**N_T (cm^{-3})**	**E_A (eV)**	**σ (cm^2)**
Trap A2	1.4×10^{15}	0.18	7.8×10^{-16}
Trap B2	6.3×10^{15}	0.38	7.8×10^{-14}
Trap C2	6.2×10^{15}	0.44	1.4×10^{-13}

Regardless of the origin of these traps, it is clear that the GaNAsSb structure present noticeably higher defect density than the GaAs baseline structure. This is represented graphically in Figure 9.7. Other work on GaNAsSb have revealed quite different trap signature from what has been found in this work. Tan *et al.* reported a deep hole trap with E_A = 0.58 eV and $N_T \approx 2.4\times10^{13}$ cm^{-3} which was attributed to As_{Ga} antisite defects [113]. A more recent study by Polojärvi *et al.* showed similar findings with a trap which had the following properties: E_A = 0.56 eV, $\sigma \approx 5.6\times10^{-14}$ cm^2, and $N_T \approx 2.3\times10^{14}$ cm^{-3} [142]. These defects might also exist in our material but due to our much higher defect density (~ 10^{15} cm^{-3}), these traps might be completely swamped out and hence not detectable. It was also showed that annealing led to a strong reduction in the defect density in their GaNAsSb solar cells [142]. Similar results are expected in this work and are currently under investigation. One suspicion is that, as demonstrated in the previous chapter, the optimum annealing conditions are difficult to reach because of instrument limitation, *i.e.*, it is preferable not to operate the RTA for an extended period of time at such elevated temperatures. It was found that an anneal at 800°C for 20 min led to the highest V_{oc} of 0.4

V, however it is suspected that longer anneal might improve the V_{oc} further and would simultaneously lead to a decrease in the defect density. This will be investigated further as part of future work.

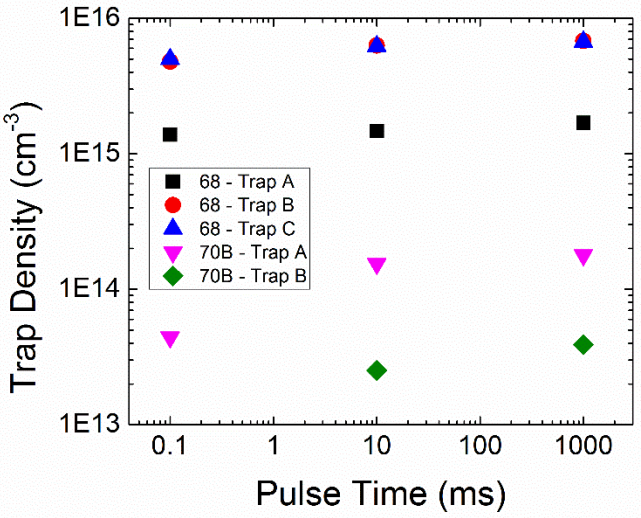

Figure 9.7. Comparison between the trap density of the GaAs structure (G16-070) and the GaNAsSb structure (G16-068) extracted from DLTS.

9.5. Background doping (C-V)

Capacitance-voltage measurements were performed to obtain the background doping density in the GaNAsSb solar cells presented in CHAPTER 8. An acceptor background doping density N_A of 7.8×10^{16} cm^{-3} was obtained on all the structures tested. The corresponding depletion width was found to extend to ~ 220 nm at –2 V. This indicates that the NID-GaNAsSb layer in these solar cell structures is not fully depleted. In order to be fully depleted, we would need $N_{A,D} < 10^{15}$ cm^{-3}. This unintentional high background doping is the reason why the n-i-p structure doesn't demonstrate a higher carrier collection than the n-p structure as the i-layer is not "intrinsic" as per say. Indeed, the cell structure is rather n-p-p and hence behaves very much like the n-p structure.

In order to understand the origin of this high background doping density, SIMS analysis was performed on a 100-nm GaNAsSb film to measure the concentration of impurities such as C, O and H. The detection limit was 5E15 at/cc for C and O and 2E17 at/cc for H.

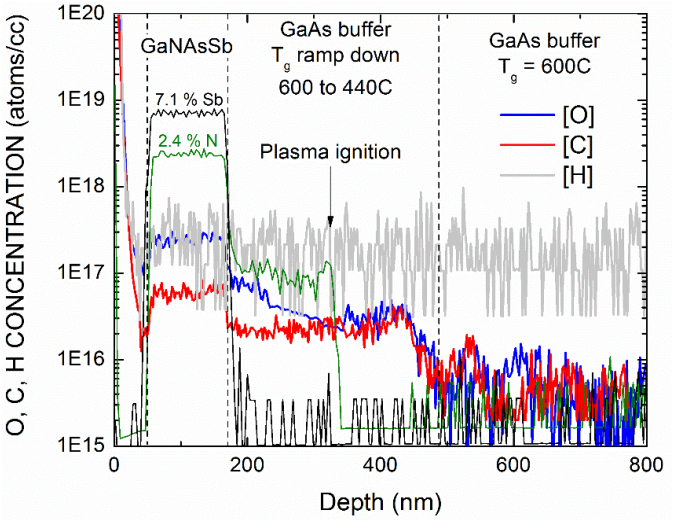

Figure 9.8. Depth profile of O, C and H impurity concentration in GaNAsSb grown at 440°C.

Figure 9.8 shows that a concentration of O, C and H of 2E17, 8E16 and 2E17 atoms/cc respectively were observed in the GaNAsSb layer. The concentration of H is at the instrument detection limit, which indicates that the actual H concentration might be lower than what was measured. The concentrations of C and O on the other hand are fairly high for MBE-grown materials. Indeed such impurity levels would be expected in MOCVD-grown materials. The other thing to notice is that the concentrations of O and C appear to follow both the growth temperature and the presence of nitrogen. The concentrations of O and C in the GaAs buffer layer grown at high temperature are at or below the instrument detection limit (in the mid-10^{15} atoms/cc). As the growth temperature of the GaAs buffer layer is ramped down to the growth temperature of 440°C, the concentration of both impurities increase to ~ 2E16 atoms/cc. Furthermore, as the nitrogen

plasma is ignited, a slight increase of the O concentration can be noted. At this point, the nitrogen shutter is still closed. The concentration O and C drastically increased to 3E17 atoms/cc as the N shutter was open to grow GaNAsSb. This indicates that the background doping is mainly controlled by the growth temperature and that impurities such as O and C might originate from the constituents of the N gas supply or are residual elements in the MBE chamber.

Additionally, Kondow *et al.* also reported on the undesirable incorporation of Al during growth of GaInNAs when the Al cell was kept at elevated temperature (in spite of keeping shutter of the Al cell closed), and also discussed the related device performance degradation [145]. Ishikawa *et al.* showed that keeping the Al cell at elevated temperature (1020°C) led to an increase in [Al], [O] and [C] although they were able to demonstrate that this could be prevented by keeping the Al cell at a much lower temperature (750°C) [146].

The incorporation of Al and its potential effect on C and O incorporation and ultimately on the performance of our solar cells has not been investigated in this work. However, since the Al cell was kept at elevated temperature during the growth of the GaNAsSb layer, this should definitely be investigated in the future.

9.6. Bi-mediated surfactant growth to reduce background doping

C-V analysis revealed that the high background doping in our GaNAsSb led to a relatively short depletion width. Ptak *et al.* showed that the use of a Bi surfactant during the growth of GaInNAs led to an increase in the net donor concentration. With that in mind, we decided to explore the use of Bi as a surfactant during the growth of our GaNAsSb material to investigate the possibility that Bi will also increase the donor concentration or

reduce the density of p-type defects in this material, which would reduce the net p-type background doping and thus improve current collection.

Bismuth has been used as a surfactant during the growth of various materials such as AlGaAs, GaInAs, GaNAs and GaInNAs and was found to reduce surface roughness and improve material quality [56], [147], [148]. Moreover Bi does not incorporate in the lattice at typical growth conditions for these materials. In this work, moderately high Bi fluxes (4.9×10^{-8} to 1.5×10^{-7} Torr) were used during the growth of 100-nm GaNAs and GaNAsSb films capped with 50-nm of GaAs. Upon the opening of the Bi shutter, the surface reconstruction switched from a (1×2) to a (1×3) pattern, in agreement with previous reports [149]. XRD data revealed that Bi led to a strong increase in N incorporation (up to 40 %) until saturation at sufficiently high Bi flux, as shown in Figure 9.9a. PL measurements, on the other hand, showed that Bi introduced under these growth conditions strongly reduced the PL intensity of GaNAsSb, as shown in Figure 9.9b. Although still at a preliminary stage, one of the plausible explanations is that the Bi flux used should be lowered by roughly an order of magnitude. Ptak *et al.* demonstrated devices with wide depletion widths ($W > 2$ μm) in GaInNAs using Bi fluxes lower than 1×10^{-8} Torr [56].

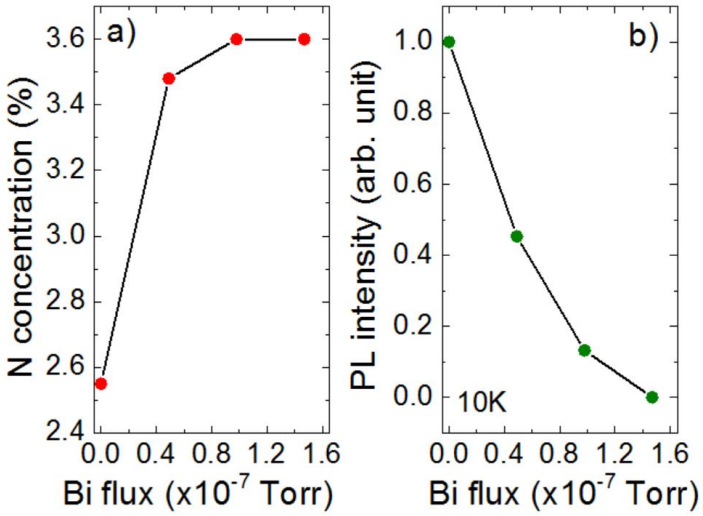

Figure 9.9. a) N composition in GaNAs films as a function of Bi flux measured by HRXRD, b) Low-temperature PL intensity of GaNAsSb(Bi) films grown with increasing Bi fluxes.

Unfortunately right after the growth of these few samples, the MBE went down to live up to its reputation of being the "most broken equipment" and therefore this study could not continue further. Future work will look at tuning the growth conditions to achieve material with satisfactory PL. Upon this milestone, GaNAsSb solar cells will be grown using Bi surfactant-mediated growth to investigate its effect on the background doping, depletion width and overall device performance.

9.7. Summary

The performance limitations of GaNAsSb solar cells were reviewed in this chapter. It was found that the main factor limiting the efficiency of our devices was the unintentional high background doping. SIMS analysis revealed the background doping is mainly controlled by the growth temperature and impurities such as O and C that most likely originate from the constituents of the N gas supply. Additionally, GaAs reference cells were grown under the same conditions as the GaNAsSb solar cells to study their performance under these growth conditions and possibly reveal details that could be useful

to improve the performance of the dilute nitride solar cells. In particular, replacement of the post-growth RTA step by an in-situ anneal was investigated. It showed that DLTS analysis revealed the presence of a similar midgap defect in both the GaAs and GaNAsSb cells. This midgap trap state could potentially arise from the EL2 defect as a result of the low growth temperature. Two additional trap states were found in the GaNAsSb solar cells. It is believed that these defects could be suppressed upon further optimization of post-growth annealing. Bismuth was proposed as a way to increase the net donor concentration and/or reduce the density of p-type defects in this material, which would reduce the net p-type background doping and thus improve current collection. Preliminary results were presented showing increase in nitrogen incorporation but decrease in photoluminescence intensity.

CHAPTER 10

CONCLUSION

10.1. Summary

The work presented in this dissertation has covered various topics ranging from the modeling to the growth and characterization of III-V and dilute nitride antimonide materials and solar cells. The main goal of this work was to investigate the potential of 1-eV GaNAsSb solar cell lattice-matched to GaAs to be used as the third cell in a multijunction solar cell.

The first part of this thesis was performed in close collaboration with Soitec Phoenix Lab. It has mainly consisted in optimizing the device structure of a four-junction, wafer-bonded solar cell. A transfer matrix method was used to model the absorption in each of the layer within the stack and the resulting quantum efficiency as well as the reflectance were modeled. This tool was found to be extremely helpful in optimizing both the device structure and the antireflective coating designs.

A great deal of work has also looked at the behavior of single-junction GaAs solar cells at elevated temperatures (up to 400°C). The solar cells were found to behave quite well up to 350°C after which severe shunting altered the diode behavior. Metal diffusion from the contacts was found to be the main source of shunting and improvements of the metallization design were proposed. These results provided the first review of the performance of GaAs solar cells at such elevated temperatures and helped develop a further understanding of their performance and limitations under these conditions.

A process to synthetize dilute nitride antimonide materials using molecular beam epitaxy has then been established. The growth of lattice-mismatched GaInAs and GaAsSb materials and the characterization of the associated strain relaxation was reviewed first. A variety of structural characterization techniques was used to show that two critical thicknesses were found in these materials. The first critical thickness corresponded to the formation of misfit dislocations while the second to dislocation multiplication and strain relaxation. Detailed optical characterization of GaAsSb films revealed the presence of compositional fluctuations which led to carrier localization effects. Tuning of the growth conditions minimized these compositional fluctuations.

A growth process was then developed and optimized to form high quality GaNAsSb films using a plasma-assisted growth technique. The incorporation of the group-V elements was examined. The increase of luminescence accompanied with a large blueshift of the emission wavelength after post growth thermal annealing was reviewed. Slow substrate rotation used during growth was found to result in the formation of superlattices, whose thickness and period can be controlled by the rotation speed and the growth rate.

Following the development of this growth capability, GaNAsSb solar cells have been grown lattice-matched to GaAs with a bandgap close to 1.0 eV. Bulk and multi-quantum well solar cells have been investigated. The performance of these single-junction GaNAsSb solar cells were reviewed. In particular, the effect of thermal annealing was discussed. Although post-growth thermal treatments led to large increase in V_{oc}, it seemed to systematically degrade the EQE in the short-wavelength region. The MQW approach underperformed with regards to the bulk structure mainly due to non-ideal GaAs/GaNAsSb interfaces. The deposition of an antireflective coating was also investigated. In particular,

a novel PDMS approach was demonstrated for the first on this of material and although not performing as good as a dual-layer ARC, results are very promising. The best device had a bandgap of 0.96 eV, with a J_{sc} of 20.8 mA/cm2, a FF of 64 % and a V_{oc} 0.39 V, corresponding to a bandgap-voltage offset W_{oc} of 0.57 V.

Finally the performance limitations of the current devices were examined. GaAs reference cells were used for comparison. Series resistance were found to limit the FF by a few percent. In-situ anneal was proposed to avoid degradation of the EQE in the short-wavelength region. Optimization of the in-situ anneal conditions would still be necessary in order to observe significant improvement. DLTS analysis revealed the presence of three hole traps in our GaNAsSb materials while CV analysis revealed that unintentional high acceptor background doping and the corresponding short depletion width (220 nm) currently limits the current collection (J_{sc}). The use of bismuth as a surfactant during growth of GaNAsSb(Bi) was proposed for the first time. It is hoped that Bi would increase the net donor concentration. Preliminary results were presented but equipment failure did not allow completion of this study, hence future work will be necessary.

The results presented in this thesis are hoped to bring further understanding of the properties of these III-V and dilute nitride materials.

10.2. Future work

The paragraphs detailed below are intended to provide a list of experimental studies that time did not allow to investigate. These should be considered as suggestions only, but represent some of the areas that could potentially improve the performance of our devices.

In my opinion, the main area of future work should focus on trying to reduce the unintentional high background doping of our GaNAsSb materials. This should be tackled

first by looking directly at the possible source of the problem: the nitrogen plasma setup itself. It was found that a high concentration of O and C was measured in our materials, which might very well originate from residual elements in our plasma. This could potentially be improved by first installing a differential pumping system which would allow the nitrogen line to be vented whenever needed. Replacing the gas purifier and investigating the resulting change in background contamination from SIMS and CV might lead to further understanding of the residual elements in the plasma. We also discussed the possible effect that keeping the Al effusion cell at elevated temperature during GaNAsSb growth might have on the unintentional incorporation of O and C. It would be interesting to grow several GaNAsSb solar cells using different Al cell temperatures during growth of the GaNAsSb layer, to investigate the effect on the resulting background doping density.

The use of deflection was not found to improve the material quality in this work but it is possible that the defect density is still too high at the moment to notice any improvement. Upon further reducing of the background doping and the defect density, the use of deflection plates should be investigated further.

The work on surfactant-mediated growth using bismuth surfactant is very interesting since it has never been demonstrated on GaNAsSb before. Unfortunately the MBE system decided to not cooperate and thus this study could not be completed. This should definitely be investigated further in the future as it has great potential for improving device performance.

Although most the work in this thesis has focused on GaNAsSb, it should not be forgotten that world record results were achieved with GaInNAs(Sb). The growth capability for GaNAsSb has now been developed in this work but development of a growth

process for GaInNAs-based materials should also be considered in the future. The implementation from the process developed in this thesis should be straightforward. These GaInNAs(Sb) materials have great potential for 1-eV solar cells and other long wavelength applications.

Finally, a baseline growth process to realize single-junction GaAs solar cells was established within the framework of this dissertation work. Although satisfactory for test structures, the performance of these GaAs cells still have room for improvement, especially at the V_{oc} level which is currently at ~ 0.95 V while the state-of-the-art is at 1.1 V. Here are a suggestions that should improve the V_{oc} of these baseline cells. First, a growth procedure has also been established in this work to grow $Ga_{0.51}In_{0.49}P$ lattice-matched to GaAs. This process should be implemented to replace the AlGaAs window layer that is currently used. This also applies to the GaNAsSb solar cells. AlGaAs does not like oxygen and we seem to have quite a lot of it, therefore GaInP would seem to be more appropriate. Furthermore, GaInP might be more resistant to the high temperatures needed during post-growth anneal and hence, the EQE in the short-wavelength might also benefit. ARC deposition of SiO_2/SiN was also found to decrease the V_{oc} on our GaAs cells. This could be related to degradation of the AlGaAs window layer and might disappear upon replacement of AlGaAs with GaInP. Regardless, the plasma conditions of the PECVD should be tuned to avoid this loss in V_{oc} or other deposition technique should be considered (such as sputtering or evaporation for instance).

REFERENCES

[1] T. F. Stocker *et al.*, "Climate Change 2013: The Physical Science Basis, Cambridge University Press, Cambridge, United Kingdom and New York, NY, USA.," IPCC, 2013.

[2] T. F. Stocker *et al.*, *Climate change 2013: The physical science basis*. Cambridge University Press Cambridge, UK, and New York, 2014.

[3] "Climate Stabilization Targets: Emissions, Concentrations, and Impacts over Decades to Millennia," National Research Council. The National Academies Press, Washington, DC, USA, 2011.

[4] "Adoption of the Paris agreement," United Nations , Frameword Convention on Climate Change, FCCC/CP/2015/L.9/Rev.1, 2015.

[5] "Solar Energy Perspective," IEA International Energy Agency, 2011.

[6] "Trends 2016 in Photovoltaic Applications," IEA International Energy Agency, IEA PVPS T1-30:2016, 2016.

[7] "Photovoltaics Report," Fraunhofer Institute for Solar Energy Systems, ISE, Oct. 2016.

[8] M. A. Green, K. Emery, Y. Hishikawa, W. Warta, and E. D. Dunlop, "Solar cell efficiency tables (version 48): Solar cell efficiency tables (version 48)," *Prog. Photovolt. Res. Appl.*, vol. 24, no. 7, pp. 905–913, Jul. 2016.

[9] W. Shockley and H. J. Queisser, "Detailed Balance Limit of Efficiency of p-n Junction Solar Cells," *J. Appl. Phys.*, vol. 32, no. 3, p. 510, 1961.

[10] M. A. Green, "Third generation photovoltaics: Ultra-high conversion efficiency at low cost," *Prog. Photovolt. Res. Appl.*, vol. 9, no. 2, pp. 123–135, 2001.

[11] R. R. King, "Raising the efficiency ceiling in multijunction solar cells," *Spectrolab IncSep 2009 Retrieved Internet*, pp. 1–76, 2009.

[12] "Press release, Fraunhofer Institute for Solar Energy Systems," 01-Dec-2014.

[13] M. Woodhouse and A. Goodrich, "Manufacturing Cost Analysis Relevant to Single- and Dual-Junction Photovoltaic Cells Fabricated with III-Vs and III-Vs Grown on Czochralski Silicon (Presentation)," National Renewable Energy Laboratory (NREL), Golden, CO., 2014.

[14] F. Dimroth, “High-efficiency solar cells from III-V compound semiconductors,” *Phys. Status Solidi C*, vol. 3, no. 3, pp. 373–379, Mar. 2006.

[15] M. Yamaguchi, T. Takamoto, K. Araki, and N. Ekins-Daukes, “Multi-junction III–V solar cells: current status and future potential,” *Sol. Energy*, vol. 79, no. 1, pp. 78–85, Jul. 2005.

[16] R. A. Sinton, Y. Kwark, J. Y. Gan, and R. M. Swanson, “27.5-percent silicon concentrator solar cells,” *IEEE Electron Device Lett.*, vol. 7, no. 10, pp. 567–569, 1986.

[17] S. P. Philipps, A. W. Bett, K. Horowitz, and S. Kurtz, “Current Status of Concentrator Photovoltaic (CPV) Technology,” Fraunhofer ISE, NREL, 2016.

[18] S. P. Bremner, M. Y. Levy, and C. B. Honsberg, “Analysis of tandem solar cell efficiencies under AM1.5G spectrum using a rapid flux calculation method,” *Prog. Photovolt. Res. Appl.*, vol. 16, no. 3, pp. 225–233, May 2008.

[19] “Press Release, Solar Junction,” 15-Oct-2012.

[20] “Press Release, Sharp Corporation,” 14-Jun-2013.

[21] “Press Release, NREL,” 16-Dec-2014.

[22] K. A. W. Horowitz, M. Woodhouse, G. Smestad, and H. Lee, “A Bottom-up Cost Analysis of a High Concentratin PV Module.” Apr-2015.

[23] J. Adams *et al.*, “Demonstration of multiple substrate reuses for inverted metamorphic solar cells,” in *Photovoltaic Specialists Conference (PVSC), Volume 2, 2012 IEEE 38th*, 2012, pp. 1–6.

[24] M. Yamaguchi, “Radiation resistance of compound semiconductor solar cells,” *J. Appl. Phys.*, vol. 78, no. 3, p. 1476, 1995.

[25] P. Patel *et al.*, “Experimental Results From Performance Improvement and Radiation Hardening of Inverted Metamorphic Multijunction Solar Cells,” *IEEE J. Photovolt.*, vol. 2, no. 3, pp. 377–381, Jul. 2012.

[26] M. Kondow, K. Uomi, A. Niwa, T. Kitatani, S. Watahiki, and Y. Yazawa, “GaInNAs: A Novel Material for Long-Wavelength-Range Laser Diodes with Excellent High-Temperature Performance,” *Jpn J Appl Phys*, vol. 35, p. 1273, 1996.

[27] A. Maros *et al.*, “Critical thickness investigation of MBE-grown GaInAs/GaAs and GaAsSb/GaAs heterostructures,” *J. Vac. Sci. Technol. B Nanotechnol.*

Microelectron. Mater. Process. Meas. Phenom., vol. 34, no. 2, p. 02L113, Mar. 2016.

[28] A. Maros, N. N. Faleev, M. I. Bertoni, C. B. Honsberg, and R. R. King, "Carrier localization effects in GaAs1−xSbx/GaAs heterostructures," *J. Appl. Phys.*, vol. 120, no. 18, p. 183104, Nov. 2016.

[29] A. Maros, N. Faleev, R. R. King, and C. B. Honsberg, "Growth and characterization of GaAs1−x−ySbxNy/GaAs heterostructures for multijunction solar cell applications," *J. Vac. Sci. Technol. B Nanotechnol. Microelectron. Mater. Process. Meas. Phenom.*, vol. 34, no. 2, p. 02L106, Mar. 2016.

[30] J. Simon, K. L. Schulte, D. L. Young, N. M. Haegel, and A. J. Ptak, "GaAs Solar Cells Grown by Hydride Vapor-Phase Epitaxy and the Development of GaInP Cladding Layers," *IEEE J. Photovolt.*, vol. 6, no. 1, pp. 191–195, Jan. 2016.

[31] T. Kim, "Characteristics of Bulk Dilute-Nitride-Antimonide Materials Grown by MOVPE for High-Efficiency Multi-Junction Solar Cell," University of Wisconsin-Madison, 2014.

[32] A. J. Ptak, S. W. Johnston, S. Kurtz, D. J. Friedman, and W. K. Metzger, "A comparison of MBE-and MOCVD-grown GaInNAs," *J. Cryst. Growth*, vol. 251, no. 1, pp. 392–398, 2003.

[33] A. Aho, "Dilute Nitride Multijunction Solar Cells Grown by Molecular Beam Epitaxy," Tampere University of Technology, 2015.

[34] A. J. Ptak, D. J. Friedman, S. Kurtz, and R. C. Reedy, "Low-acceptor-concentration GaInNAs grown by molecular-beam epitaxy for high-current p-i-n solar cell applications," *J. Appl. Phys.*, vol. 98, no. 9, p. 94501, 2005.

[35] J. W. Matthews and A. E. Blakeslee, "Defects in epitaxial multilayers: I. Misfit dislocations," *J. Cryst. Growth*, vol. 27, pp. 118–125, 1974.

[36] F. C. Frank and J. H. Van Der Merwe, "One-dimensional dislocations. I. Static Theory," *Proc. R. Soc. Lond.*, vol. A198, no. 1053, pp. 205–216, 1949.

[37] E. A. Fitzgerald, "Dislocations in strained-layer epitaxy: theory, experiment, and applications," *Mater. Sci. Rep.*, vol. 7, no. 3, pp. 87–142, 1991.

[38] I. Vurgaftman, J. R. Meyer, and L. R. Ram-Mohan, "Band parameters for III–V compound semiconductors and their alloys," *J. Appl. Phys.*, vol. 89, no. 11, p. 5815, 2001.

[39] R. C. Longsworth, “Cryopump regeneration studies,” *J. Vac. Sci. Technol.*, vol. 21, no. 4, p. 1022, Nov. 1982.

[40] *Epitaxial Crystal Growth: Methods and Materials*. Springer Handbooks of Electronic and Photonic Materials, 2006.

[41] H. B. Yuen, “Growth and characterization of dilute nitride antimonides for long-wavelength optoelectronics,” Stanford University, 2006.

[42] M. A. Wistey, “Growth of 1.5 um GaInNAsSb vertical cavity surface emitting lasers by molecular beam epitaxy,” Ph.D. dissertation, Stanford University, 2006.

[43] G. K. Vijaya, A. Freundlich, D. Tang, and D. J. Smith, “MBE growth of sharp interfaces in dilute-nitride quantum wells with improved nitrogen-plasma design,” *J. Vac. Sci. Technol. B Nanotechnol. Microelectron. Mater. Process. Meas. Phenom.*, vol. 33, no. 3, p. 31209, May 2015.

[44] M. A. Wistey, S. R. Bank, H. B. Yuen, H. Bae, and J. S. Harris, “Nitrogen plasma optimization for high-quality dilute nitrides,” *J. Cryst. Growth*, vol. 278, no. 1–4, pp. 229–233, May 2005.

[45] D. B. Jackrel, “InGaAs and GaInNAs(Sb) 1064 nm Photodetectors and Solar Cells on GaAs Substrates,” Ph.D. dissertation, Stanford University, 2005.

[46] V. M. Kaganer, R. Köhler, M. Schmidbauer, R. Opitz, and B. Jenichen, “X-ray diffraction peaks due to misfit dislocations in heteroepitaxial structures,” *Phys. Rev. B*, vol. 55, no. 3, p. 1793, 1997.

[47] D. R. Black and G. G. Long, “960-10Special.”

[48] D. K. Schroder, *Semiconductor Material and Device Characterization*, Third Edition. John Wiley & Sons, Inc., 2006.

[49] V. Polojärvi, A. Aho, A. Tukiainen, A. Schramm, and M. Guina, “Comparative study of defect levels in GaInNAs, GaNAsSb, and GaInNAsSb for high-efficiency solar cells,” *Appl. Phys. Lett.*, vol. 108, no. 12, p. 122104, Mar. 2016.

[50] K. J. Schmieder *et al.*, “Effect of Growth Temperature on GaAs Solar Cells at High MOCVD Growth Rates,” *IEEE J. Photovolt.*, vol. 7, no. 1, pp. 340–346, Jan. 2017.

[51] J. F. Geisz, M. A. Steiner, I. García, S. R. Kurtz, and D. J. Friedman, “Enhanced external radiative efficiency for 20.8% efficient single-junction GaInP solar cells,” *Appl. Phys. Lett.*, vol. 103, no. 4, pp. 41118–41118, 2013.

[52] E. Yablonovitch, O. D. Miller, and S. R. Kurtz, “The opto-electronic physics that broke the efficiency limit in solar cells,” in *Photovoltaic Specialists Conference (PVSC), 2012 38th IEEE*, 2012, pp. 1556–1559.

[53] B. M. Kayes *et al.*, “27.6% conversion efficiency, a new record for single-junction solar cells under 1 sun illumination,” in *Photovoltaic Specialists Conference (PVSC), 2011 37th IEEE*, 2011, pp. 4–8.

[54] A. Gubanov, V. Polojärvi, A. Aho, A. Tukiainen, N. V. Tkachenko, and M. Guina, “Dynamics of time-resolved photoluminescence in GaInNAs and GaNAsSb solar cells,” *Nanoscale Res. Lett.*, vol. 9, no. 1, pp. 1–4, 2014.

[55] D. J. Friedman, A. J. Ptak, S. R. Kurtz, and J. F. Geisz, “Analysis of depletion-region collection in GaInNAs solar cells,” in *Photovoltaic Specialists Conference, 2005. Conference Record of the Thirty-first IEEE*, 2005, pp. 691–694.

[56] A. J. Ptak, R. France, C.-S. Jiang, and R. C. Reedy, “Effects of bismuth on wide-depletion-width GaInNAs solar cells,” *J. Vac. Sci. Technol. B Microelectron. Nanometer Struct.*, vol. 26, no. 3, p. 1053, 2008.

[57] J. Nelson, *The Physics of Solar Cells*. Imperial College Press, 2003.

[58] R. R. King *et al.*, “Band gap-voltage offset and energy production in next-generation multijunction solar cells,” *Prog. Photovolt. Res. Appl.*, vol. 19, no. 7, pp. 797–812, 2011.

[59] N. Leong *et al.*, “Growth of 1-eV GaNAsSb-based photovoltaic cell on silicon substrate at different As/Ga beam equivalent pressure ratios,” *Prog. Photovolt. Res. Appl.*, p. n/a-n/a, 2015.

[60] “Standard Solar Spectra.” [Online]. Available: http://rredc.nrel.gov/solar/spectra/.

[61] L. A. Pettersson, L. S. Roman, and O. Inganas, “Modeling photocurrent action spectra of photovoltaic devices based on organic thin films,” *J. Appl. Phys.*, vol. 86, no. 1, pp. 487–496, 1999.

[62] J. S. C. Prentice, “Coherent, partially coherent and incoherent light absorption in thin-film multilayer structures,” *J. Phys. Appl. Phys.*, vol. 33, no. 24, p. 3139, 2000.

[63] E. Centurioni, “Generalized matrix method for calculation of internal light energy flux in mixed coherent and incoherent multilayers,” *Appl. Opt.*, vol. 44, no. 35, pp. 7532–7539, 2005.

[64] G. F. Burkhard, E. T. Hoke, and M. D. McGehee, “Accounting for Interference, Scattering, and Electrode Absorption to Make Accurate Internal Quantum Efficiency Measurements in Organic and Other Thin Solar Cells,” *Adv. Mater.*, vol. 22, no. 30, pp. 3293–3297, Aug. 2010.

[65] F. Dimroth *et al.*, “Wafer bonded four-junction GaInP/GaAs//GaInAsP/GaInAs concentrator solar cells with 44.7% efficiency: Wafer bonded four-junction concentrator solar cells with 44.7% efficiency,” *Prog. Photovolt. Res. Appl.*, p. n/a-n/a, Jan. 2014.

[66] A. Maros *et al.*, “High temperature characterization of GaAs single junction solar cells,” in *Photovoltaic Specialist Conference (PVSC), 2015 IEEE 42nd*, 2015, pp. 1–5.

[67] P. D. Wienhold and D. F. Persons, “The development of high-temperature composite solar array substrate panels for the MESSENGER spacecraft,” *SAMPE J.*, vol. 39, no. 6, pp. 6–17, 2003.

[68] J. Kinnison et al., “The Solar Probe+ Mission: A New Concept for Close Solar Encounters,” *59th Int. Astronaut. Congr.*, Oct. 2008.

[69] Y. Tripanagnostopoulos, T. H. Nousia, M. Souliotis, and P. Yianoulis, “Hybrid photovoltaic/thermal solar systems,” *Sol. Energy*, vol. 72, no. 3, pp. 217–234, 2002.

[70] P. G. Charalambous, G. G. Maidment, S. A. Kalogirou, and K. Yiakoumetti, “Photovoltaic thermal (PV/T) collectors: A review,” *Appl. Therm. Eng.*, vol. 27, no. 2–3, pp. 275–286, Feb. 2007.

[71] T. T. Chow, “A review on photovoltaic/thermal hybrid solar technology,” *Appl. Energy*, vol. 87, no. 2, pp. 365–379, Feb. 2010.

[72] V. V. Tyagi, S. C. Kaushik, and S. K. Tyagi, “Advancement in solar photovoltaic/thermal (PV/T) hybrid collector technology,” *Renew. Sustain. Energy Rev.*, vol. 16, no. 3, pp. 1383–1398, Apr. 2012.

[73] S. P. Philipps, D. Stetter, R. Hoheisel, M. Hermle, F. Dimroth, and A. W. Bett, “Characterization and numerical modeling of the temperature-dependent behavior of GaAs solar cells,” in *23rd European Photovoltaic Solar Energy Conference*, 2008, vol. 114.

[74] S. P. Philipps *et al.*, “An experimental and theoretical study on the temperature dependence of GaAs solar cells,” in *Photovoltaic Specialists Conference (PVSC), 2011 37th IEEE*, 2011, pp. 1610–1614.

[75] Y. P. Varshni, “Temperature dependence of the energy gap in semiconductors,” *Physica*, vol. 34, no. 1, pp. 149–154, 1967.

[76] “Stephan Suckow, 2/3-Diode Fit (2014). http://nanohub.org/resources/14300. 1.3.” .

[77] T. Anan, K. Nishi, S. Sugou, M. Yamada, K. Tokutome, and A. Gomyo, “GaAsSb: A novel material for 1.3μm VCSELs,” *Electron. Lett.*, vol. 34, no. 22, p. 2127, 1998.

[78] Xiaoguang Sun *et al.*, “GaAsSb: a novel material for near infrared photodetectors on GaAs substrates,” *IEEE J. Sel. Top. Quantum Electron.*, vol. 8, no. 4, pp. 817–822, Jul. 2002.

[79] R. U. Martinelli, T. J. Zamerowski, and P. A. Longeway, “2.6 μm InGaAs photodiodes,” *Appl. Phys. Lett.*, vol. 53, no. 11, p. 989, 1988.

[80] N. Chand, E. E. Becker, J. P. van der Ziel, S. N. G. Chu, and N. K. Dutta, “Excellent uniformity and very low (<50 A/cm2) threshold current density strained InGaAs quantum well diode lasers on GaAs substrate,” *Appl. Phys. Lett.*, vol. 58, no. 16, p. 1704, 1991.

[81] J. F. Geisz *et al.*, “Inverted GaInP/(In) GaAs/InGaAs triple-junction solar cells with low-stress metamorphic bottom junctions,” in *Photovoltaic Specialists Conference, 2008. PVSC’08. 33rd IEEE,* 2008, pp. 1–5.

[82] P. Patel *et al.*, “Initial results of the monolithically grown six-junction inverted metamorphic multi-junction solar cell,” in *Photovoltaic Specialists Conference (PVSC), Volume 2, 2012 IEEE 38th*, 2012, pp. 1–4.

[83] S. P. Bremner, K.-Y. Ban, N. N. Faleev, C. B. Honsberg, and D. J. Smith, “Impact of stress relaxation in GaAsSb cladding layers on quantum dot creation in InAs/GaAsSb structures grown on GaAs (001),” *J. Appl. Phys.*, vol. 114, no. 10, p. 103511, 2013.

[84] P. F. Fewster, “X-ray diffraction from low-dimensional structures,” *Semicond Sci Technol*, vol. 8, pp. 1915–1934, 1993.

[85] Y. Takagi, Y. Furukawa, A. Wakahara, and H. Kan, “Lattice relaxation process and crystallographic tilt in GaP layers grown on misoriented Si(001) substrates by metalorganic vapor phase epitaxy,” *J. Appl. Phys.*, vol. 107, no. 6, p. 63506, 2010.

[86] Y. C. Chen and P. K. Bhattacharya, “Determination of critical layer thickness and strain tensor in InxGa1- xAs/GaAs quantum-well structures by x-ray diffraction,” *J. Appl. Phys.*, vol. 73, no. 11, pp. 7389–7394, 1993.

[87] A. V. Drigo *et al.*, “On the mechanisms of strain release in molecular-beam-epitaxy-grown InxGa1−xAs/GaAs single heterostructures,” *J. Appl. Phys.*, vol. 66, no. 5, p. 1975, 1989.

[88] C. G. Tuppen, C. J. Gibbings, and M. Hockly, “The effects of misfit dislocation nucleation and propagation on Si/SiGe critical thickness values,” *J. Cryst. Growth*, vol. 94, pp. 392–404, 1989.

[89] R. H. Dixon and P. J. Goodhew, “On the origin of misfit dislocations in InGaAs/GaAs strained layers,” *J. Appl. Phys.*, vol. 68, no. 7, p. 3163, 1990.

[90] J. Y. Tsao, B. W. Dodson, S. T. Picraux, and D. M. Cornelison, “Critical stresses for Si x Ge 1- x strained-layer plasticity,” *Phys. Rev. Lett.*, vol. 59, no. 21, p. 2455, 1987.

[91] S. A. Lourenço, I. F. L. Dias, J. L. Duarte, E. Laureto, V. M. Aquino, and J. C. Harmand, “Temperature-dependent photoluminescence spectra of GaAsSb/AlGaAs and GaAsSbN/GaAs single quantum wells under different excitation intensities,” *Braz. J. Phys.*, vol. 37, no. 4, pp. 1212–1219, 2007.

[92] A. Aït-Ouali, A. Chennouf, R. Y.-F. Yip, J. L. Brebner, R. Leonelli, and R. A. Masut, “Localization of excitons by potential fluctuations and its effect on the Stokes shift in InGaP/InP quantum confined heterostructures,” *J. Appl. Phys.*, vol. 84, no. 10, p. 5639, 1998.

[93] A. Aït-Ouali, R. Y.-F. Yip, J. L. Brebner, and R. A. Masut, “Strain relaxation and exciton localization effects on the Stokes shift in InAsP/InP multiple quantum wells,” *J. Appl. Phys.*, vol. 83, no. 6, p. 3153, 1998.

[94] Y. G. Sadofyev and N. Samal, “Photoluminescence and Band Alignment of Strained GaAsSb/GaAs QW Structures Grown by MBE on GaAs,” *Materials*, vol. 3, no. 3, pp. 1497–1508, Feb. 2010.

[95] L. Vina, S. Logothetidis, and M. Cardona, “Temperature dependence of the dielectric function of germanium,” *Phys. Rev. B*, vol. 30, no. 4, p. 1979, 1984.

[96] R. Pässler, “Basic Model Relations for Temperature Dependencies of Fundamental Energy Gaps in Semiconductors,” *Phys Stat Sol B*, vol. 200, p. 155, 1997.

[97] Q. Li *et al.*, “Thermal redistribution of localized excitons and its effect on the luminescence band in InGaN ternary alloys,” *Appl. Phys. Lett.*, vol. 79, no. 12, p. 1810, 2001.

[98] Q. Li, S. J. Xu, M. H. Xie, and S. Y. Tong, “A model for luminescence of localized state ensemble,” *ArXiv Prepr. Cond-Mat0411128*, 2004.

[99] M. M. Karow, N. N. Faleev, D. J. Smith, and C. B. Honsberg, “Defect creation in InGaAs/GaAs multiple quantum wells–I. Structural properties,” *J. Cryst. Growth*, Apr. 2015.

[100] M. M. Karow, N. N. Faleev, A. Maros, and C. B. Honsberg, “Defect Creation in InGaAs/GaAs Multiple Quantum Wells – II. Optical Properties,” *J. Cryst. Growth*, Apr. 2015.

[101] L. C. Hirst *et al.*, “Spatially indirect radiative recombination in InAlAsSb grown lattice-matched to InP by molecular beam epitaxy,” *J. Appl. Phys.*, vol. 117, no. 21, p. 215704, Jun. 2015.

[102] Y.-E. Ihm, N. Otsuka, J. Klem, and H. Morkoç, “Ordering in GaAs1−xSbx grown by molecular beam epitaxy,” *Appl. Phys. Lett.*, vol. 51, no. 24, p. 2013, 1987.

[103] Y. Kawamura, A. Gomyo, T. Suzuki, T. Higashino, and N. Inoue, “Band-gap change in ordered/disordered GaAs1-ySby layers grown on (001) and (111) B InP substrates,” *Jpn. J. Appl. Phys.*, vol. 41, no. 4B, p. L447, 2002.

[104] B. P. Gorman *et al.*, “Atomic ordering-induced band gap reductions in GaAsSb epilayers grown by molecular beam epitaxy,” *J. Appl. Phys.*, vol. 97, no. 6, p. 63701, 2005.

[105] R. Teissier, D. Sicault, J. C. Harmand, G. Ungaro, G. Le Roux, and L. Largeau, “Temperature-dependent valence band offset and band-gap energies of pseudomorphic GaAsSb on GaAs,” *J. Appl. Phys.*, vol. 89, no. 10, p. 5473, 2001.

[106] T. S. Wang, J. T. Tsai, K. I. Lin, J. S. Hwang, H. H. Lin, and L. C. Chou, “Characterization of band gap in GaAsSb/GaAs heterojunction and band alignment in GaAsSb/GaAs multiple quantum wells,” *Mater. Sci. Eng. B*, vol. 147, no. 2–3, pp. 131–135, Feb. 2008.

[107] G. Ungaro, G. Le Roux, R. Teissier, and J. C. Harmand, “GaAsSbN: a new low-bandgap material for GaAs substrates,” *Electron. Lett.*, vol. 35, no. 15, pp. 1246–1248, 1999.

[108] H. B. Yuen, S. R. Bank, M. A. Wistey, J. S. Harris, and A. Moto, “Comparison of GaNAsSb and GaNAs as quantum-well barriers for GaInNAsSb optoelectronic devices operating at 1.3–1.55 μm,” *J. Appl. Phys.*, vol. 96, no. 11, p. 6375, 2004.

[109] H. B. Yuen *et al.*, “Improved optical quality of GaNAsSb in the dilute Sb limit,” *J. Appl. Phys.*, vol. 97, no. 11, p. 113510, 2005.

[110] S. Wicaksono, S. F. Yoon, K. H. Tan, and W. K. Loke, “Characterization of small-mismatch GaAsSbN on GaAs grown by solid source molecular beam epitaxy,” *J. Vac. Sci. Technol. B Microelectron. Nanometer Struct.*, vol. 23, no. 3, p. 1054, 2005.

[111] S. Wicaksono, S. F. Yoon, K. H. Tan, and W. K. Cheah, "Concomitant incorporation of antimony and nitrogen in GaAsSbN lattice-matched to GaAs," *J. Cryst. Growth*, vol. 274, no. 3–4, pp. 355–361, Feb. 2005.

[112] T. K. Ng *et al.*, "1eV GANxAs1-x-ySby material for lattice-matched III-V solar cell implementation on GaAs and Ge," 2009, pp. 000076–000080.

[113] K. H. Tan *et al.*, "Molecular beam epitaxy grown GaNAsSb 1eV photovoltaic cell," *J. Cryst. Growth*, vol. 335, no. 1, pp. 66–69, Nov. 2011.

[114] K. H. Tan *et al.*, "Study of a 1 eV GaNAsSb photovoltaic cell grown on a silicon substrate," *Appl. Phys. Lett.*, vol. 104, no. 10, p. 103906, Mar. 2014.

[115] S. Z. Wang, S. F. Yoon, and W. K. Loke, "Effects of surface nitridation during nitrogen plasma ignition on optical quality of GaInAsN grown by solid source molecular beam epitaxy," *J. Appl. Phys.*, vol. 94, no. 4, p. 2662, 2003.

[116] M. Kondow and T. Kitatani, "Molecular beam epitaxy of GaNAs and GaInNAs," *Semicond. Sci. Technol.*, vol. 17, no. 8, p. 746, 2002.

117] T.-C. Ma, Y.-T. Lin, and H.-H. Lin, "Incorporation behaviors of group V elements in GaAsSbN grown by gas-source molecular-beam epitaxy," *J. Cryst. Growth*, vol. 310, no. 11, pp. 2854–2858, May 2008.

[118] A. Maros, N. Faleev, S. H. Lee, J. S. Kim, C. B. Honsberg, and R. R. King, "1-eV GaNAsSb for multijunction solar cells," *2016 IEEE 43rd Photovolt. Spec. Conf. PVSC Portland OR*, pp. 2306–2309, 2016.

[119] J. C. Harmand, G. Ungaro, L. Largeau, and G. Le Roux, "Comparison of nitrogen incorporation in molecular-beam epitaxy of GaAsN, GaInAsN, and GaAsSbN," *Appl. Phys. Lett.*, vol. 77, no. 16, p. 2482, 2000.

[120] D. B. Jackrel *et al.*, "Dilute nitride GaInNAs and GaInNAsSb solar cells by molecular beam epitaxy," *J. Appl. Phys.*, vol. 101, no. 11, p. 114916, 2007.

[121] K. Volz, J. Koch, B. Kunert, I. Nemeth, and W. Stolz, "Influence of annealing on the optical and structural properties of dilute N-containing III/V semiconductor heterostructures," *J. Cryst. Growth*, vol. 298, pp. 126–130, Jan. 2007.

[122] J. C. Harmand *et al.*, "GaNAsSb: how does it compare with other dilute III–V-nitride alloys?," *Semicond. Sci. Technol.*, vol. 17, no. 8, p. 778, 2002.

[123] K. Volz *et al.*, "Optimization of annealing conditions of (GaIn)(NAs) for solar cell applications," *J. Cryst. Growth*, vol. 310, no. 7–9, pp. 2222–2228, Apr. 2008.

[124] Y.-T. Lin, T.-C. Ma, H.-H. Lin, J.-D. Wu, and Y.-S. Huang, "Effect of thermal annealing on the blueshift of energy gap and nitrogen rearrangement in GaAsSbN," *Appl. Phys. Lett.*, vol. 96, no. 1, p. 11903, 2010.

[125] W. Shan *et al.*, "Band anticrossing in GaInNAs alloys," *Phys. Rev. Lett.*, vol. 82, no. 6, p. 1221, 1999.

[126] K.-I. Lin, K.-L. Lin, B.-W. Wang, H.-H. Lin, and J.-S. Hwang, "Double-Band Anticrossing in GaAsSbN Induced by Nitrogen and Antimony Incorporation," *Appl. Phys. Express*, vol. 6, no. 12, p. 121202, Dec. 2013.

[127] K. W. J. Barnham and G. Duggan, "A new approach to high-efficiency multi-band-gap solar cells," *J. Appl. Phys.*, vol. 67, no. 7, pp. 3490–3493, Apr. 1990.

[128] N. J. Ekins-Daukes *et al.*, "Strain-balanced GaAsP/InGaAs quantum well solar cells," *Appl. Phys. Lett.*, vol. 75, no. 26, pp. 4195–4197, Dec. 1999.

[129] S. Manzoor *et al.*, "Improved Light Management in Planar Silicon and Perovskite Solar Cells using PDMS Scattering Layer," *Submitt. Publ.*

[130] J. Escarré *et al.*, "Geometric light trapping for high efficiency thin film silicon solar cells," *Sol. Energy Mater. Sol. Cells*, vol. 98, pp. 185–190, Mar. 2012.

[131] M. A. Green *et al.*, "Solar cell efficiency tables (version 49): Solar cell efficiency tables (version 49)," *Prog. Photovolt. Res. Appl.*, vol. 25, no. 1, pp. 3–13, Jan. 2017.

[132] J. Tommila *et al.*, "Moth-eye antireflection coating fabricated by nanoimprint lithography on 1 eV dilute nitride solar cell: Moth-eye antireflection coating," *Prog. Photovolt. Res. Appl.*, p. n/a-n/a, Mar. 2012.

[133] N. Miyashita, N. Ahsan, M. Inagaki, M. Monirul Islam, M. Yamaguchi, and Y. Okada, "High electron mobility in Ga(In)NAs films grown by molecular beam epitaxy," *Appl. Phys. Lett.*, vol. 101, no. 22, p. 222112, 2012.

[134] A. Aho, A. Tukiainen, V.-M. Korpijärvi, V. Polojärvi, J. Salmi, and M. Guina, "Comparison of GaInNAs and GaInNAsSb solar cells grown by plasma-assisted molecular beam epitaxy," 2012, pp. 49–52.

[135] A. Aho, A. Tukiainen, V. Polojärvi, J. Salmi, and M. Guina, "High current generation in dilute nitride solar cells grown by molecular beam epitaxy," in *Proc. SPIE 8620, Physics, Simulation, and Photonic Engineering of Photovoltaic Devices II, 86201I*, 2013, p. 86201I.

[136] T. Thomas *et al.*, "GaNAsSb 1-eV solar cells for use in lattice-matched multi-junction architectures," in *Photovoltaic Specialist Conference (PVSC), 2014 IEEE 40th*, 2014, pp. 550–553.

[137] T. Thomas *et al.*, "Time-resolved photoluminescence of MBE-grown 1 eV GaAsSbN for multi-junction solar cells," in *Photovoltaic Specialist Conference (PVSC), 2015 IEEE 42nd*, 2015, pp. 1–5.

[138] A. Mitonneau, G. M. Martin, and A. Mircea, "Hole traps in bulk and epitaxial GaAs crystals," *Electron. Lett.*, vol. 13, no. 22, pp. 666–668, 1977.

[139] H. J. Von Bardeleben, D. Stievenard, D. Deresmes, A. Huber, and J. C. Bourgoin, "Identification of a defect in a semiconductor: EL2 in GaAs," *Phys. Rev. B*, vol. 34, no. 10, p. 7192, 1986.

[140] S. Sato *et al.*, "Defect characterization of proton irradiated GaAs pn-junction diodes with layers of InAs quantum dots," *J. Appl. Phys.*, vol. 119, no. 18, p. 185702, May 2016.

[141] T. Figielski, "Electron Emission from Extended Defects: DLTS Signal in Case of Dislocation Traps," *Phys Stat Sol A*, vol. 121, p. 187, 1990.

[142] V. Polojärvi, A. Aho, A. Tukiainen, A. Schramm, and M. Guina, "Comparative study of defect levels in GaInNAs, GaNAsSb, and GaInNAsSb for high-efficiency solar cells," *Appl. Phys. Lett.*, vol. 108, no. 12, p. 122104, Mar. 2016.

[143] L. Panepinto *et al.*, "Temperature dependent EBIC and deep level transient spectroscopy investigation of different types of misfit-dislocations at MOVPE grown GaAs/InGaAs/GaAs-single-quantum wells," *Mater. Sci. Eng. B*, vol. 42, no. 1–3, pp. 77–81, 1996.

[144] S. Wicaksono *et al.*, "Effect of growth temperature on defect states of GaAsSbN intrinsic layer in GaAs⁄GaAsSbN⁄GaAs photodiode for 1.3μm application," *J. Appl. Phys.*, vol. 102, no. 4, p. 44505, Aug. 2007.

[145] M. Kondow and F. Ishikawa, "High-Quality Growth of GaInNAs for Application to Near-Infrared Laser Diodes," *Adv. Opt. Technol.*, vol. 2012, pp. 1–11, 2012.

[146] F. Ishikawa, S. Wu, M. Kato, M. Uchiyama, K. Higashi, and M. Kondow, "Unintentional Source Incorporation in Plasma-Assisted Molecular Beam Epitaxy," *Jpn. J. Appl. Phys.*, vol. 48, no. 12, p. 125501, Dec. 2009.

[147] S. Tixier, M. Adamcyk, E. C. Young, J. H. Schmid, and T. Tiedje, "Surfactant enhanced growth of GaNAs and InGaNAs using bismuth," *J. Cryst. Growth*, vol. 251, no. 1–4, pp. 449–454, Apr. 2003.

[148] G. Feng, K. Oe, and M. Yoshimoto, “Temperature dependence of Bi behavior in MBE growth of InGaAs/InP,” *J. Cryst. Growth*, vol. 301–302, pp. 121–124, Apr. 2007.

[149] E. C. Young, S. Tixier, and T. Tiedje, “Bismuth surfactant growth of the dilute nitride GaNxAs1−x,” *J. Cryst. Growth*, vol. 279, no. 3–4, pp. 316–320, Jun. 2005.